INFILTRATION GROWTH PROCESSING OF YBCO NANOCOMPOSITES: SHAPE FORMING, MICROSTRUCTURAL AND MAGNETIC STUDIES

A thesis submitted for the degree of
Doctor of Philosophy

by

P. MISSAK SWARUP RAJU

School of Physics
University of Hyderabad
Hyderabad – 500046, India

October 2012

Dedicated

To

My Parents

DECLARATION

I hereby declare that the work reported in this thesis has been carried out by me under the supervision of *Dr. T. Rajasekharan,* Scientist-'G' (Former), DMRL, Hyderabad and *Professor V. Seshubai*, School of Physics, University of Hyderabad, Hyderabad, India. I also declare that this work has not been submitted to any University or Institution for the award of any degree/diploma.

P. MISSAK SWARUP RAJU

Date: October , 2012

Place: Hyderabad

CERTIFICATE

This is to certify that the research work compiled in this thesis entitled **"Infiltration growth processing of YBCO nano-composites: Shape forming, microstructural and magnetic studies"** has been carried out by *Mr. P. Missak Swarup Raju* under our supervision and the same has not been submitted for the award of any degree of any University.

Dr. T. Rajasekharan

RESEARCH SUPERVISOR
Scientist-'G' (Former)
Defence Metallurgical Research Laboratory,
Hyderabad

Professor V. Seshubai

RESEARCH SUPERVISOR
Professor, School of Physics
University of Hyderabad

DEAN
School of Physics

Date:
Place: Hyderabad

I thank Dr. Maqbool Ahmed, the PSO, Central Instrument Laboratory, University of Hyderabad for permitting me to use many of the central facilities to characterize the samples like X-ray diffractometer, Scanning Electron Microscope. I also thank Mr. C. S. Murthy, Senior Scientific Officer for his special concern. I thank Dr. Manjunath, Mr. Pavan, Mr. Nageswara Rao, Mr. Suresh, Ms. Nalini and all other technical staff of CIL for their readiness in helping me with the characterization work. I also thank Mr. Sambasiva Rao, Giri and Monto, technical staff of Liquid Nitrogen and Liquid Helium Plants of University of Hyderabad for providing me the liquid cryogens required for characterization of the samples in the present work. I thank **Dr. N. Hari Babu,** *Brunel University,* **UK** for providing Nd-123 seeds. I thank **Dr. N. Harish Kumar, IIT Madras** for useful discussions.

I express my thanks to the technical staff Mr. B. Satyanand, Mr. K. Srinivas, Mr. G. Mukanda Reddy, Mr. Vincent, Mr. Pentaiah, Mr. Ratnam, Mr. Zaheeruddin, Mr. Ravi Shankar, Mr. Venakateswara Rao of School of Physics for their willingness to help at various stages of this work. I specially thank **Mr. P. Krishna** for the invaluable services rendered in connection with setting up of various experimental facilities. I also thank all the non-teaching staff specially Mr. T. Abraham, Mr. G.L.N. Murthy, Mr. Anantharao, Mr. Mohan Rao, Ms. Saramma, Mr. Sunil for their timely help.

I take this opportunity to express my gratitude to **Rev Dr. B. Simon** and **Mrs B. Deva Deevena** for their continuous prayer and support at personal front. I specially thank Dr. B.D. J. Narendra, who motivated me to pursue research and stood by me during the odd times, I also remember Vijayalakshmi vadina, Teja and Abhi for their love and affection, which always made me feel at home. I also thank Rev. B. D. P. Ravindra, Jyothi vadina, Siddhardha and Hithardha as well as Dr. B. S. P. Surendra, Jessy vadina, Saman and Aman for their love and affection.

I wish to thank my seniors Dr. V. L. Kameswari, Dr. S. Santhosh, Dr. K. Balkis Ameen, my colleagues Dr. N. Devendra Kumar, Dr A. Satish Kumar, Dr. M. Ramudu, R. Parthasarathy,

M. Mahalaxmi, S. Pavan Kumar and others at the University. I too remember KK, Kumar, Farzana, Thejal, Usha, Vinod for all the precious moment that I shared with them. I also wish to acknowledge all my friends in School of Physics for their cooperation in carrying out my research work and also for making my stay in the University a wonderful and beneficial experience. My church, my second home and my dear brothers and sisters in Christ from Church at Gachibowli are of a great encouragement in all my ways.

I thank my parents for their love and unconditional support throughout my life. Thank you dear Mummy and Daddy for giving me the strength to accomplish my dream. I wish to extend my thanks to my dear brother and friend Issac and sister-in-law Latha.

Above all I would like to thank almighty for using me, a feeble with minimum understanding, to accomplish something that needs exceptional intelligence. I thank God for the wisdom and perseverance that he has bestowed upon me during this research project, and indeed, throughout my life: "*I can do everything through him who gives me strength.*" (Philippians 4: 13)

PLACE: HYDERABAD
DATE :

(P. Missak Swarup Raju)

CONTENTS

Chapter III

Introduction

1.1. Introduction

High temperature superconductors (HTSC), exhibiting superconductivity above the boiling point of liquid nitrogen, are among the most fascinating materials discovered in the last century. The initial excitement was in anticipation of finding room temperature superconductors. The quest is still on. And, a wide area of research on the physics of these interesting materials has opened up. The basic properties of superconductors are described in Appendix given at the end of the thesis. Even more effort had been put in exploiting the potential of these materials for applications, both in the form of wires/ tapes, and also as bulk components. Some of the applications being developed using high temperature superconductors are also discussed in the Appendix.

1.2. High temperature superconductors

The discovery of La-Ba-Cu-O superconductor in 1986 by Georg Bednorz and Alex Müller [1] was the starting point in the research on HTSC. This was followed by the discovery of cuprate superconductors with transition temperatures above the boiling point (77 K) of liquid nitrogen. Some of the cuprate compounds were discovered in the Y-Ba-Cu-O, Bi-Sr-Ca-Cu-O, Tl-Ba-Ca-Cu-O and Hg-Ba-Ca-Cu-O [2-5] systems, many of them with critical temperatures higher than 77 K (Fig. 1.1). Among the HTSC, transition temperatures up to 138 K (164 K under pressure) have been recorded in Hg-based superconductors [5]. Superconductivity was later discovered in magnesium diboride (MgB_2)[6], which showed a T_c of 39 K. Other interesting

discoveries were superconductivity in the fulleride compound CsC60, with a T_c of 40 K [6] . Most recently, iron-based series of compounds have been discovered whose T_c has risen to ~50 K[8].

Most of the application oriented research on HTS has been confined to $Bi_2Sr_2Ca_2Cu_3O_y$ (BSCCO) and $REBa_2Cu_3O_{7-\delta}$ (REBCO, RE stands Rare Earth elements such as Y, Nd, Sm, Gd, Dy etc) systems. Tl-Ba-Ca-Cu-O, Hg-Ba-Ca-Cu-O etc. drew less attention due to their toxicity and the difficulties involved in their preparation [3-4]. Substantial amount of work has been done on the BSCCO system due to the relative ease with which wires/tapes can be fabricated out of this material. Operation of these at higher magnetic fields had been limited due to flux creep problem [9].

At present, REBCO superconductors are the most promising materials for various applications because of their reasonable transition temperatures, relatively lower toxicity, manageable flux-creep problems and to a considerable extent, the available control over their properties through process modifications.
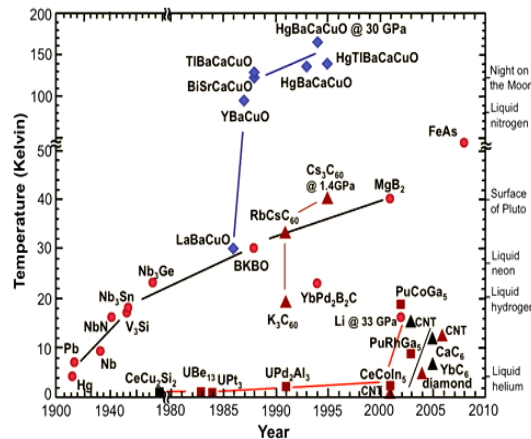
Fig. 1.1 Evolution in the transition temperatures of superconducting materials, starting with mercury. Recent discoveries are also included [10].

1.3. Properties of REBCO Superconductor

REBCO are black ceramic superconductors with their transition temperatures around 92 K. They, when oxygen deficient, have the formula $REBa_2Cu_3O_{6.5}$ and a tetragonal crystal structure; and the composition changes to $REBa_2Cu_3O_{7-\delta}$ with the structure changing to orthorhombic through oxygen ordering in the b-direction (see Fig. 1.2), when annealed for long durations at lower temperatures.

REBCO is known to be anisotropic in nature [2]; it has been established that the current density (J_c) supported by the materials is lower by an order of magnitude when the current flows in the c-direction than when it flows in the Cu-O layers in the c-plane [11].
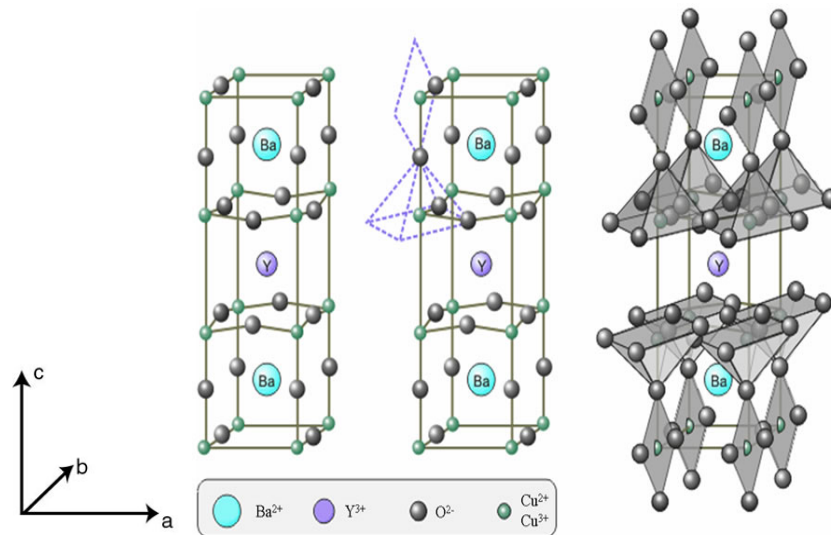
Fig. 1.2 The orthorhombic unit cell of $YBa_2Cu_3O_{7-\delta}$. It has lattice parameters a ~ 3.82 Å, b ~ 3.89 Å, c ~ 11.68 Å, and space group P4/mmm , T_c = 92 K. The notable feature is the presence of a sequence of copper-oxygen layers perpendicular to the c-axis [12].

1.4. REBCO superconductors fabricated by melt growth process

Initially REBCO Ceramic superconductors were processed through conventional sintering technique which yielded samples with randomly

oriented grains. Random orientation of the grains gives rise to weak links at the grain boundaries bringing down the overall current carrying capability. Macroscopic defects such as cracks, porosity and secondary phases also affect the current densities [13]. Fig. 1.3 shows typical micrograph of a sintered YBCO superconductor.
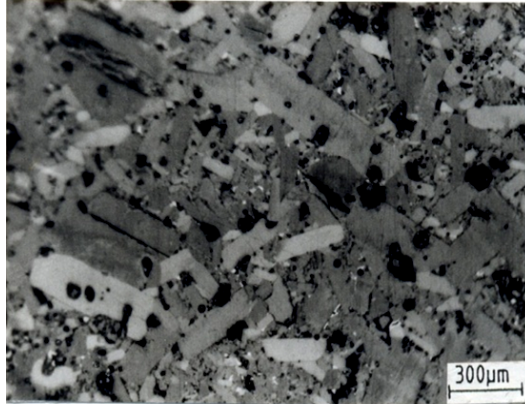
Fig. 1.3 Optical micrograph of a sintered YBCO superconductor showing randomly oriented grains and a large amount of porosity.

Melt texturing technique developed by Jin et al. [13] was the first process to yield bulk samples of YBCO supporting relatively high current density. The initial melt textured samples were significantly improved in their capacity to carry currents in comparison with sintered samples; they supported current densities of the order of 10^4 A/cm^2 at zero field [14].

1.4.1. Melt Growth Process (MGP)

The Melt textured growth of REBCO [13] consisted of heating the precursor REBCO to above its melting temperature, and growing and aligning crystals from the super-cooled melt, followed by a prescribed heat treatment schedule for homogenization, stress relief, enhancement of oxygen content and cleaner grain boundaries without "weak links". Significant improvement

4

in mechanical, electrical and magnetic properties of the melt textured samples triggered increased attention towards improving and modifying the fabrication techniques, and resulted in the development of several variants of the melt processing technique such as Quench powder Melt Growth(QMG) [16], Melt Powder Melt Growth(MPMG) [17], Powder Melting Process(PMG) [18], Oxygen Controlled Melt Growth process(OCMG) [19], Top seeded melt growth(TSMG) [20], etc. Many reports have been published highlighting various facets of melt processed materials [11, 20-27].
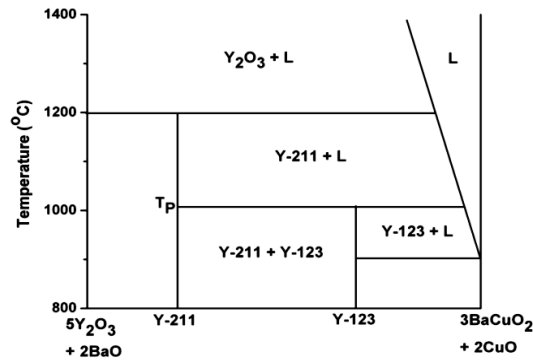
Fig. 1.4 The pseudo-binary phase diagram of the Y-Ba-Cu-O system, showing various phases that occurs in the system. The peritectic formation temperature (T_p) of Y-123 is marked [13].

Melt growth process [13] was developed by studying the pseudo binary phase diagram in Fig.1.4 and exploiting the peritectic decomposition of YEBCO. In Melt growth process Y-123 compound is heated above its peritectic temperature (T_p) to dissociate it into Y_2BaCuO_5 (Y-211) and liquid phases ($BaCuO_2$ and CuO). The peritectic reaction for YBCO can be written as

$$Y_2BaCuO_5 + 3BaCuO_2 + 2CuO \Leftrightarrow 2YBa_2Cu_3O_{6.5}$$
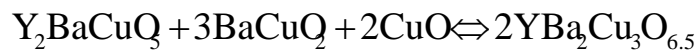
The properitectic mixture thus obtained reacts to produce aligned grains of RE-123 when cooled slowly below T_p and maintained there for some duration. The value of T_p is around 1008 °C for YBCO in air; and

5

increases with increasing atomic volume for REBCO with other rare earths [21, 22]. Examples are $T_p \sim 1030$ °C for GdBCO, $T_p \sim 1054$ °C for SmBCO and $T_p \sim 1068$ °C for NdBCO, in air.

Melt processing a composition that is richer in Yttria leads to excess Y-211 in the melt processed material, which appears as inclusions in the Y-123 matrix. An optical micrograph in Fig. 1.5 illustrates the major microstructural features seen in melt processed Y-123.
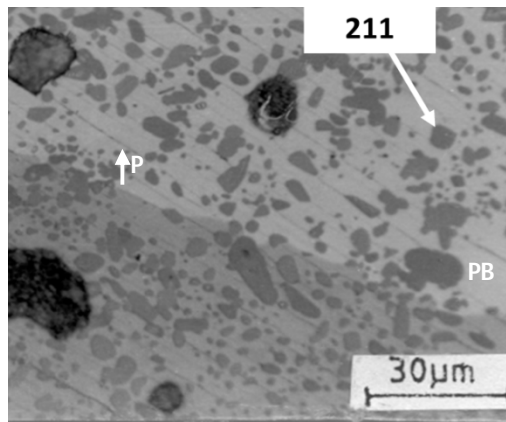
Fig. 1.5 Typical microstructure of melt processed Y-123 material. Polarized light microscopy reveals two shades of grey due to orientation difference between two grains. Y-123 occurs as parallel platelets separated by small gaps within each domain. Properitectic Y-211 phase occurs as inclusions within the Y-123 grains. The Y-211 inclusions are not uniformly distributed, are rather large and blocky. Also, defects such as large pores can be seen.

1.4.2. Developments of MGP

$REBa_2Cu_3O_{6.5}$ with tetragonal crystal structure is formed after a hold of several hours at a temperature below T_p to complete grain growth in melt growth process, and thus formed $REBa_2Cu_3O_{6.5}$ is not superconducting. Prolonged oxygen treatment at a temperature in the range 300 °C- 600 °C increases the oxygen content [11] and shifts the formula to $REBa_2Cu_3O_{7-\delta}$, with orthorhombic crystal structure, rendering the sample superconducting.

Twinning appears in the superconductor matrix to accommodate stresses accompanying the transformation [24]. A substantial amount of shrinkage, and formation of macroscopic defects in the interior of the samples due to liquid phase loss, is typical of the process [28], (see Fig.1.6). A large part of the work on melt growth process was aimed at optimizing the microstructure of the material so that it supports large current densities. Other important requirements for applications are shaping the material in required geometries with good mechanical strength and minimal macroscopic defects.
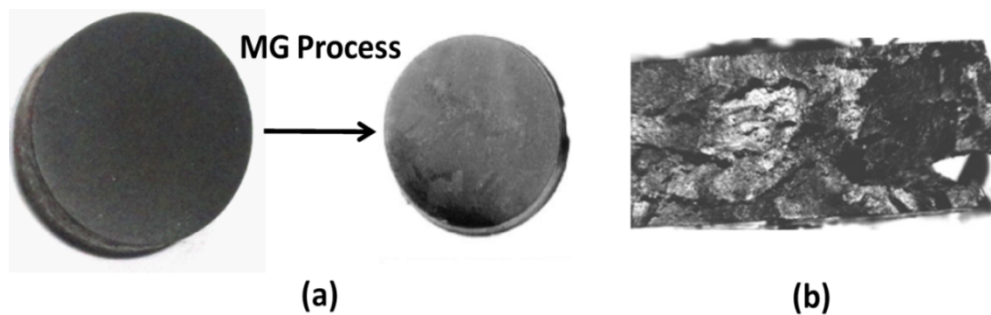
Fig. 1.6 (a) Shrinkage of a stoichiometric YBCO sample subjected to Melt growth process. The figure on left illustrates the starting (before melt growth process) size of a pellet (~ 34 mm dia.), and the figure on right is that of the resulting product (~ 26.5 mm dia.). The shrinkage caused is ~ 22 %. Also, distortions in shape can be noticed. **(b)** Vertical cross-section of a melt grown pellet of Y-123. Macroscopic defects such as large hollow regions can be seen [28].

This section summarizes briefly the current understanding of microstructural developments in melt grown REBCO materials and compares it with that in IG processed materials. A recent review from our group summarizes the important aspects [29]. Murakami et al. [25] reported that the presence of an optimized amount of fine-sized Y-211 inclusions in the Y-123 matrix can enhance the J_c of melt processed Y-123 considerably. In the

optimized materials, levitation effects were demonstrated to be sufficient to lift a person(s) on a platform of magnets floating on melt processed Y-123 pellets [9, 27].

The improvement in critical current densities (J_c) in the presence of Y-211 inclusions is attributed to the formation of secondary defects [25, 26], of the size of the coherence length, at the interface between Y-211 inclusions and Y-123 matrix. The coherence length in RE-123 is of the order of a few nm [23]. The interfacial defects are formed due to thermal expansion mismatch between the Y-123 and Y-211 phases. The larger the curvature of the Y-123/Y-211 interface, the more is the probability of finding such defects. Evidence for the occurrence of such defects has been reported from TEM studies (Fig. 1.7).
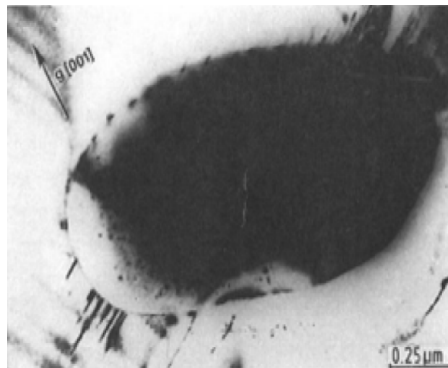
Fig.1.7 TEM micrograph showing secondary defects at the Y-123/Y-211 interface, in the matrix of melt processed Y-123. More defects are seen in regions of larger interface curvature [26].

The effect of increasing Y-211 content on the microstructure of the melt processed Y-123 has been systematically studied [30]. The Y-211 inclusions in melt processed Y-123 become smaller and more spherical in shape with increasing Y-211 content, essentially following the variation in size of the Y-211 particles in the properitectic melt (Fig. 1.8).
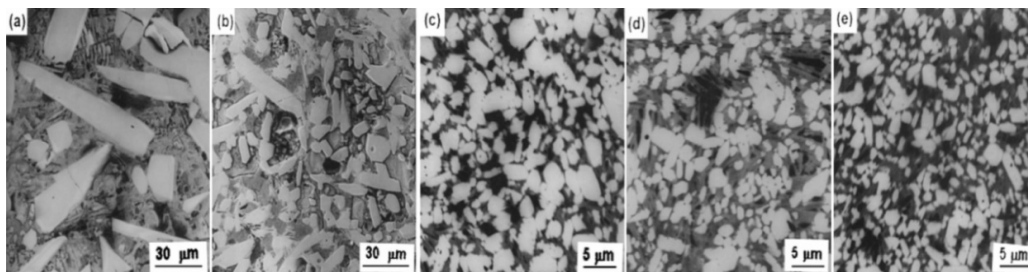
Fig. 1.8 SEM micrographs from Gd-123/Gd-211 pellets quenched from 1100°C, after a hold of 20 minutes, showing Gd-211 particles in liquid. In samples containing **(a)** 0 **(b)** 10 **(c)** 20 **(d)** 30 and **(e)** 40 mol. % Y-211 added to Y-123, we observe that the Y-211 particles become finer, denser in distribution and spherical in morphology, with increasing Y-211 concentration [31].

The melt process results in multigrain samples with large grains of RE-123, a few millimeters in size. It is believed that large angle grain boundaries in the melt processed material cause a rapid decrease in the magnitude of J_c [32]. Seed crystals, one or many, have been used, in different configurations to promote controlled single/multi grain growth. If the peritectic recombination of Y-211 and liquid phases takes place in the presence of a suitably placed seed crystal, the entire material can grow as a single grain [33], thus increasing the J_c.

The major disadvantage in melt growth process is shrinkage, the origin of shrinkage and its management through controlling the RE-211 content, has been studied in Gd-Ba-Cu-O system [28]. Most of the shrinkage has been observed to take place during melting of RE-123 pellet to form RE-211 and liquid phases, and almost no shrinkage occurs during subsequent recombination below T_p, to form RE-123. Shrinkage variations, measured with respect to the size of the starting pellets, as a function of Gd-211 content in melt processed Gd-123/Gd-211 composites, are compared at two stages, viz. just after melting, and after complete processing, in Fig. 1.9 [28].
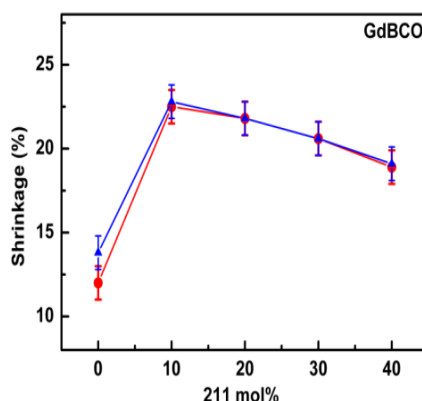
Fig. 1.9 Shrinkage during melt processing: Plots showing experimentally measured shrinkage of Gd-123 samples as a function of Gd-211 mol%. Gd-123/Gd-211 pellets were prepared by adding systematically increasing amount of Gd-211 powder to Gd-123 and compacting the mixture. The x-axis refers to the amount of Y-211 *added* to Y-123, and does not include the Y-211 formed by decomposition of Y-123 at T_p. Shrinkage (in %) of the pellets after melting them around 1100°C are shown as triangles, and the shrinkage after complete melt processing are shown as circles. Almost all of the shrinkage takes place at the melting stage, and none at all at the subsequent recombination stage [28].

1.4.3. Limitations of MGP

Melt processed RE-123 is always associated with occurrence of systematic porosity. Pore distribution in melt processed Gd-Ba-Cu-O samples with increasing Y-211 content, is displayed in Fig. 1.10.
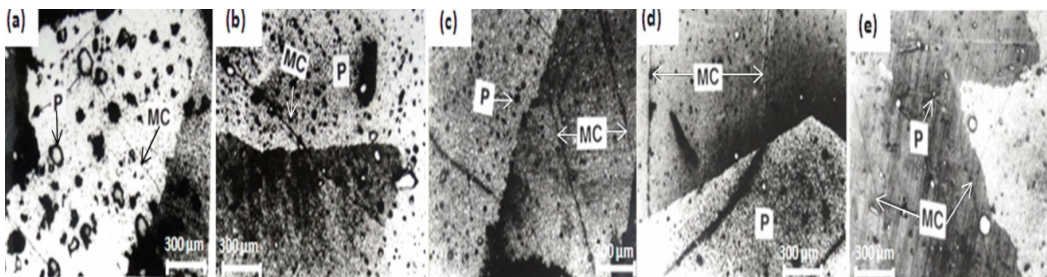
Fig. 1.10 Systematically occurring porosity in melt processed samples with different Y-211 content. The pores are very large in melt processed stoichiometric Gd-123, and the pores decrease sharply in size with just 10 mol% added Y-211[34].

The reasons for such pores were often believed to be the evolution of oxygen during melt processing [35]. An alternative explanation for the observed pore sizes, and their variation with Y-211 content, is as follows: during the texturing stage, the liquids move towards the Y-211 skeleton to react and form Y-123. Since the Y-211 skeleton does not melt or get distorted during the process. In samples which shrink less during melting due to the acicular nature of the Y-211 particles, the liquid phase movement will leave back more porosity. This picture is supported by the observation that the pore size and its variation with Y-211 content shown in Fig. 1.11, compares with the Y-211 size and its variation with Y-211 content in the pro-peritectic melt.
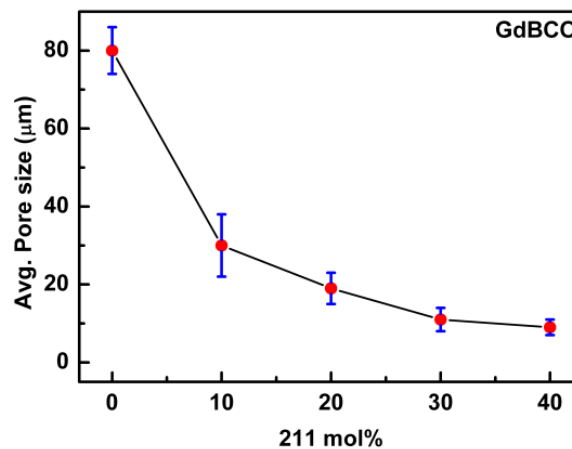
Fig. 1.11 A plot showing variation of the average pore size in melt processed Gd-123, as a function of increasing Gd-211 content [34].

1.5 REBCO superconductors fabrication by Infiltration and Growth (IG) process

The Infiltration Growth (IG) process was developed to overcome problems associated with melt growth process [36-38]. The IG process offers several additional advantages as well, in terms of improved microstructure [36-41]. The process uses an assembly as shown in Fig. 1.12. A preform of

RE-211 is kept in contact with a source of liquid phases, usually of Y-123, $BaCuO_2$ and CuO in a certain proportions. By heating the assembly to a temperature 30-40 °C above the T_p of the RE-123 compound involved, the liquid phases ($BaCuO_2$ + CuO) are infiltrated into the preform.

The assembly is then cooled down slowly to a temperature below the peritectic temperature T_p, where the liquid phases react with RE-211 to form RE-123 phase, with excess RE-211 left back as inclusions in the RE-123 matrix. Many minor variations of the arrangement shown in Fig. 1.12 have been reported with good success. For instance, liquids have been infiltrated from the top or bottom of the preforms with almost equal ease [35, 41]; the primary driving force for the infiltration of the liquids being the capillary forces.
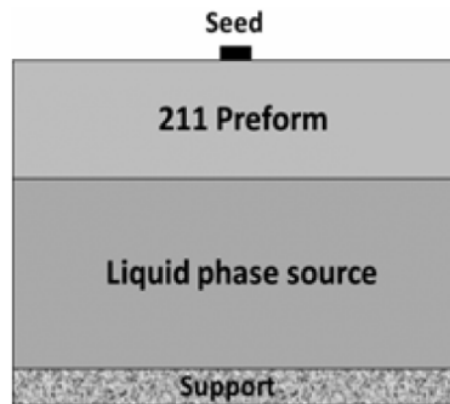
Fig. 1.12 A typical experimental arrangement used in Infiltration Growth process. A source of liquid phases which can either be Y-123 or Y-123+ $BaCuO_2$ + CuO. A preform made up of Y-211 powder is kept on top of it. A c-axis oriented Nd-123 seed crystal is placed on top of the preform, at the center [29].

Different ways of assembling the Y-211 preforms, liquid phase sources and seeds, various ways of supporting the assembly during heat treatments, and variations in composition of the liquid phase sources [42-47] have been reported.

12

The IG process is compared and contrasted with the melt growth process in Fig. 1.13. In the melt growth process, schematically described in the top row in the Fig. 1.13, RE-123 is molten above its peritectic melting temperature to form Y-211 and liquids. The sample shrinks nearly 13 to 22% on melting. Subsequently, when the Y-211 and liquids are recombined below T_p to form textured Y-123, the shrinkage and distortions generated during melting are retained. Macroscopic internal defects can appear in the interior of the sample due to liquid phase outflow. On the other hand, in the IG process, when the preform of Y-211 is infiltrated by the liquid phases, the shrinkage is less than 0.4%. The infiltrated preform is then reacted below T_p to from Y-123. Since the skeleton of Y-211 remains intact in shape and size during both the liquid infiltration and subsequent reaction to form Y-123, there is practically no shrinkage during the process. The Y-211 particles left back in the Y-123 matrix are uniformly distributed, fine in size and spherical. The systematically occurring porosity in melt processed Y-123 is eliminated due to a continuous supply of liquids during the peritectic formation of Y-123.

The use of seed crystals to promote single grain growth in IG process has been discussed by several authors [48-51]. Hari babu et al. [52] discuss replacing Nd-123 by a universal seed crystal in IG processing. They suggest a generic seed crystal cleaved from melt processed Nd-123 with 5% to 10% Mg substituted for Nd, with a melting point about 20°C higher than that of Nd-123. The use of such a seed eliminates the need for hot seeding in the IG processing of materials like Sm-123 and Nd-123.
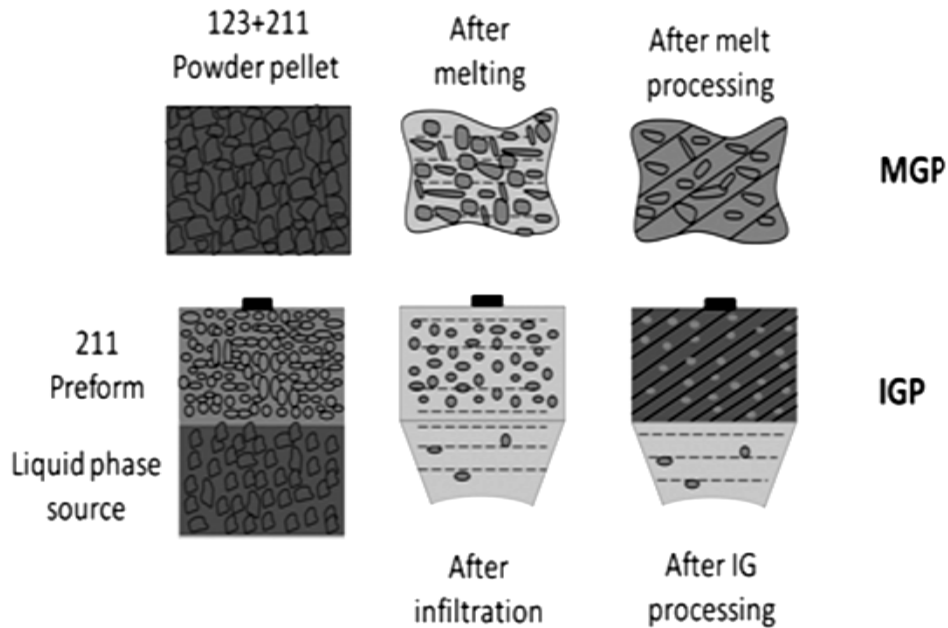
Fig. 1.13 A comparison between the Melt growth process and the Infiltration growth process [29].

Li et al. [53] discuss the importance of choosing an appropriate temperature window to promote single grain growth while using a seed crystal. They cite the example of IG processing Gd-123 whose T_p is around 1040 °C in air. Nd-123 seed crystals were used. After the infiltration of liquid phases at 1060 °C, different samples were furnace cooled to different temperatures below T_p and were maintained there for 20 hours for Gd-123 growth, and then furnace cooled. It was observed that more the undercooling, faster was the epitaxial growth of the Gd-123 grain. But, at temperatures more than 15 °C below T_p, multiple nucleation unrelated to the seed crystal started taking place in various regions of the sample.

1.6   Shape forming by IG process

A major advantage of the IG process is that it allows, by eliminating shrinkage, near net shape fabrication of RE-123 products with

microstructures that support high current density. This possibility is particularly important because the melt processed material is difficult to machine. In IG processing, a Y-211 preform of the required shape and size might be fabricated using any of conventional ceramic shape forming techniques such as uniaxial pressing, isostatic pressing, injection molding, slip casting etc.. Liquid phase sources are kept in contact with the preform. The assembly is taken through infiltration and texturing stages to produce a product that needs almost no further machining. The first 3-D component made by IG process [28], a hollow cylinder of Y-123, is shown in Fig. 1.14.
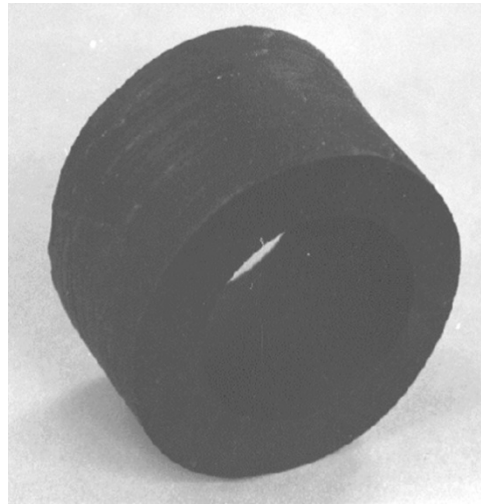
Fig. 1.14 A hollow cylinder of Y-123 fabricated by the Infiltration Growth process [28].

The IG process has been used to fabricate superconductor foams by Reddy and Schmitz [54]. Commercially available rubber sponges with various levels of interconnected porosity were dipped in slurry of Y-211 powder and dried; and the process was repeated several times to build up the required thickness for the Y-211 layer.
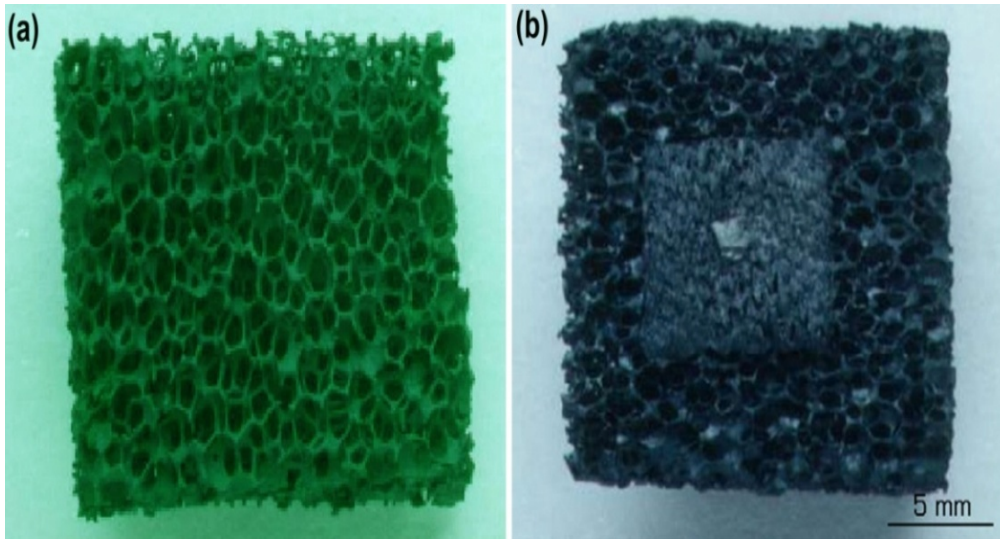
Fig. 1.15 (a) Y-211 foam prepared as a replica from a rubber sponge from Y-211 slurry, and **(b)** Y-123 foam derived from the Y-211 foam by the IG process [54].

The rubber was later burnt away in a controlled fashion. The preform thus prepared was processed with suitably placed liquid phase sources and seed crystals to fabricate the IG processed Y-123 sponge (see Fig. 1.15). By maintaining the texturing temperature above 990 °C, multiple nucleations could be prevented and single grain Y-123 foam as big as 100mm x 100mm could be prepared. Foams have been made out of Dy-123 as well [39]. Superconductor foams had hitherto not been fabricated out of any material, and its development through the IG process can potentially offer interesting possibilities, both in science and technology. Fundamental aspects like contributions of surface pinning become interesting because the critical current densities in the foam will strongly differ from that of bulk specimens having similar microstructures. The porosity allows relatively easy oxygenation of large components. The foams can be heated or cooled quickly using liquid or gaseous cryogens that percolate their continuous porosity with ease. They have been proposed for use in fault current limiters; such

16

devices can be rapidly restored back to the superconducting state after temporary disturbances drive them normal.

Using Y-211 blocks with systematically drilled holes, Y-123 samples with systematic array of holes have been created [55], see Fig. 1.16. The holes can be used for rapid heat extraction from the material. In addition, the holes can be filled with resins or molten metal to reinforce the IG processed material. Such a possibility can be very valuable since flux trapping in the superconductor during applications can cause enormous stresses.
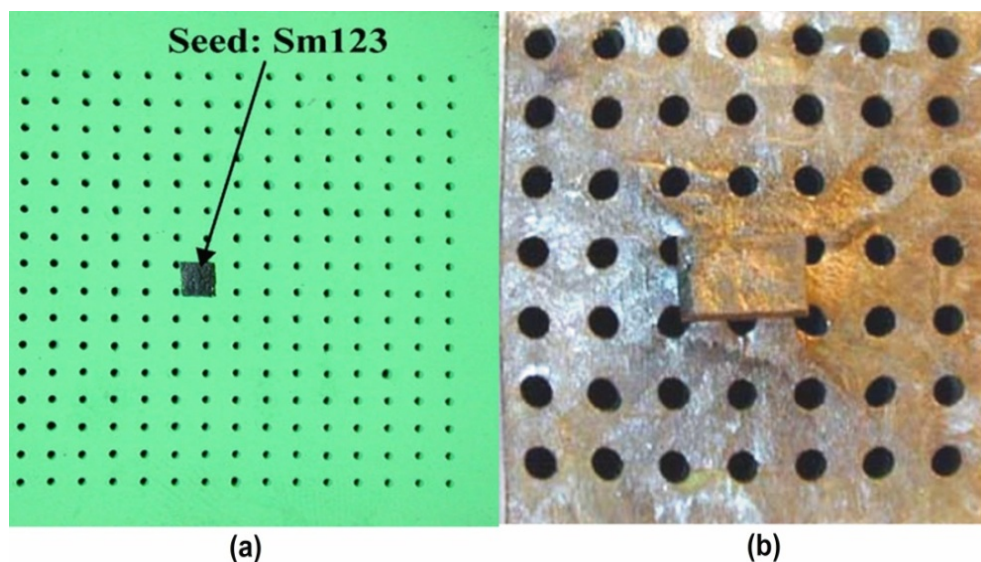
Fig. 1.16 (a) A Y-211 preform with an Sm-Y-123 seed at the centre. Arrays of holes have been drilled systematically through the preform; **(b)** IG processed Y-123 with an array of holes [55].

IG process has been used to fabricate thick films of REBCO superconductor [56]. The preform in this case is fabricated out of clothes woven out of Y_2O_3 fibers. By infiltration of suitable liquids and reacting below the peritectic formation temperature of Y-211, the fabric is converted into a Y-211 fabric, which is subsequently converted to Y-123 through the IG process.

Fabrication of large single grains of Y-123 by IG process for application as trapped field magnets [57-60] has been reported. Most applications that require bulk RE-123 may not need materials fabricated in very complex shapes. Even while fabricating relatively simple shapes, the IG process offers several advantages in terms of improved macro- and microstructures.

1.7 Flux pinning and critical current densities in REBCO superconductors

The critical current density for YBCO superconductors increases systematically, and by several orders of magnitude, with increasing amount of Y-211 precipitates in the Y-123 matrix [22, 30]. As discussed in the earlier section, as the externally added Y-211 content in melt processed Y-123 is increased, the particle size of Y-211 precipitates systematically decreases [30]. The reason for the improvement in J_c with increasing Y-211 content is believed to be the creation, at the Y-123/Y-211 interface, of a large number of nanometer-sized defects, of the order of the coherence length, to serve as flux pinning centers [25, 26]. The critical current density supported by melt processed Y-123 bulk is reported to increase with increase in surface area of Y-211 phase particles [61].

Various methods have been attempted in the literature to refine the Y-211 size in melt processed Y-123:

I. Addition of Pt and PtO_2 has been found to decrease the size of Y-211 particles and also to change the morphology of the Y-211 to one with a very high aspect ratio. This method has been widely used to reduce Y-211 precipitate sizes in melt-texturing techniques.[62]

II. Rapid heating of Y-123 during melt processing, to above the peritectic temperature has been found to result in refined Y-211 [63].

18

III. The addition of heterogeneous nucleation sites in the form of excess Y-211or other second phase additions has been found to act as nucleation sites for the peritectically produced Y-211, thereby decreasing the average Y-211 particle size. For example, Jin et al. [64] added aerosol-processed Y-211 particles that initially were 0.2 μm in size and, after texturing were 0.7 μm in size, in Y-123 matrix.

IV. Use of alternative precursors results in the formation of refined Y-211 particles in the Y-123 matrix. For example, one can begin with Y-211 + liquid phase (PMP), (Y_2O_3 + liquid) produced as a result of a quench process (QMG or MPMG), or well-dispersed Y_2O_3 + liquid produced by a solid-state route (SLMG). [65]

In addition to Pt and PtO_2, CeO_2 has also been observed to refine the size of Y-211 particles in melt processed Y-123[62, 65-66]. Although, in many instances, the additions were made with the hope that they would act as fine flux pinning centers, they had the effect of dramatically modifying the morphology and size of the Y-211 phase. In Fig. 1.17, reproduced from Kim et al. [62], we observe that Y-211 size is substantially refined by the addition of ceria. The current density supported by the sample is also considerably improved.

Various alternative methods have also been reported in the literature to introduce fine defects of size comparable to the coherence length in melt processed materials [67-70]; such attempts have been made with the IG processed materials also, but to a lesser extent. Substitution of metallic ions in Cu site creating defects in the lattice to pin magnetic flux has been tried; the substitution has been observed to lower/broaden the superconducting transition temperature [71][70]. Alternative methods such as heavy ion irradiation [72] neutron irradiation [73] proton irradiation [74] and even

19

electron irradiation [75] have been tried to create defects; such irradiation creates controlled fine defects, both columnar and point defects. Although these methods have considerably improved the critical currents at high fields, large scale industrial applications are hindered by cost and by possible radioactive residues.
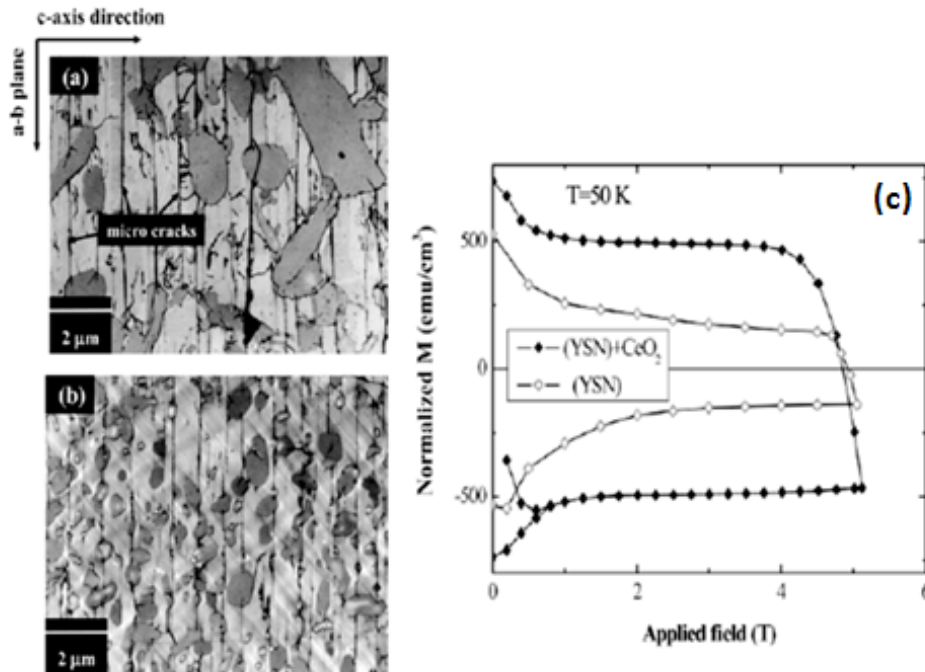
Fig. 1.17 **(a)** In melt processed YBCO wihtout extra Y-211 and without any other additives, the size of the Y-211 particles is of the order of few tens of microns, and **(b)** with CeO_2 added to the same sample as in **(a)**, the Y-211 grain size is considerably reduced (to about 1-2 μm). **(c)** Magnetic hysteresis loops obtained at 50K from the samples in **(a)** and **(b)** show that the loop area substantially increases with added ceria [62].

Apart from reducing Y-211 size, many groups across the world have tried to introduce nanometer-sized pinning centers in the Y-123 matrix of the melt processed material. Nanoparticles of dopants like Y_2O_3 [68], ZrO_2 [69], $BaCeO_3$ [70], Al_2O_3 [76] and NiO [77], have been introduced as fine

20

second phase particles in the Y-123 matrix. $Y_2Ba_4CuMO_y$ (M=U, Nb, Ta, Mo, W, and Re) [78] nanoparticles have been introduced into the YBCO matrix during melt processing and IG processing. Most often, the expectation has been that the particles themselves would serve as pinning centers, but in cases like ceria, zirconia, barium cerate etc. reactions with the Y-123/Y-211 system leading to Y-211 size refinement has been observed.

Majority of the literature on nanoparticle-doping in YBCO system discusses doping during the Melt Growth (MG) process, where nanoparticles are added directly to the precursor powder and mixed thoroughly. The mixing is done mostly by ball milling, either dry or wet. The green body prepared by pressing YBCO containing the dopant, is melted above the peritectic temperature of YBCO where it melts into Y_2BaCuO_5 and liquid phases. The mixture is then cooled to below the peritectic temperature to regenerate large grains of YBCO with flux pinning precipitates in the superconductor body. Due to the corrosive nature of the liquid phases involved in the MG process and the fine size of the dopant particles, reactions between the matrix and the dopants, and 'pushing effects' [79] whereby the particles agglomerate, are inevitable. Fig. 1.18 demonstrates the effect of nanoparticles being carried along by the liquid phases. In the reports that discuss the introduction of nanoparticles during the Infiltration and Growth process, the nanoparticles were introduced along with the liquid phases [58]; the particles tend to agglomerate while in the liquid phases.
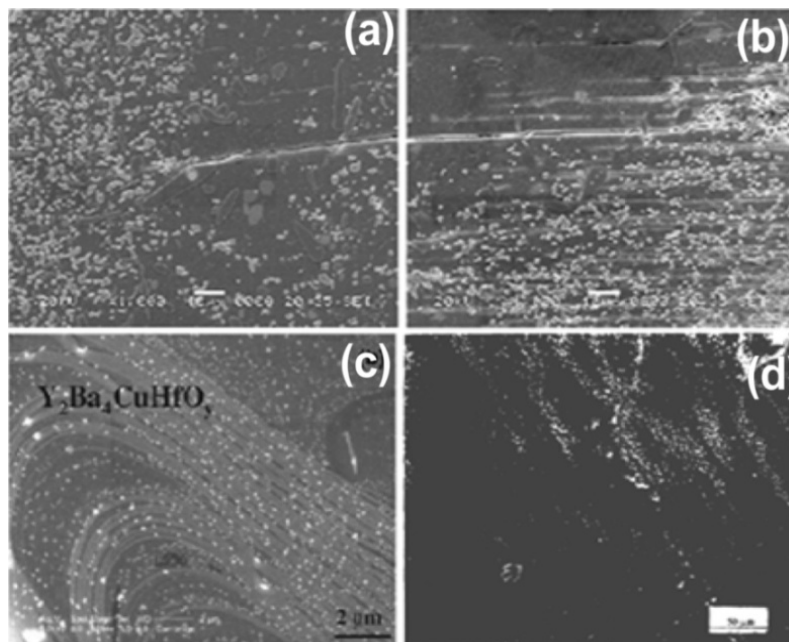
Fig. 1.18 Nanoparticles in melt processed YBCO are carried along by the liquid phases causing **(a)** and **(b)** segregation/agglomeration of nanoparticle and free regions [70]. **(c)** and **(d)** (from[80] and [81] respectively)shows track/ bands of nanoparticles in the YBCO matrix.

To obtain optimum benefits from nanoparticle doping, especially when dealing with large concentrations of additives, it is necessary to develop methods that allow uniform distribution of nanoparticles in the YBCO matrix, completely eliminating agglomeration. A novel method for doing the same is presented in this thesis, which introduces nanoparticles into the preform used for IG processing without agglomeration and they remain isolated from one another. Furthermore, the particles remain anchored to the Y-211 particles in the preform during liquid phase infiltration. The fact that the preform in IGP does not melt and flow during the process is important in this context. Apart from better control of the microstructure, the procedure also allows more transparency in studying the development of the microstructure.

IG process offers several advantages (like near net shape fabrication) in comparison with the melt growth process as enumerated earlier; however, the current densities obtained in IG processed materials have been rather low, of the order of 10-70 kA/cm^2 [34, 42, 45-48] at zero field. The high field performance of these materials has not been appreciable; critical currents carried at zero field could hardly be sustained up to 3T. In comparison, the best low field current densities supported by melt grown samples (see Fig 1.19) are in hundreds of kA/cm^2 [82].
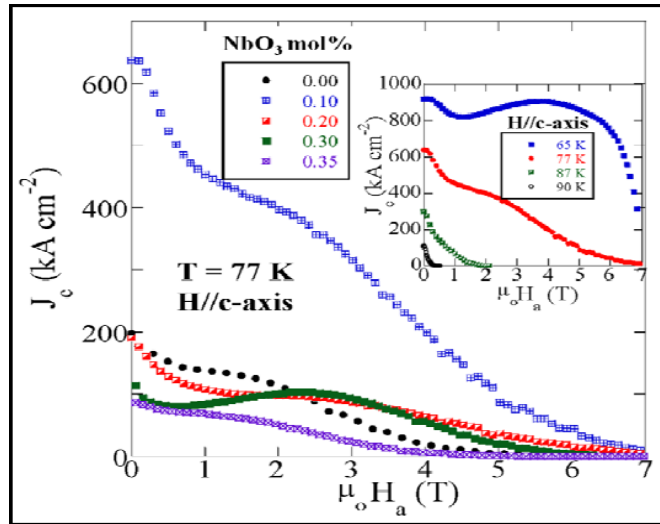
Fig 1.19 J_c (B) curves for $(Nd_{0.33}Eu_{0.33}Gd_{0.33})Ba_2Cu_3O_{7-\delta}$ with 35 mol% fine Gd-211 (70nm), but various contents of NbO$_3$. Inset illustrates the J_c(B) curves at different temperatures for the doping level of 0.1mol% NbO$_3$ [82].

Recent experiments in optimizing the IG process through an optimization of the pressures under which the Y-211 preform is fabricated and through optimized pre-sintering of the Y-211 preform (called Preform Optimized IGP, or POIGP), have improved the current carrying capacity of IG processed materials to very high fields [36, 83], as evidenced by flat J_c versus H curves reported up to 13 T at 65 K. However, the values of J_c(0) obtained in IG processed materials are low in comparison with those obtained in the best

melt grown samples. An examination of the literature shows that the melt grown samples which show very high current densities are those in which a large amount of nano-sized RE-211 particles, along with other minor nano-dopants like NbO_3, are externally added (Fig 1.19).

Considering the advantages offered by the IG process, it is of interest to introduce large amount of nanoparticles into IG processed RE-123 as pinning centers. In the present work, we have devised a novel process to fabricate preforms wherein the nanoparticles from a uniformly dispersed sol are deposited individually on the surface of the Y-211 particles in the preform. We refer to that process as Nano Dispersed Sol Casting (NDSC), for convenience.

The NDSC process is of interest because well-dispersed unreacted nanoparticles in YBCO can potentially enhance J_c. The process has the further advantage that the reactions taking place during Infiltration Growth processing among various components of the reaction system in presence of nano-dopants, become easier to understand. The introduction of ceria, zirconia and $BaCeO_3$ in melt processed Y-123 has been studied widely in literature [62, 65, 67-71]. Ceria and Pt are known to refine the size of the residual Y-211 particles in the Y-123 matrix after melt growth. The mechanism by which these additives reduce the size of the Y-211 inclusions has been of immense interest. Kim et al. [84] have suggested that ceria dissolves in the liquid phase containing $BaCuO_2$ and forms $BaCeO_3$. This depletes the liquid phases of Ba and thus modifies the interfacial energy between the Y-211 particles and liquid phase, thereby restricting the coarsening of the Y-211 particles. Vilalta et al. [85] proposed the formation of Y_2O_3 nanoparticles by the interaction of ceria with Y-211 and liquid phases,

and that these Y_2O_3 nanoparticles would act as nucleation sites for the pro-peritectic Y-211.

It is known that the IG process results in substantial refinement in the size of the Y-211 inclusions, without the need to add any refining agents [83]. The size of the Y-211 inclusions in IG processed materials is of the order of one micron, whereas in melt processed materials, the size of the Y-211 inclusions can be much larger if no refining agents are added. We have investigated the question of whether the introduction of nanoparticles of ceria, zirconia and $BaCeO_3$ into IG processed Y-123 can cause further refinement of the Y-211 inclusions. We have then looked at the reasons why such refinement of Y-211 takes place in the system with the addition of ceria, but not with the addition of $BaCeO_3$. Since no fresh Y-211 is introduced into the system by the melting of Y-123 as in the melt growth process, it is easier to track the size reduction of the particles pre-existing in the preform. Microstructural observations at various stages during IG process using preforms containing isolated ceria nanoparticles, is used to reveal a possible mechanism for the refinement of Y-211 particles in the presence of ceria. Current densities and their magnetic field dependences are measured for samples containing different dopants in varying concentrations. The microstructures and current densities supported by the final products are studied as a function of the nature of the additives and their concentrations.

Retention of a favorable distribution of nanoparticles in the Y-123 matrix is most desirable in a complex-shaped IG-processed product. Gelcasting is a generic process used in the manufacture of ceramic products. In this process, high-quality complex-shaped ceramic parts are formed by the polymerization of uniform slurry containing ceramic powders. The main challenge is the preparation of a self-standing slurry with a high loading of

the ceramic powders, along with a monomer, cross-linking polymers and surfactants. A macromolecular network is created which holds the ceramic particles together when the mixture is polymerized. The ceramic part takes the shape of the mold in which the slurry is polymerized. The polymer is later burnt out in a controlled fashion. Gelcast green bodies have a low polymer content (<5%), and complicated binder burnout schedules can be avoided. The process does not involve extensive and expensive machinery, thus simplifying the overall process and drastically reducing the cost and energy requirement. The compatibility of the process with wide range of mold materials and mold types opens up a range of options for shaping: starting from simple sand molds to complicated rapid prototyping (RPT) molds have been used. Very complex shapes, not possible by other methods, can be obtained using RPT. In this work, we have coupled the IG process with the gelcasting technique and evolved a process that can be used to fabricate complex-shaped components of REBCO with microstructures supporting high current densities. The thesis describes the development of 3-D components that support high current density. A hollow cylinder is fabricated to demonstrate this capability. The microstructural and magnetic properties of the gelcast YBCO are investigated. The gelcasting process has the important merit that nanoparticles can be introduced into shaped components without agglomeration using the NDSC method.

1.8. Organization of the Thesis

The present thesis is organized into six chapters. The contents of the chapters are as follows.

Chapter I gives a brief introduction to REBCO superconductors. It describes various techniques such as Melt Growth (MG) process and

Infiltration Growth (IG) process used to generate samples of REBCO superconductors supporting high current densities. The advantages offered by the IG process in comparison with the MG process, like the possibility of near net shape processing allowed by the former, of improved Y-211 morphology and distribution, etc. are brought out. The current densities obtained in the best MG and IG processed samples, and the process modifications used to obtain the same are discussed. It is demonstrated that, though the IG process has been used successfully in obtaining a variety of complex-shaped components which can prove very valuable in practice, the J_C in these materials is considerably lower than those obtained in melt processed samples. It is brought out from a study of the literature that substantially high current density is obtained only in those melt processed samples in which nanometer-sized pinning centers have been introduced.

The objectives of the present work are discussed in the chapter. They are to introduce nanoparticles of various materials into IG processed YBCO through NDSC process that allows their introduction without agglomeration. The samples are studied at various stages of processing. Microstructural and magnetic properties of samples are measured and discussed in comparison with the reports in the literature. Among the objectives of the thesis is the possibility of extending the NDSC process to the fabrication of relatively complex shapes through gelcasting.

Chapter II discusses the experimental techniques used in this work. These include the preparation of fine precursor powders of the required phases of the Y-Ba-Cu-O system through the citrate gel technique, and their characterization..

The IG processed samples are characterized by a study of their microstructural, electrical and magnetic properties. A homemade dc

electrical resistivity set up and ac susceptometer are used for the initial characterization. Microstructures of metallographically polished samples are studied using an optical microscope and a Field Emission Scanning Electron Microscope. Magnetic properties of the materials are studied using a Physical Property Measurement System,(PPMS), of Quantum Design-make.

The gelcasting technique is discussed along with a brief description of the techniques used for characterizing the powders and the slurry used for gelcasting. BET technique used for powder surface area measurements and zeta potential measurements to help develop stable suspensions are discussed.

Chapter III discusses preparation of nanoparticles of CeO_2, ZrO_2 and $BaCeO_3$ with a very narrow size distribution of around 30 nm through chemical route. The preparation of uniform, self standing slurries of Y-211 powder along with nano-sized powders of different materials (CeO_2, ZrO_2 and $BaCeO_3$) in an aqueous medium is discussed. Slurries with uniformly distributed nanoparticles form the starting material for the fabrication of preforms to be used in the IG process. YBCO superconducting composites are fabricated through IG process containing various amounts of the dopants. Microstructural observations using optical microscopy and Field Emission Scanning Electron microscopy allowed study of the distribution of various phases available in the IG processed samples. Energy Dispersive Spectroscopy (EDS) / Wavelength Dispersive Spectroscopy (WDS) studies on the YBCO composite were used for the identification of different phases in the microstructure. A detailed report on microstructural features such as pores, cracks, platelet gaps and characteristics of Y-211 inclusions (such as concentration, size, morphology and distribution) are presented in the thesis. Nanoparticle precipitates occurring in the Y-123 matrix are discussed. Twins

28

occurring in the matrix are also discussed. Samples at intermediate stages of processing are examined to (i) demonstrate that the NDSC process does indeed deposit nanoparticles on the Y-211 grains in the preforms without agglomeration and individually, and (ii) to understand the evolution of the final microstructures. The results are discussed in comparison with those from the literature on melt processed samples containing similar dopants. Mechanisms are proposed for the observed refinement / lack of refinement of Y-211 inclusions in the samples with various dopants at different concentrations.

Chapter IV details an investigation of the samples using dc electrical conductivity measurements and ac magnetic susceptibility measurements is presented. The current densities supported by the samples are estimated as function of applied magnetic field from dc magnetization measurements. The J_c versus H behavior of the samples is discussed in the light of the observed microstructures. The sample containing 10 wt. % CeO_2 showed a flat response in J_c to 9 Tesla. The J_c versus H behavior of the sample was examined in comparison with flux penetration into the sample measured at various applied dc magnetic fields using ac susceptibility measurement as a probe, and the results are discussed.

Chapter V initially discusses the gelcasting and rapid prototyping techniques as applied to ceramic materials such as alumina. Then it discusses the development of stable aqueous slurries Y-211 with sufficient solid loading for gelcasting. Aqueous slurries are preferred since Y-211 does not decompose in water as does Y-123 [86]. The slurries of Y-211 thus prepared are used to fabricate Y-211 preforms for use in Infiltration Growth processing. As a typical example, the fabrication of a hollow cylinder of YBCO with a microstructure similar to that of an IG processed material is discussed.

29

A specimen from the cylinder is characterized by dc magnetic studies to assess the field dependence of J_c, and the observations are correlated to the observed microstructural features.

Chapter VI summarizes the results obtained from different measurements and discusses the various conclusions drawn from the work presented in the thesis.

References

[1]   J. Bednorz and K. A. Muller, *Z. Phys. B: Cond. Matter.* **64 (**1986) 189

[2]   M. K. Wu, J. R. Ashburn, C. J. Torng, P.H. Hor, R. L. Meng, L. Gao, Z. J. Huang, Y. Q. Wang and C. W. Chu, *Phys Rev Lett* **58** (1987)908–910

[3]   H. Maeda, Y. Tanaka, M. Fukutomi and T. Asano, *Jpn J Appl Phys* **27** (1988) L209–L210

[4]   Z. Z. Sheng and A. M. Hermann, *Nature* **332** (1988)55–58

[5]   C. W. Chu, L. Gao, F. Chen, Z. J. Huang, R. L. Meng and Y. Y. Xue *Nature* **365** (1993) 323–325

[6]   J. Nagamatsu, N. Nakagawa, T. Muranaka, Y. Zenitani and J. Akimitsu, *Nature* **410** (2001) 63

[7]   O. Gunnarsson, *Reviews of Modern Physics* **69** (1997) 575-606

[8]   T. Y. Chen, Z. Tesanovic, R. H. Liu, X. H. Chen and C. L. Chien, *Nature* **453 (**2008) 1224-1226

[9]   A. A. Yurgens and N. V. Zavaritsky, *Physica C* **203** (1992) 277-283

[10]   http://en.wikipedia.org/wiki/File:Sc_history.gif

[11]   M. Murakami, N. Sakai, T. Higuchiz and S. I. Yooz, *Supercond. Sci. Technol.* **9** (1996) 1015–1032

[12]   http://www.fusione.enea.it/SUPERCOND/ybco.html.en

[13]   M. Murakami, *Supercond. Sci. Technol.* **5** (1992) 185-203 page no. 190

[14]   S. Jin, T. H. Tiefel, R. C. Sherwood, M. E. Davis, R. B. van Dover, G. W. Kammlott, R. A. Fastnacht and H. D. Keith, *Appl. Phys. Lett.* **52** (1988) 2074-2076

[15]   H. Kupfer, C. Keller, K. Salama adn K. Selvamanickam, *Appl. Phys. Lett.* **55 (**1989**)** 1903-1905

[16]   M. Murakami, M. Morita, K. Doi and K. Miyamoto, *Japan. J. Appl. Phys.* **28** (1989) 1189-1194

[17] H. Fujimoto, M. Murakami, S. Gotoh, N. Koshizuka and S. Tanaka, *Adv. Supercond.* **2** (1990) 285-288

[18] L. Zhou, P. Zhang, P. Ji, K. Wang, J. Wang and X. Wu, *Supercond. Sci. Technol.* **3** (1990) 490-492

[19] S. I. Yoo, N. Sakai, H. Takaichi and M. Murakami, *Appl. Phys. Lett.* **65** (1994) 633-635

[20] S. Takebayashi and M. Murakami, *Supercond. Sci. Technol.* **14** (2001) 741-747

[21] Salama Kamel and F. Lee Dominic, *Ceramics International* **22** (1996) 341-346

[22] M. Muralidhar, M. Jirsa, N. Sakai and M. Murakami, *Supercond. Sci. Technol.* **16** (2003) R1–R16

[23] B. Batlogg, *Physics Today* **44** (1991) 44

[24] C. Barry, *Journal of Electron Microscopy Technique* **8** (1988) 325–337

[25] M. Murakami, S. Gotoh, N. Koshizuka, S. Tanaka, T. Matsushita, S. Kambe and K. Kitazawa, *Cryogenics* **30** (1990) 390-396

[26] T. Rajasekharan, R. Gopalan and T. Roy, *Pramana - Jl. of Physics.* **37** (1991) L173-L177

[27] Y. Feng, J. G. Wen, A. K. Pradhan, N. Koshizuka,L. Zhou, S. K. Chen, K. G. Wang and X. Z. Wu, *Physica C* **363** (2001) 99-106

[28] E. Sudhakar Reddy and T. Rajasekharan, *Superconductor Science & Technology.,* **11** (1998) 523-534

[29] V. Seshubai and T. Rajasekharan, Chapter-III, "*Superconductivity : Recent Developments and New Production Technologies*" Nova Science Pub Inc 2012

[30] R. Gopalan, T. Roy, T. Rajasekharan, G. Rangarajan and N. Hari Babu, *Physica C* **244** (1995) 106-114

[31] E. Sudhakar Reddy and T. Rajasekharan, *J. Mater. Res.* **13** (1998) 2472-2475

[32] D. Dimos, P. Chaudhari and J. Mannhart, *Phys. Rev. B.* **41** (1990) 4038-4049

[33] M. Morita, S. Takebayashi, M. Tanaka, K. Kimura, K. Miyamoto and K. Sawano, *Adv. Supercond.* **4** (1991) 733

[34] E. Sudhakar Reddy, A. K. Singh, and T. Rajasekharan, *J. Mater. Res.* **14(6)** (1999) 2394-2398

[35] R. Miletich, M. Murakami, A. Preisinger and H. W. Weber, *Physica C* **209** (1993) 415 -420

[36] E. Sudhakar Reddy and T. Tajasekharan, *Supercond. Sci. Technol.* **11** (1998) 523–534

[37] N. V. N. Viswanath, T. Rajasekharan, N. Harish Kumar, L. Menonz and S. K. Malik, *Supercond. Sci. Technol.* **11** (1998) 420–425

[38] N. Hari Babu, T. Rajasekharan, Latika Menon and S. K. Malik, *J. Amer. Ceram. Soc.* **82** (1999) 2978-2984

[39] R. Cloots, T. Koutzarova, J. P. Mathieu and M. Ausloos, *Supercond. Sci. Technol* **18** (2005) R9-R23

[40] Y. L. Chen, H. M. Chan, M. P. Harmer, V. R. Todt, S. Sengupta and D. Shi, *Physica C* **234** (1994) 232-236

[41] J. P. Mathieu, T. Koutzarova, A. Rulmont, J. F. Fagnard, Ph. Laurent, B. Mattivi, Ph. Vanderbemden, M. Ausloos and R. Cloots, *Superconductor Science & Technology* **18** (2005) S136-S141

[42] H. Fang, Y. X. Zhou, K. Ravi-Chandar and K. Salama, *Supercond. Sci. Technol.* **7** (2004) 269–273

[43] N. D. Kumar, T. Rajasekharan and V. Seshubai, *Supercond. Sci. Technol.* **24** (2011) 085005-15

[44] Li. Guo-Zheng, Yang. Wan-Min, Cheng. Xiao-Fang, Fan. Jing, Dan. Xiao, *PRAMANA - Journal of Physics.* **74** (2010) 827-832

[45] A. Wongsatanawarid, H. Seki and M. Murakami, *Journal of Physics: Conference Series* **234** (2010) 012047 (1-7)

[46] Li. Guo-Zheng and Yang. Wan-Min, *J. Am. Ceram. Soc.* **93** (2010) 4033–4035

[47] Li. Guo-Zheng and Yang. Wan-Min, *J. Supercond Nov Magn.* **23** (2010) 429–432

[48] Li. Jguo-Zheng, Yang. Wan-Min, Cheng. Xiao-Fang, Fan. Jing and Guo. Xiao-Dan. *PRAMANA – J. Physics.* **74** (2010) 827-832

[49] H. Fang and K. Ravi-Chandar, *Physica C* **340** (2000) 261-268

[50] N. Hari Babu, K. Iida, Y. Shi and D. A. Cardwell, *Applied Physics Letters.* **87** (2005) 202506-08

[51] K. Iida, N. H. Babu, Y. H. Shi, D. A. Cardwell and M. Murakami, *Supercond. Sci. Technol.* **19** (2006) 641–647

[52] N. Hari Babu, Y. Shi, K. Iida and D. A. Cardwell, *Nature Materials.* **4** (2005) 476-480

[53] Li. Guo-Zheng, Yang. Wan-Min, Tang. Yao-Long and Ma. Jun, *Cryst. Res. Technol.* **45** (2010) 219 – 225

[54] E. S. Reddy and G. J. Schmitz, *Supercond. Sci. Technol.* **15** (2002) L21–L24

[55] J. G. Noudem, *J. Supercond Nov Magn.* **24** (2011) 105–110

[56] E. Sudhakar Reddy, J. G. Noudem, M. Tarka and G. J. Schmitz, *J. Mater. Res.* **16** (2001) 955-966

[57] K. Iida, N. Hari Babu, Y. Shi, T. Miyazaki, N. Sakai, M. Murakami and D. A. Cardwell, *Journal of Physics: Conference Series* **97** (2008) 012105 (1-5)

[58] Chen. Po-Wei, Chen. In-Gann, Chen. Shih-Yun and Wu. Maw-Kuen. *Supercond. Sci. Technol.* **24** (2011) 085021-28

[59] S. Umakoshi, Y. Ikeda, A. Wongsatanawarid, C. J. Kim and M. Murakami. M. *Physica C* **471** (2011) 843–845

[60] S. Meslin, C. Harnois, C. Chubilleau, D. Horvath, D. Grossin, E. R. Suddhakar and J. G. Noudem, *Supercond. Sci. Technol.* **19** (2006) S585–S589

[61] Y. H. Fujimoto, M. Murakami, N. Nakamura, S. Gotoh, A. Kondoh, N. Koshizuka and S. Tanaka, *Adv. Supercond. IV (Springer-Verlag, Tokyo)* (1992) 339

[62] Kim et al., *Journal of ceramics Processing Research* **7** (2006) 235

[63] J. Rignalda, X. Yao, D. G. McCartney, C. J. Kiely and G.J. Tatlock, *Mater. Lett.* **13** (1992) 357

[64] S. Jin, G. W. Kammlott, T. H. Tiefel, T. T. Kodas, T. L. Ward and D. M. Kroeger, *Physica C* **181** (1991) 57

[65]   D. Shi, S. Sengupta, J. S. Lou, C. Varanasi and P. McGinn, *Physica C* **213** (1993) 179

[66]   M. P. Delamare, I. Monot, J. Wang, J. Provost and G. Desgardin, *Supercond. Sci. Technol.* **9** (1996) 534–542

[67]   I. Monot, K. Verbist, M. Hervieu, P. Laffez, M. P. Delamare, J. Wang, G. Desgardin and G. Van Tendeloo, *Physica C* **274** (1997) 253-266

[68]   W. M. Yang, L. Zhou, Y. Feng, P. X. Zhang, M. Z. Wu, C. P. Zhang, J. R. Wang, Z. H. Du, F. Y. Wang, Z. M. Yu, X. Z. Wu, W. Gawalek and P. Gornert, *Physica C* **305** (1998) 269

[69]   Caixuan Xu, Anming Hu, Naomichi Sakai, Mitsuru Izumi and Izumi Hirabayashi, *Physica C* **445** (2006) 357

[70]   Chan-Joong Kim, Najam ul Qadir, Asif Mahmood, Y. H. Han and T. H. Sung, *Physica C* **463–465** (2007) 344–347

[71]   Chan-Joong Kim, Ki-Baik Kim, Dong-Yeon Won, Hong-Chul Moon, Dong-Soo Suhr, S. H. Lai and P. J. McGinn, *J. Mater. Res.* **9** (1994) 1952

[72]   T. R. Chien, Z. Z. Wang and N. P. Ong, *Phys. Rev. Lett.* **67** (1991) 2088

[73]   A. Wahl, M. Hervieu, G. Van Tendeloo, V. Hardy, J. Provost, D. Groult, Ch. Simon and B. Raveau , *Radiat. Eff. Defects Solids.* **133** (1995) 293

[74]   H. W. Weber, H. P. Wiesinger, W. Kritscha,F. M. Sauerzopf, G. W. Crabtree, J. Z. Liu, Y. C. Chang and P. Z. Jiang, *Critical Currents In Neutron-Irradiated YBCO And BiSCO Single-Crystals*, Adam Hilger Ltd, Bristol (1991)

[75]   H. W. Weber, H. P. Wiesinger, W. Kritscha,F. M. Sauerzopf, G. W. Crabtree, J. Z. Liu, Y. C. Chang and P. Z. Jiang, *Critical Currents In Neutron-Irradiated YBCO And BiSCO Single-Crystals*, Adam Hilger Ltd, Bristol (1991)

[76]   N. Moutalibi, A. M'chirgui and J. Noudem, *Physica C* **470** (2010) 568–574

[77]   Y. Zhao, C. H. Cheng and J. S. Wang, *Supercond. Sci. Technol.* **18** (2005) S43–S46

[78]   N. Hari Babu, E. S. Reddy, D. A. Cardwell, A. M. Campbell, C. D. Tarrant and K. R. Schneider, *Appl. Phys. Lett.* **83** (2003) 23

[79]   P. Diko and K.C. Goretta *Physica C* **297** (1998) 211–215

[80]   D.A. Cardwell and N. Hari Babu, *Physica C* **445–448** (2006) 1–7

[81]   T. Meignan, A. Banerjee, J. Fultz and P. J. McGinn, *Physica C* **281** (1997) 109-120

[82]   M. Muralidhar, N. Sakai, M. Jirsa, M. Murakami and I. Hirabayashi, *Appl. Phys. Lett.* **92** (2008) 162512

[83]   N. Devendra Kumar, T. Rajasekharan, K. Muraleedharan, A. Banerjee and V. Seshubai, *Supercond. Sci. Technol.* **23** (2010) 105020

[84]   C. J . kim, Il hyun kuk, Gye Won Hong, Tae hyun Sung, Sang Chul Han and Jin Joong kim, *Material letters* **34** (1998) 392-397

[85]   N. Vilalta, F. Sandiumenge, S. Pinol and X. Obradors, *J. Mater. Res.* **12** (1997) 1

[86]   M. F. Yan, R. L. Barns, H. M. O'Bryan Jr., P. K. Gallagher, R. C. Sherwood and S. Jin, *Appl. Phys. Lett.* **51** (1987) 532
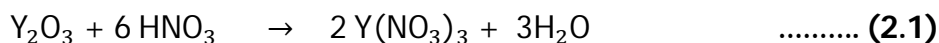
Experimental Techniques

This chapter presents sample preparation and characterization techniques used in the present work.

2.1. Preparation and characterization of precursor powders

2.1.1. Citrate synthesis method

The $YBa_2Cu_3O_7$ (Y-123) and Y_2BaCuO_5 (Y-211) powders were synthesized following a chemical route employing citrate precursors [1, 2]. The citrate synthesis route was chosen because of expected fine particle size and better homogeneity in the final product as compared to the solid state route [3, 4].

Y-123 and Y-211 powders were prepared from Yttrium Oxide (Y_2O_3) of Indian Rare Earth-make (purity -99.9 %), Barium Carbonate ($BaCO_3$) and Copper Oxide (CuO) of E-merck make, and both of them of 99.99 % purity. They were weighed out in stoichiometric ratios and were dissolved in nitric acid to make corresponding nitrates as shown below:

$$Y_2O_3 + 6\,HNO_3 \quad \rightarrow \quad 2\,Y(NO_3)_3 + 3H_2O \qquad .... \textbf{(2.1)}$$
$$BaCO_3 + 2\,HNO_3 \quad \rightarrow \quad Ba(NO_3)_2 + H_2O + CO_2 \uparrow \qquad .... \textbf{(2.2)}$$
$$CuO + 2\,HNO_3 \quad \rightarrow \quad Cu(NO_3)_2 + H_2O \qquad .... \textbf{(2.3)}$$
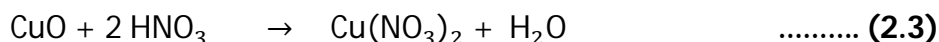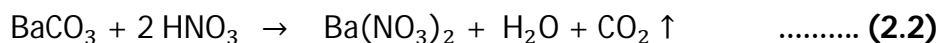
Requisite amount of citric acid was added to the nitrate precursor solution along with a small amount of chelating agent 'Ethylene glycol'. The pH of the solution was adjusted to 8 by adding appropriate amounts of ammonia (NH_4OH). A gel was formed by evaporating the clear solution which

was heated to about 250 °C. Spontaneous combustion of the gel then generated a voluminous material.

Submicron-sized powders thus obtained were heated for 12 hours at 900 °C and 950 °C to form Y-123 and Y-211 compounds respectively. Formation of the correct phase was confirmed by X-ray diffraction. The particle size of the Y-211 thus obtained was observed using a Scanning Electron Microscope (SEM) after dispersing them in ethanol medium. The particles were observed to be in the size range of 1-2 μm as shown in Fig. 2.1.
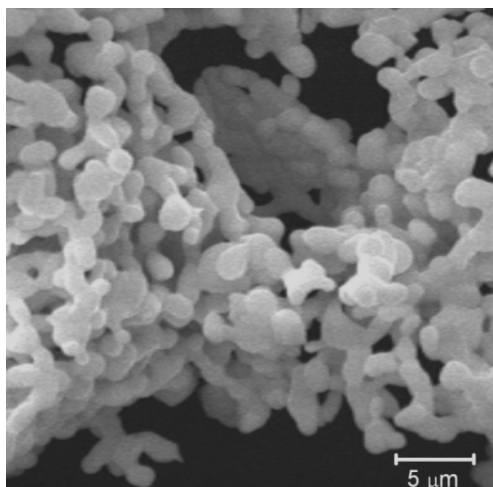
Fig.2.1. A scanning electron micrograph obtained from sintered Y-211 powder used in the present experiments is shown. The micrograph shows that the size of the Y-211 particles is around 1-2 μm.

2.1.2. Furnaces used

In the present work, two different furnaces were employed, one for sintering the precursor powders of Y-123 and Y-211, and also for the Infiltration Growth (IG) process. The second was used for oxygenating the IG processed samples. Both the furnaces were home-made and had tubular muffles made of re-crystallized alumina (Al_2O_3). Kanthal APM wires were used as heating elements. Chromel–Alumel thermocouples were used for

temperature measurements. Eurotherm-make temperature controllers (model 2404) and thyristors (model TE10A) were used for controlling the temperature in the furnaces to an accuracy of $\pm$ 1 $^{\circ}$C. In the case of oxygenation furnace, a long quartz muffle of length ~ 100 cm was introduced into the alumina muffle. The quartz muffle of the furnace after loading with the samples was sealed with rubber cork and plaster of Paris cloth and further sealed with Teflon tapes. A schematic picture of the furnace along with the temperature controller and thyristor are shown in Fig. 2.2. The samples were heated in oxygen atmosphere at 460 $^{\circ}$C for 100 hours. The temperature in the furnace was controlled by a temperature controller and thyristor of West-make. During the oxygenation process, the Y-123 phase undergoes a transformation from tetragonal state to orthorhombic state .
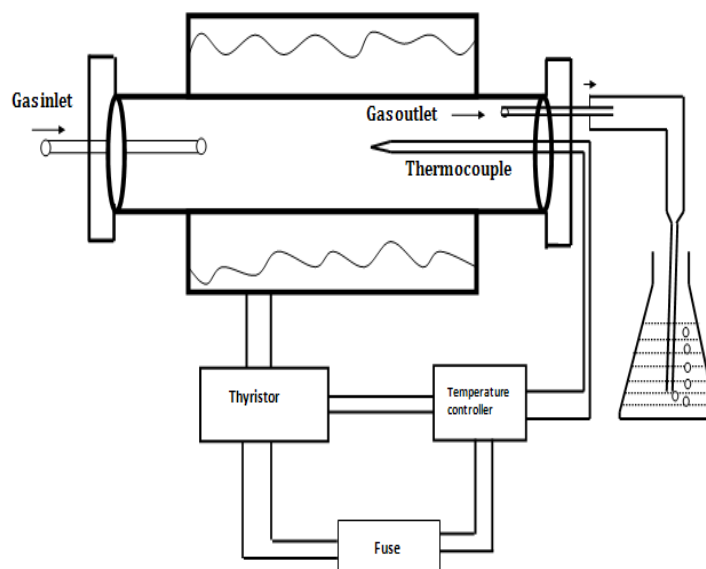
Fig. 2.2. A schematic diagram of the furnace used.

The heat profiles obtained by measuring the temperature as a function of length in the muffles of the furnaces are shown in Figs. 2.3 (a) and (b).

39
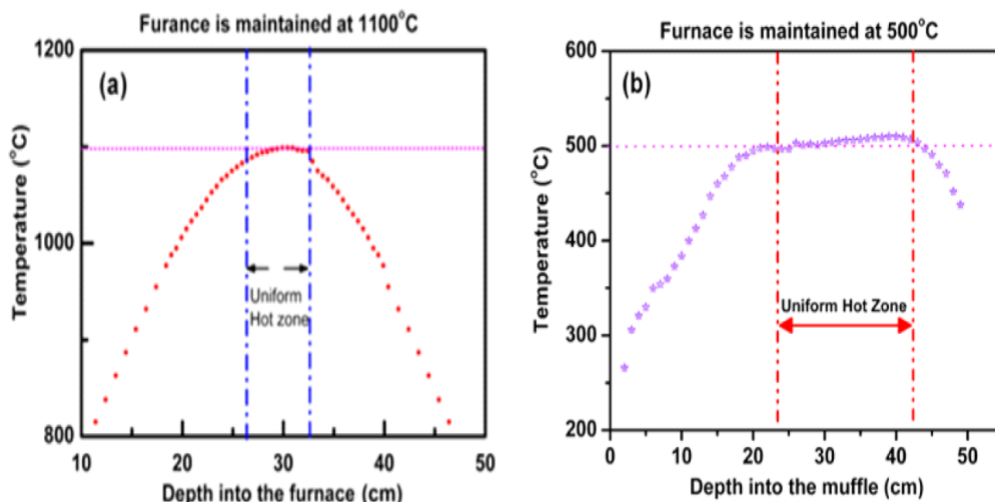
Fig. 2.3. The heat profiles showing the temperature distribution obtained along the length of the muffle in tubular furnaces used for **(a)** sintering / IGP and **(b)** oxygenation.

2.1.3. X-ray Diffractograms of sintered Y-123

When a parallel monochromatic beam of X-rays of approximately 0.1 nm wavelength strikes a crystal, the crystal acts as a three-dimensional diffraction grating and produces an X-ray diffraction pattern. This diffraction pattern comprises of a three dimensional array of reflections which satisfy the condition of Bragg's law:

$$2d \sin\theta = n\lambda \dots\dots (2.4)$$

where 'n' represents the order of diffraction, λ represents the wavelength of the X-rays, 'd' is the perpendicular distance between a set of parallel lattice planes and 'θ' is the angle between the incident X-ray beam and the corresponding atomic lattice planes in the crystal .

The reflection angle for a particular set of lattice planes (hkl) is

$$2\theta = 2\sin^{-1}\left(\frac{\lambda}{2d_{hkl}}\right) \dots\dots \textbf{(2.5)}$$

where (hkl) are Miller indices defining the orientation of the plane with respect to the crystallographic axes. In general, the powder X-ray diffraction pattern is a set of first order reflections in which the lattice spacing and relative intensities are unique from each crystalline substance.

X-ray diffractograms were recorded on the sintered powders of Y-123 and Y-211 to confirm their phase formation. Copper K_α radiation with wavelength (λ) of 1.5414 Å was used. An X-ray diffractometer of Phillips-make was used for this purpose. Indexed pattern obtained for $YBa_2Cu_3O_{6.5}$ is shown in Fig. 2.4.
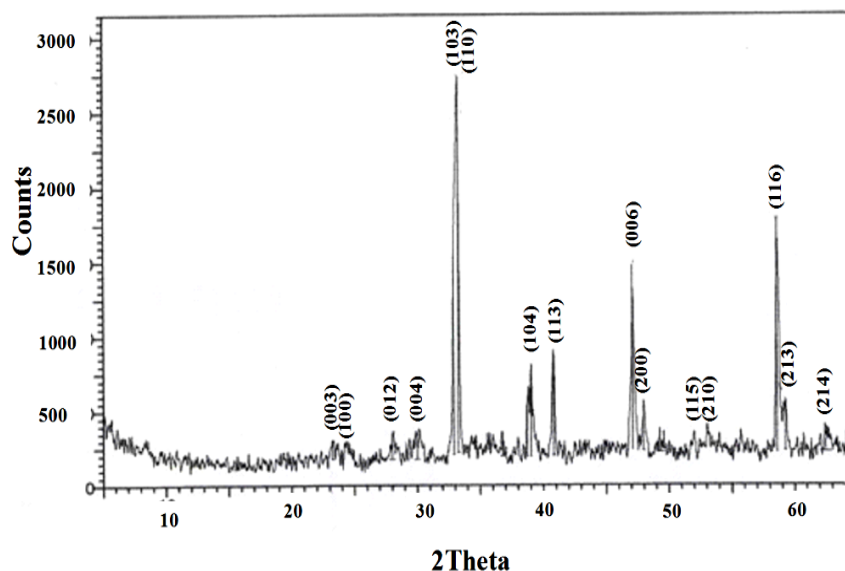
Fig.2.4. X-ray diffractogram obtained from sintered powders of $YBa_2Cu_3O_{6.5.}$ The pattern could be indexed to a tetragonal unit cell (JCPDS file no 88-2462).

2.2. Infiltration and Growth Processing of YBCO superconductors

In Chapter I, the Infiltration Growth (IG) process and its characteristics have been reviewed. In this section, we discuss the experimental steps involved in carrying out the IG process. We have followed

the optimized process steps evolved and reported elsewhere . The first step is the fabrication of an appropriate preform.

In order to fabricate the preforms, sintered powders of Y-123 and Y-211 were compacted into pellets of dimensions of 16 mm X 16 mm X ~ 15 mm and 16 mm X 16 mm X ~ 8 mm respectively by applying uniaxial pressure. For this purpose, a hydraulic press was used. The preforms were made at an optimum compaction pressure of 460 MPa. The preparation of sample assembly for IG process is illustrated in Figs. 2.5 (a), (b) and (c).
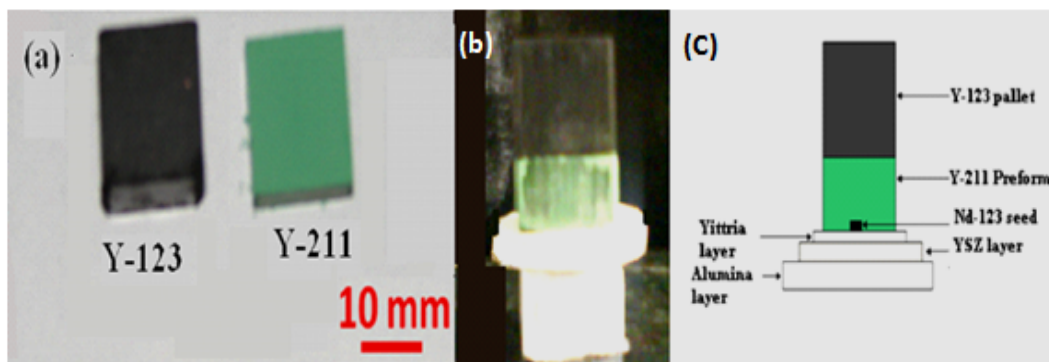
Fig.2.5. (a) Photographs of pellets of Y-123 (black in color) and Y-211 (green in color) are fabricated under pressure of 460 MPa. **(b)** Y-123 and Y-211 pellets are arranged for IG process. The schematic picture in **(c)** shows the sample assembly used in the IG process. The liquid phase source and preform pellets are supported on a layer of Y_2O_3 which in turn are supported on YSZ and alumina layers.

The Y-211 preform is supported on thin layers of Y_2O_3, Yttria-Stabilized Zirconia (YSZ) and alumina (Al_2O_3) to minimize the outflow of liquid phases during heat treatment. The presence of Y_2O_3 and YSZ layers also helps in avoiding contamination of the sample by alumina at elevated temperatures. Y-123 pellet, which is the source of liquid phases, is placed above the Y-211 preform. Nd-123 seeds fabricated following a procedure reported by Hari Babu et al. were used to promote textured growth of Y-123 during IG process.

The sample assembly arranged as described above is heat-treated in a tubular furnace, which has a uniform hot-zone of ~ 60 mm. It is heated to 950 °C at a rate of 150 °C per hour, followed by a 4 hour dwell at that temperature for sintering the preform . The temperature is then ramped to 1100 °C and maintained there for 1 hour to ensure sufficient infiltration of liquid phases into the Y-211 preform. The samples are then quickly cooled to 1010 °C, and then cooled very slowly (at 0.5 °C per hour) through the peritectic formation temperature of Y-123 (T_p~1008 °C) to 980 °C. They are maintained there for 48 hours to ensure complete grain growth of Y-123, and are then furnace-cooled to room temperature. The heat treatment schedule followed is shown in Fig. 2.6. The IG processed samples prepared as above were characterized as discussed below.
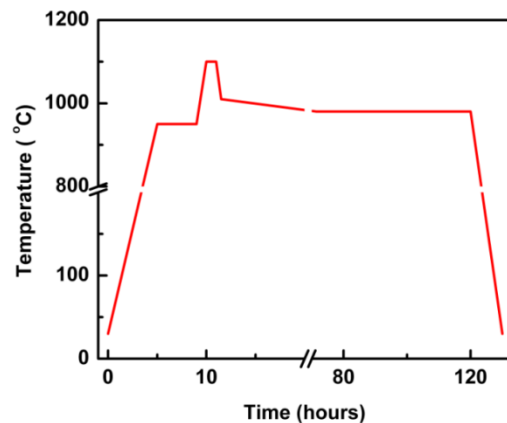
Fig.2.6. Time–Temperature profile followed for the fabrication of YBCO bulk superconductors by Infiltration Growth (IG) process.

2.3. Microstructural characterization

In order to prepare specimens for microstructural characterization, the samples were sliced into thin sections using a low speed diamond saw (model Isomet 1000, Buehler-make). The specimens extracted from the samples were mounted in bakelite and ground on silicon carbide papers

(600, 800, 1000 and 1200 grits) to a flat surface. They were further polished on polishing cloth on the rotating wheel of a Buehler polishing machine, using different grades (6, 3, 1, 0.25 μm) of diamond paste as grinding media. Kerosene was used as a lubricant during polishing. The surface was cleaned after every stage of polishing. Polishing time at each stage ranged from 2 to 30 minutes with silicon carbide paper and 0.5-2 hours with diamond paste. The polished surface of the sample was then cleaned with methanol and dried in hot air. In the present study, no etching was done to the polished surface of the samples. The micrographs thus obtained were characterized for various microstructural parameters using quantitative metallographic methods as explained below.

2.4. Field Emission Scanning Electron Microscopy (FE-SEM)

The Scanning Electron Microscope (SEM) employs a high-energy (in keV) electron beam and helps in imaging the topography of the sample surface by operating in a raster scan mode . In the case of a Field Emission Scanning Electron Microscope (FE-SEM), a field-emission cathode in the electron gun of a SEM provides narrower probing beams at low as well as high electron energy, resulting in both improved spatial resolution and minimized sample charging and damage. The electrons, when they interact with the atoms of the sample, produce secondary electrons, back-scattered electrons, transmitted electrons, characteristic X-rays etc.. A typical schematic sketch representing the above mentioned processes are shown in Fig. 2.7(a). Separate detectors are present to pick up the information from each of these processes (see Fig. 2.7(b)).

The secondary electron imaging can produce very high-resolution images of a sample surface, revealing details even in the size range 10 - 100

nm. Due to the very narrow electron beam, SEM micrographs have a large depth of field yielding a characteristic three-dimensional appearance useful for understanding the surface structure of a sample. Back-scattered electrons (BSE) are beam electrons that are reflected from the sample by elastic scattering. BSE are often used along with the spectra made from the characteristic X-rays. Since the intensity of the BSE signal is strongly related to the atomic number (Z) of the specimen, BSE images can provide information about the distribution of different elements in the sample. It also provides information about different phases present in the sample based on the variations in reflectivity.
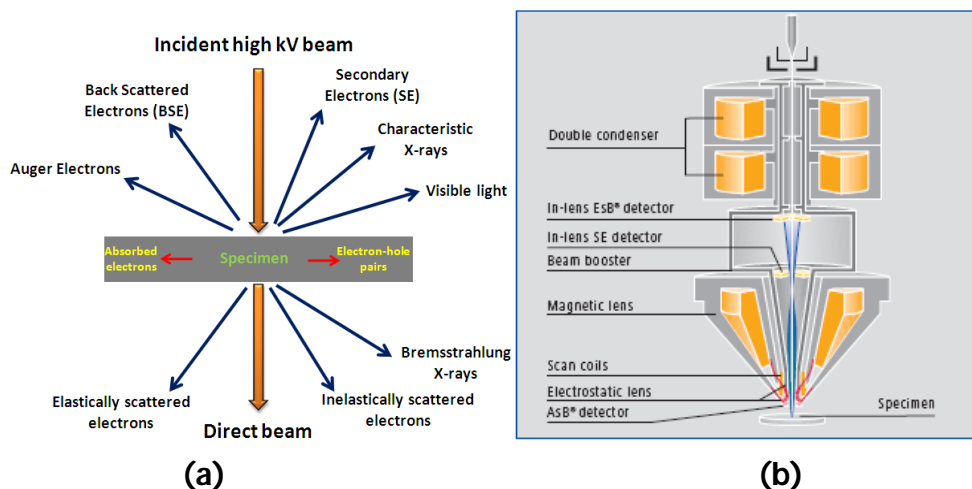
Fig.2.7. (a) A schematic picture showing generation of various radiations when a high energy electron beam gets incident on a material **(b)** A schematic picture showing emission of electron beam and presence of various detectors in a Scanning Electron Microscope (SEM).

Electron beam of very high energies are employed in order to visualize the sub-surface structures while low energy BSE detection is quite useful for high resolution investigation of critical/charging specimens. This is met through a new In-lens BSE detection system. In order to reduce aberrations and sensitivity to interfering stray-fields the electron optical

column is equipped with a positively biased booster that shifts the energy of the primary electrons. The incident beam is focused by a combination of a magnetic lens with an axial gap that avoids field leakage to the specimen and an electrostatic retarding together with the grounded pole piece cap. Shortly before the electrons hit the specimen they are decelerated down to the desired primary energy. A suitable explanation for the reduction of spherical and chromatic aberrations is that the electron beam is focused by the objective lens at higher energies and smaller electron beam diameters. Another advantageous effect of this arrangement is the collection of secondary electrons emerging from the sample surface attracted and accelerated by the positively biased electrode of the beam booster and finally projected onto the In-lens detector.

Characteristic X-rays are emitted when the electron beam removes an inner shell electron from the sample, causing a higher energy electron to fill the shell and release energy. These characteristic X-rays are used to identify the composition and measure the abundance of elements in the sample.

In the Present work, a Field Emission Scanning Electron Microscope (model Ultra 55, Carl Zeiss-make) was employed for obtaining the micrographs. The working distance for most of the cases was in the range 4 - 10 mm. The charging effects of the electron beam on the sample were bypassed by either gold coatings or by creating a silver paint / strip channel from the holder to the sample. FE-SEM with Energy Dispersive Spectrometry (EDS) and Wavelength Dispersive Spectrometry (WDS) attachments was employed in the present study. WDS can detect the presence of elements to a greater accuracy compared to EDS.

2.5. Gelcasting technique

Gelcasting is a novel process of consolidating powders of metal and ceramics into complex shaped articles. Gelcasting technique was first developed by Omatete et al. -12] in Oakridge National Research Laboratory (ONRL) in 1991. In this process, slurry made up of ceramic powder in an aqueous or non-aqueous media along with organic monomers and dispersant is cast into a mold and polymerized to form a wet gelled part. The gelled part is then dried under humidity controlled atmosphere to avoid crack formation and sintered to final density. The flow chart of the process is given in Fig. 2.8.
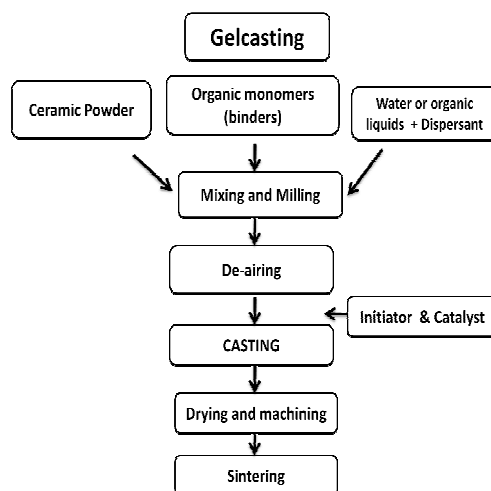
Fig.2.8 Flow chart representing various steps involved in gelcasting process.

Gelcasting involves preparation of slurries with very high solid content (~40-60 vol. %) and casting them into molds. To attain high solid content it is necessary to understand the effect of size and morphology of particles on stability and flow behavior of the slurry. Selection of proper dispersant is also very important; dispersants attach to the surface of the particles and prevent them from being agglomerated through electrostatic, steric or electro-steric stabilization.

2.5.1. Characterization of powders

The particles need to have spherical morphology in order to prevent interlocking while tumbling and casting and preferably of single particle size distribution. If the surface area is large i.e. for finer particles more of dispersant will be required; too large a quantity of dispersant can lead to coagulation instead of dispersion of particles and will also complicate the debinding process. For small surface area i.e. for larger and heavier particles, electrostatic or electro-steric repulsion need to compete with the gravitational force in order to keep them from settling down. Hence the surface area and the charge on them plays vital role in deciding the optimal size of the particles to be used.

2.5.1.1. BET surface area measurements

Nitrogen physisorption is useful in the determination of specific surface area and pore volume in microporous (< 2 nm) and mesoporous (2-50 nm) materials. When a vapor of a condensable gas (e.g. N_2 or He) is brought in contact with porous media at constant temperature, several mechanisms of adsorption occur successively on the surface of the pore, as the relative pressure (say, N_2) increases from zero to unity.

During adsorption, the amount of gas needed to form a monolayer or to fill the pores in various sizes can be measured as a function of gas pressure and such a plot is referred to as gas adsorption isotherm. The type of adsorption isotherm is mainly determined by the pore size and the pore uniformity. The BET method (Brunauer-Emmet-Teller) is then used to determine the surface area of the material by using the following equation.

$$A_s = (V_m/22414) \, N_a\sigma \, \text{..........} \, \textbf{(2.6)}$$

Chapter II
Experimental Techniques

where V_m is the monolayer nitrogen volume, N_a is Avogadro number and σ is cross sectional area of one nitrogen molecule (0.162 nm^2). The adsorption at p/p_0 value of 0.3 forms a monolayer and at this partial pressure, the specific surface area can be calculated from the volume of adsorbed nitrogen.

Fig. 2.9 Quantumchrom made BET surface area measurement system.

Zeta potential

The electrical potential that exists at the boundary of slipping plane, a plane between dispersion media and a stationary layer of fluid attached to the particles, in a colloidal solution is known as zeta potential see Fig. 2.10. Zeta potential determines the stability of the particles in a colloidal solution. Zeta potential is affected by the pH of the colloidal solution. Zeta potential versus pH curve will determine the optimal pH at which the zeta potential is more and aid in stability to the suspension of colloidal particles.
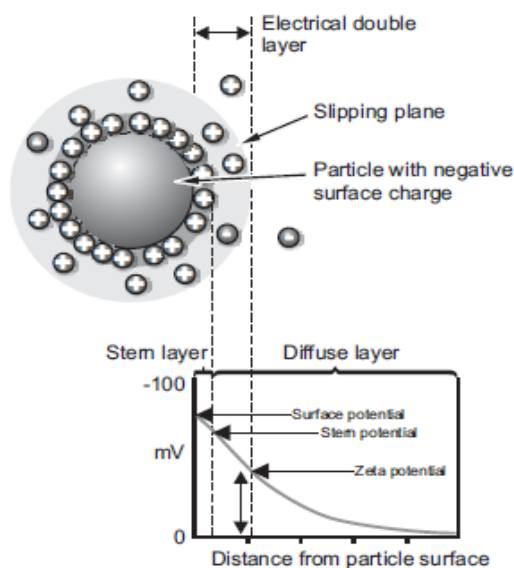
Fig. 2.10 Schematic illustration of zeta potential and slipping plane.

A typical zeta potential versus pH plot is given in Fig. 2.11, the zeta potential value gradually changes from either positive maximum to a negative maximum through zero or vice versa. The point where zeta potential vanishes is called isoelectric point. At isoelectric point, no charge is present on the particles hence they can easily coagulate and settle down. To obtain well dispersed slurry/colloidal solution one need to know the isoelectric point and the maximum zeta potential values so that pH of the slurry/colloids can be adjusted to keep them from settling down.

The Laser Doppler Velocimetry (LDV) technique is used to measure the zeta potential on the powder particles. LDV technique is well known in fluid dynamics where the velocity of the particles in the fluid is measured. The powder particles are dispersed in fluid media and an electric field is applied across the media containing powder particles. The powder particles start moving under the influence of the electric field and a laser beam is shined on the moving powder particles. The laser beam scattered from the

moving particles is combined with the reference beam to get a fluctuating signal where the rate of fluctuation is proportional to the speed of the particles and the fluctuating signal is analyzed with a digital signal processor to obtain the zeta potential from the calculated velocity of the particles.
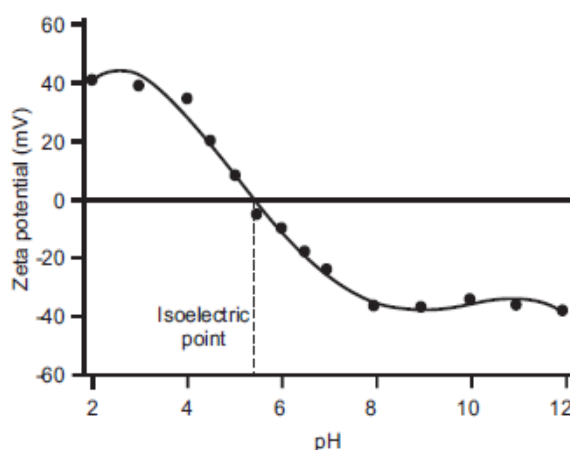
Fig.2.11 A plot indicating variation of zeta potential with respect to pH. The pH value at which zeta potential vanishes is called isoelectric point. In order to attain uniform and well dispersed suspension, pH of the solution should be away from isoelectric point.

2.5.2. Dispersant optimization

As described in previous section the dispersant plays a crucial role in attaining high solid loading in the slurry. In order to optimize dispersants preliminary test such as flow point and sedimentation tests were carried out.

2.5.2.1. Flow point measurement

Flow point determines the amount of dispersant required for a given powder particle system to flow in minimum amount of dispersing media . At first, various amounts (~0.5-1.5 wt. % of the powder) of dispersant are mixed with the powder and then dispersing medium is added drop wise. The point

where the entire powder starts to flow i.e. a sharp transition from wet powder to flowing mass is known as flow point. Such a sharp transition indicates that the particles are separated by a fine layer of dispersing medium. If a gradual transition takes place, then the dispersant is not effective in keeping the particles separate. This measurement also helps to determine the amount of dispersing medium and the dispersant required.

2.5.2.2. Sedimentation test

Sedimentation test described by Janney et al. was carried out in the present study to identify the appropriate dispersant and its ability to disperse the particles in the slurry for a long durations. The dispersant found to be best in flow point test were mixed thoroughly with the ceramic powder in a tumbling mill for 12 hours and kept in transparent tubes for a relatively long duration and were monitored. The best dispersant is the one which can keep the particles dispersed for a long time i.e. for more than 12 hours and when the slurry starts settling it should separate into a compact mass with a clear solution.

2.5.2.3. Viscosity measurement

The crux of gelcasting process lies in preparing low viscous slurries with high solid content (~40-60 vol. %). Flow point measurement and sedimentation test can give an approximate estimation of the dispersant. But the true measure of flow behavior of the slurries is obtained from their viscosity.

The viscosity of the slurries is measured using a rotational viscometer (Soft Solid Tester of Brook field-make). Rotational viscometer operates on the principle of measuring the rate of rotation of a solid shape in a viscous medium upon application of a known force or torque required to rotate the

solid shape at a definite angular velocity. Although rotational viscometers are more elaborate than the capillary type during operation and often less accurate for Newtonian liquids, they have several advantages that make them attractive particularly to study the flow properties of non-Newtonian materials. Some of the advantages are: measurements under steady state conditions, multiple measurements with the same sample at different shear rates, continuous measurement on materials whose properties may vary as a function of temperature and that small or no variation occurs in the rate of shear within the sample during a measurement.

A number of rotational viscometers with different designs are available commercially. These viscometers can be classified into three general categories based on their design configuration.

1. Coaxial-Cylinder Viscometer
2. Cone and Plate Viscometer
3. Coni-Cylinder Viscometer

In the present study Coaxial-Cylinder Viscometer (Soft Solid Tester of Brook field-make) was used. The basic principle of a Coaxial-Cylinder Viscometer is discussed in brief and the schematic is shown in Fig. 2.12.

It consists of an inner cylinder (which is also called a bob) of radius R_1 and height h, and an outer cylinder or cup of radius R_2. The inner cylinder is stationary. The outer cylinder that contains the test sample is rotated at a constant speed (Ω rad/sec). The resultant torque (T dyne cm) is measured by the angular deflection of the inner cylinder that is suspended by a fine wire. The velocity of the outer cylinder can be varied to obtain the data on the change in viscosity of the fluid with the shear rate.
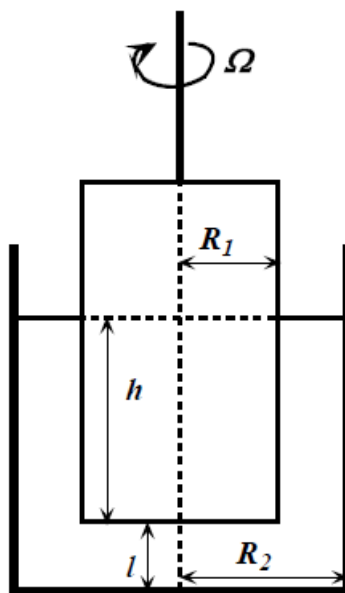
Fig.2.12 A schematic of the Coaxial-Cylinder Viscometer.

The dynamic viscosity (η) of fluid may be obtained from the following expression.

$$T = \frac{4\pi R_1^2 R_2^2 h\eta\Omega}{R_2^2 - R_1^2} = C\eta\Omega \qquad \text{.......... (2.7)}$$

where C is a constant specific to the instrument.

Eq. 2.7 actually provides the torque exerted by the liquid on the curved surface of the inner cylinder and suggests that the viscosity is directly proportional to the ratio of torque to angular velocity.

2.5.3. Binder removal

Gelled parts in gelcasting process after the polymerization is over, contains nearly 50 vol. % of solvent with a freshly formed network of polymers. Sudden removal of solvent from the gelled part can crumble the

weak gelled parts. In order to avoid the crumbling of the gelled parts, the solvent needs to be removed in a controlled manner.

2.5.3.1. Controlled subcritical drying

Sub-critical drying process is adopted to dry the gelled parts where drying is done under humidity controlled atmosphere. Initial humidity was kept very high (~95 %) and the temperature was around 50 °C in order to cause a slow evaporation of solvent from the gelled parts and gradually decreasing the humidity with increasing temperature. The whole drying process can take ~ 70-100 hours to completely remove the solvent from the gelled part.

2.5.3.2. Thermogravimetric Analysis (TGA)

Gelcast green parts, after the removal of solvent, contain lesser amount of binders (~5 wt. %) when compared to other ceramic processing techniques. These binders are removed either by dissolving them in a suitable solvent (mostly organic solvents) or by thermal debinding process. Thermal debinding process is more convenient for large scale production and to some extent eco-friendly, if done carefully after studying the decomposition processes and the final products after decomposition of the various organics in the binder system. Most of the organics used in the present study can decompose into CO_2 and NO_2 during debinding stage.

TGA was used to study the decomposition of various components of organic binders system. Fig.2.13 provides a schematic of TGA set up. In TGA, sample is heated at certain heating rate and the change in the weight of the sample is measured using a highly sensitive balance.
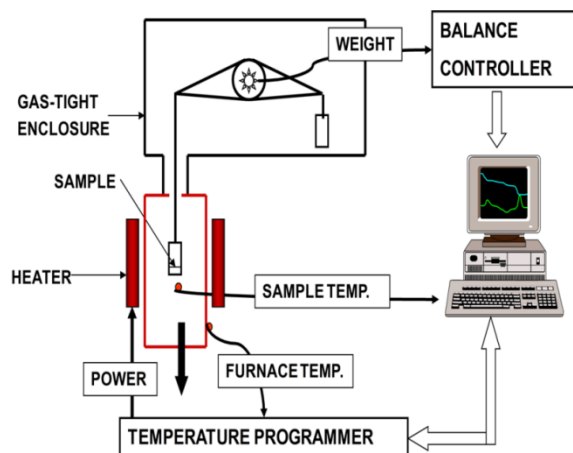
Fig 2.13 A schematic of TGA set up used for the analysis of the binder removal in gelcast green part.

2.6. Electrical resistivity measurement

The temperature dependence of dc electrical resistivity (ρ) was obtained by employing four probe technique to determine the critical temperature (T_c) and transition widths (ΔT_c) of the samples under study. A sample holder assembly was fabricated to measure electrical resistance as a function of temperature. A programmable constant current source (model 224, Keithley make) was used to send a constant dc current through the sample and a nano-voltmeter (model 181, Keithley make) was used to measure the voltage drop across the sample. Temperature of the sample was measured by placing a Platinum sensor (PT-100) in the close vicinity of the sample. The temperature of the sample was measured and controlled using a cryogenic temperature controller (model DRC-93C, Lakeshore make) with heater attachment. The temperature controller can measure temperature with an accuracy of 10 mK.

A schematic sketch showing the connections made is presented in Fig. 2.14. Typical sample puck and sample holders made for this purpose are shown in Fig. 2.15.
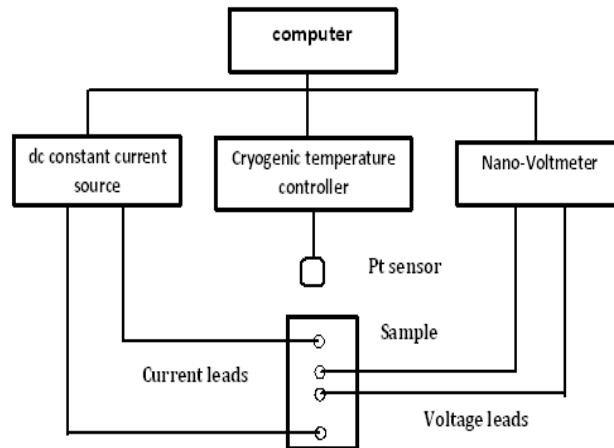
Fig. 2.14. Block diagram for measuring dc electrical resistivity.

Fig.2.15. The sample holder fabricated for measuring electrical resistance of superconductors is shown. The sample puck and the heater cavity made can also be seen in the figure.

In order to avoid thermal effect contributions, current at every temperature was reversed during the measurement for thermo-emf corrections.

$$\text{Resistance (R)} = \frac{V^+ - V^-}{I^+ - I^-} = \frac{V^+ - V^-}{2I} \quad \dots\dots\dots \text{(2.8)}$$

where

V^+ : voltage obtained when positive current (I^+) is sent through the sample

57

V⁻ : voltage obtained when negative current (I^-) is sent through the sample

I : current flowing in the sample

The thermo-emf corrections are made by reversing the current flow through the sample and by measuring the voltage drop across the leads. The difference of V⁺ and V⁻ gives the information on the resistance of the sample.

$$V^+ = V_S + V_{Th}$$ .... **(2.9)**

$$V^- = -V_S + V_{Th}$$ .... **(2.10)**

$$V^+ - V^- = V_S + V_{Th} - (-V_S + V_{Th}) = 2 V_S$$ .... **(2.11)**

$$R = \frac{V^+ - V^-}{2I} = \frac{V_S}{I}$$ .... **(2.12)**

where V_S is the voltage drop across the sample and V_{Th} is the thermo-emf voltage developed due to passage of current (heating effects).

2.7. Magnetic characterization

2.7.1. ac susceptibility measurements

A block diagram of the set up used for measuring susceptibility as a function of temperature of a sample is shown in Fig. 2.16.

In the ac magnetic measurements, a small ac drive magnetic field is applied causing a time-dependent moment in the sample. The field of the time-dependent moment induces a current in the pickup coils, allowing measurement without the sample motion. The detection circuitry is configured to detect only in a narrow frequency band, normally at the fundamental frequency (that of the ac drive field).
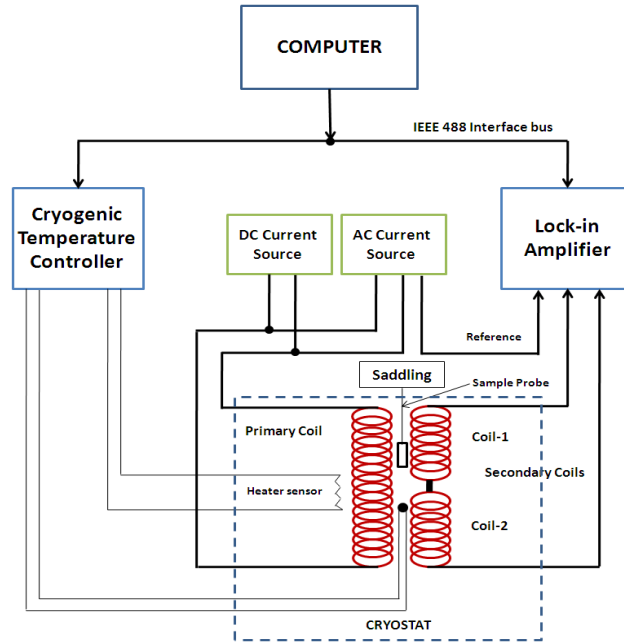
Fig. 2.16. Block diagram for ac susceptibility measurement.

If the applied ac voltage is $H = H_o \cos \omega t$, where ω is the angular frequency ($=2\pi f$), the resulting magnetization amounts to

$$M = H_o(\chi' \cos \omega t + \chi'' \sin \omega t) \text{.......... (2.13)}$$

where χ' and χ'' represent the real and imaginary components of the fundamental ac susceptibility.

The fundamental principle on which this measurement works is based on the mutual induction (Faraday's law)

$$\nabla \times E = -\frac{\partial \mathbf{B}}{\partial t} \text{.......... (2.14)}$$

Basically the assembly comprises of a mutual inductance coil assembly with two secondary coils co-axially mounted in a primary solenoid. The two secondary coils are identical and are connected in opposition in order to cancel the voltages induced by the ac field itself. A constant current

source is employed to drive an ac current in the primary solenoid. The field produced by a current with r.m.s. value 'I_{rms}' in a solenoid is given by

$$H_{rms} = \frac{\mu_o N_p I_{rms}}{L_p} \quad .... \textbf{(2.15)}$$

where N_p is the number of turns in the primary coil, L_p is the length of the primary coil (in cm) and I_{rms} is the root mean square (rms) value of the ac current through the primary coil. The field amplitude H_{ac} (in Oe) is $\sqrt{2}\, H_{rms}$.

If the secondary coils are ideally made i.e. both the coils are made under similar conditions (number of turns, diameter, etc.), no voltage will be detected by the lock-in amplifier when the coil assembly is empty. But, in practice, the net output from the secondary coils is often non-zero and is temperature dependent. This is eliminated by measuring and subtracting the back ground voltage from the signal measured after introducing the sample in similar conditions. Additionally, there is a need to correct the extraneous phase shifts arising from various sources in the setup. This is done by shifting the phase of the references so as to obtain $\chi'' = 0$ well above T_c as well as well below T_c.

When the induced voltages in the secondary is sensed at the input of the dual phase lock-in amplifier, it gives out a signal in the form of dc voltages ϵ_r and ϵ_i proportional to the real and imaginary parts of M that are in in-phase and out-of phase, respectively, with respect to the reference signal which is in-phase with the applied field *H*.

From the measured ϵ_r and ϵ_i, the real and imaginary components of the ac susceptibility χ' and χ'' are determined using the formulae shown in Eq. 2.18 to Eq. 2.19.

$$\chi_r \;=\; \frac{\epsilon_r}{\alpha\omega A N \mu_o H_m (1-D)} \;\dots\dots \textbf{(2.16)}$$

$$\chi_i \;=\; \frac{\epsilon_i}{\alpha\omega A N \mu_o H_m (1-D)} \;\dots\dots \textbf{(2.17)}$$

Here N is the number of turns in the secondary across the sample, H_m is the amplitude of the applied ac field, A is the area of the cross-section of the sample, D is the demagnetization factor and α is the filling factor . The absolute values of the ac susceptibility for non-zero demagnetization D values are calculated using the expressions given by Murphy et al. .

$$\chi' \;=\; \frac{\chi_r - D(\chi_r^2 + \chi_i^2)}{(1-\chi_r D)^2 + D^2 \chi_i^2} \;\dots\dots \textbf{(2.18)}$$

$$\chi'' \;=\; \frac{\chi_i}{(1-\chi_r D)^2 + D^2 \chi_i^2} \;\dots\dots \textbf{(2.19)}$$

Following this procedure, the temperature variations of χ' and χ'' are obtained from the measured temperature dependence of ϵ_r and ϵ_i.

2.7.2. M-H hysteresis loops and critical current density measurements
2.7.2.1. Bean's model

The critical current density 'J_c' in type-II superconductors can be estimated by analyzing the magnetization using critical state model proposed by Bean . The model assumes that the penetrated super-currents flow with a density equal to the J_c independent of the local internal field and the flux vortex array is stable and there is no flux creep and the lower critical field is zero. If this magnitude of the current flows everywhere in the specimen, it is in the critical state.

The process of magnetization of a slab of thickness $2a$ in a field parallel to its surface is shown in Fig. 2.17, when the current density is independent of the external field.
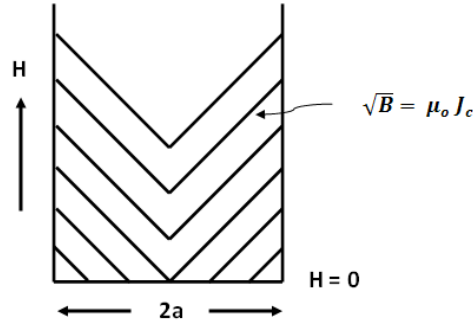
Fig. 2.17. Magnetization process of thin slab of thickness 2a in a field parallel to the surface.

The field within the specimen decreases linearly with the distance, if the material is in the critical state. The Maxwell's equation is

$$\sqrt{B} = \mu_o J_c \text{ .... (2.20)}$$

where J_c is the critical current density in Am^{-2}, B is the magnetic induction in Tesla and μ_o is the absolute permeability.

The local internal field H_i is given as

$$H_i = \frac{B}{\mu_o} \text{ .... (2.21)}$$

where B is the macroscopic local flux density.

The local magnetization M_i becomes $M_i = H_i - H$, where H is the applied field. Therefore the total magnetization M is the average of M_i, over the sample cross-section.

If we consider the magnetization for two stages namely

(i) $0 < H < H^*$ and   (ii) $H^* < H$

where H^* is the applied magnetic field at which the internal field reaches the centre of the specimen.

For an infinite slab, the initial magnetization curve $M(H)$ becomes

$$M(H) = -H + \frac{H^2}{2J_c\,a}, \text{ for } 0 < H < H^* \qquad .... \textbf{(2.22)}$$

$$M(H) = -\frac{J_c\,a}{2}, \text{ for } H^* < H \qquad .... \textbf{(2.23)}$$

The reverse curve for the high $-H_m$ $(H^* < H_m)$ case is given by

$$M(H) = -\frac{J_c\,a}{2} + H_m - H - \frac{(H_m - H)^2}{4J_c\,a}, \text{ for } H_m - 2H^* < H < H_m \text{ .. } \textbf{(2.24)}$$

$$M(H) = \frac{J_c a}{2}, \text{ for } -H_m - H < H_m - 2H^* \qquad .... \textbf{(2.25)}$$

where H is the applied magnetic field, H_m is the maximum applied field and *2a* is the thickness of the slab.

When $H_m > 2H^*$, J_c is related to the magnetization M for slab of thickness 2a as

$$M(H^+) - M(H^-) = J_c\,a \qquad .... \textbf{(2.26)}$$

Therefore J_c can be determined by measuring the width of an M-H hysteresis loop at a given field.

The discussion made above is applicable only if the sample is considered as an infinite slab. The formulation for samples with orthorhombic geometry is given in section 6 of Appendix.

For the orthorhombic geometry

$$M(H)^+ - M(H)^- = J_c b \left(1 - \frac{b}{3a}\right) .... \textbf{(2.27)}$$

2.7.2.2. Calculation of J_c from M-H loops

Magnetization hysteresis loops representing magnetization (M) as a function of applied magnetic field (H) were recorded on the samples at

various cryogenic temperatures using a Physical Property Measurement System (PPMS) of Quantum design make.
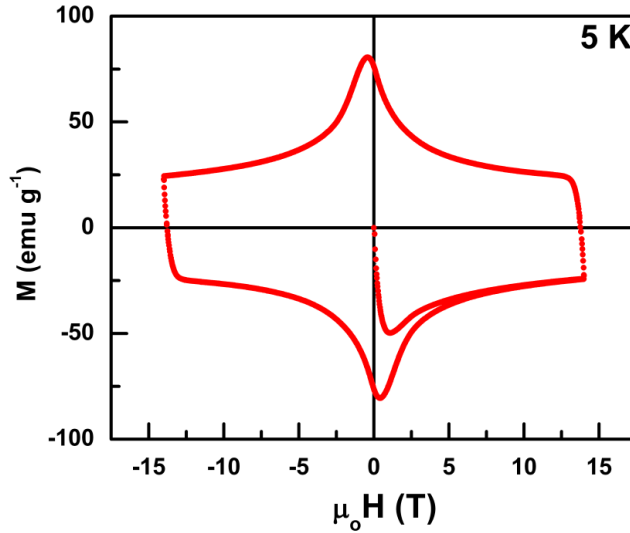
Fig.2.18. A typical magnetic hysteresis (M-H) loop obtained from a IG processed YBCO superconductor at 5 K.

The specimens used for the measurements were of size approximately 2 mm x 2 mm x 5 mm, which were cut such that their long dimension was normal to the pressed surface of the samples. The samples were exposed to magnetic fields of up to 9 Tesla generated by superconducting magnet in order to record the field dependences of magnetization. A typical M-H loop obtained for a superconductor is shown in Fig. 2.18.

Critical current densities (J_c) of the samples were determined following extended Bean's critical State model using the relation [22-23]:

$$J_c = \frac{20\,\Delta M}{d} \,.......... \textbf{(2. 28)}$$

where $\Delta M = M^+ - M^-$ (in emu/cc), $d = b\left(1 - \dfrac{b}{3a}\right)$; $a > b$ and a, b are broad and narrow dimensions of the sample (in cm).

References

[1]   A. Manthiram and J. B. Good enough, *Nature* **329** (1987) 908

[2]   D. Bahadur, A. Banerjee, A. Das, K. P. Gupta, T. Mathews. A. Mitra, M. Tewari and A. K. Majumdar, *Rev. Solid State Science* **2** (1988) 77

[3]   S. H. Shieh and W. J. Thomson, *Physica C* **204** (1992) 135

[4]   G. Kordas, K. Wu, U. S. Brahme, T. A. Friedmann and D. M. Ginsberg, *Mater. Lett.* **5** (1987) 417

[5]   W. W. Schmahi, A. Putnis, E. Salja, P. Freeman, A. Graeme-Barber, R. jones, K. K. Singh, J . Blunt, P. P. Edwards, J. Loram and K. Mirza, *Phylosophical Magazine letters,***60(6)**,(1989) 241-248

[6]   W. L. Bragg, *The Diffraction of Short Electromagnetic Waves by a Crystal*, *Proc. Cambridge Phil. Soc.*, **17 (**1913) 43-57

[7]   N. Devendra Kumar, T. Rajasekharan, K. Muralidharan, A. Benerjee and V. Seshubai, *Supercond. Sci. Technol.* **23** (2010) 105020

[8]   K,. Iida, N. Hari Babu, Y. Shi and D. A. Cardwell, *Supercond. Sci. Technol.* **18** (2005) 1421

[9]   Joseph Goldstein, D. E. Newbury, D. C. Joy, C. E. Lyman, P. Echlin, E. LIfshin, L. Sawyer, and J. R. Michael. *Scanning Electron Microscopy and X-ray Microanalysis* (3 ed). Springer, 2003

[10]   O. O. Omatete, M. A. Janney, and R. A. Strehlow, *Am. Ceram. Soc. Bull*., **70** [10] (1991).1641-49

[11]   Mark A. Janney, Ogbemi O. Omatete, Claudia A. Walls, Stephen D. Nunn, Randy J. Ogle, and Gary Westmoreland, *J. Am. Ceram. Soc.*, **81 [3]** (1998)581–91

[12]   R. GilissenU, J.P. Erauw1, A. Smolders, E. Vanswijgenhoven and J. Luyten, *Materials and Design* **21** (2000) 251-257

[13]   Stephen Brunauer, P. H. Emmett and Edward Teller, *J. Am. Chem. Soc.* **60** (1938) 309-319

[14]   J. Lyklema, "*Fundamentals of Interface and Colloid Science*" **vol. 2**, 1995

[15]   Hideki Okamoto, Minoru Hashiba, Yulkio Nurishi and K. Hiramatsu, *J. Mater. Sc.* **26** (1991) 383-387

[16]   J. C. Harper, Coaxial cylinder viscometer for non-Newtonian fluids, *Rev. Sci. Instrum.* **32** (1961) 425-428

[17]   R. Bottom, Thermogravimetric *Analysis, in Principles and Applications of Thermal Analysis* (ed P. Gabbott), Blackwell Publishing Ltd, Oxford, UK. (2008) doi: 10.1002/9780470697702.ch3

[18]   W. R. Runyan, *Semiconductor Measurements and Instrumentation* (New York: McGraw-Hill) (1915) pp 65-85

[19]   M. Couach and A. F. Khoder, *Magnetic Susceptibility of Superconductors and other Spin Systems* edited by Hein R A, Francavilla T L and Liebenberg D H 1992 (Plenum, Newyork)

[20]   S. D. Murphy, K. Renouard, R. Crittenden and S. M. Bhagat, *Solid State Commun.* **69** (1989) 367

[21]   C. P. Bean, *Phys. Rev. Lett.* **8** (1962) 250

[22]   D. X. Chen and R. B. Goldfarb, *J. Appl. Phys.* **66** (1989)2489

[23]   M. Murakami, M. Morita, K. Doi and K. Miyamoto, *Jpn. J. Appl. Phys.* **28** (1989) 1189

Fabrication and Microstructural studies on YBCO Nanocomposites

3.1. Introduction

The microstructures of melt or IG processed YBCO superconductors play an important role in deciding their current carrying capacity and hence their suitability for practical applications. Introduction of Y-211 particles in the Y-123 matrix is known to improve current densities at high applied magnetic fields due to pinning of magnetic flux at fine structural defects generated at the Y-123/Y-211 interface due to lattice mismatch [1]. The defect density per unit volume of the YBCO superconductor is affected by the size and morphology of Y-211 particles; Y-211 particles, if they are fine and spherical, increase the Y-123/Y-211 interface area and will also help maintain the superconducting Y-123 matrix continuous [2]. The coherence lengths in the Y-123 superconductors are 2-3 nm [3], and hence, finer nanometer-sized defects at the 123/211 interfaces are believed to be very effective in promoting flux pinning. The possibility of enhancing the current densities supported by melt processed samples by the external addition of fine second phase particles have also been investigated. Many investigators have introduced nanoparticles of materials such as Y_2O_3 [4], ZrO_2 [5] , $BaCeO_3$ [6], Al_2O_3 [7] and NiO [8], as fine second phase particles in the melt grown YBCO. As described in Chapter I, the presence of liquid phases during melt processing causes 'pushing effects' [9] leading to movement and

agglomeration of Y-211 particles in the melt, resulting in inhomogeneity in microstructure and in the properties of the end product. During melt processing, the 211 particles in the melt are free to move, and second phase particles of nanometer size, if introduced to enhance flux pinning, are also likely to move around and agglomerate [10, 11]. Also, Y-211 particles tend to grow in liquid phase above T_p due to Ostwald ripening [12], and average size of the Y-211 in melt processed YBCO is of the order of 10μm.

In the earlier days, it was noticed that small amounts of Pt picked up from crucibles used for melting could lead to substantial improvement in current densities by refining the size of the 211 precipitates. In the Platinum Doped Melt Growth (PDMG) [13] process, small additions of Pt (less than 0.5% by weight comparable to the Pt contamination levels obtained during the high-temperature melting stage of MPMG [14]) are made to the desired stoichiometry prior to melt processing [15]. The Y-211 size in the resulting microstructure is substantially reduced, and J_c values as high as 2.5 x 10^4 A/cm^2 at 1 T (H ∥ c) have been reported [16]. Addition of Ce, Pt, CeO_2 and PtO_2 has been widely investigated [17-21] during the melt growth process because of the ability of such additives to refine the size of Y-211 particles. Nanometer-sized additives can also directly serve as flux pinning centers due to their small size. An examination of the literature shows that the melt grown samples which show the highest reported current densities are those in which a large amount of nanometer-sized, non interacting materials have been externally added, for instance, melt processed $(Nd_{0.33}Eu_{0.33}Gd_{0.33})$-$Ba_2Cu_3O_{7-\delta}$ (NEG-123) with 35 mol. % of nanometer-sized (70 nm) Gd-211 and 0.1 mol. % of nanometer-sized NbO_3 showed current density of 600 kA/cm^2 at zero field and a current density of 200 kA/cm^2 at 4 T [22].

There are three questions that might be asked in the above context: **(i)** It is known that the IG process causes substantial reduction in Y-211 particle size without the addition of any dopant like Pt oxide or ceria. Essentially, when starting with preforms fabricated out of very fine Y-211 particles (say of 1 micron particle size), the particles are rounded by reaction with the infiltrating liquid phases, and there is no grain growth. The Y-211 size in the final microstructure is thus nearly an order of magnitude less than that obtained in melt processing without dopants. The first question is whether the Y-211 size in IG processed samples would be further reduced by the addition of dopants? **(ii)** Can the experiments on doping be designed in such a way so as to clarify the mechanism of particle size reduction, if any, through doping? This is because conclusions drawn from microstructural observations on melt processed samples can be ambiguous due to the complexity of the high temperature reactions involved. **(iii)** What would be the effect of doping on the critical current densities and their magnetic field dependences in doped samples, and what are the factors that would control such effects?

The reduction in Y-211 precipitate sizes in melt processed Y-123 containing ceria as a dopant was originally attributed to an increase in the number of nucleation sites for the crystallization of the Y-211 formed by the peritectic decomposition of Y-123 [23]. This conclusion was based on the observation of instances of formation of one or more Y_2O_3 cores in some Y-211 particles in the final microstructure, as observed by TEM. Other investigators have suggested that the Pt and CeO_2 in the melt affect the surface energy of Y-211 particles and control their grain growth [24]. Both the proposed mechanisms of Y-211 refinement are based on the observations made on MG processed YBCO composites, where the exact

reaction path is ambiguous as Y-211 and reactive liquid phases are present along with Pt/CeO$_2$ at high temperatures.
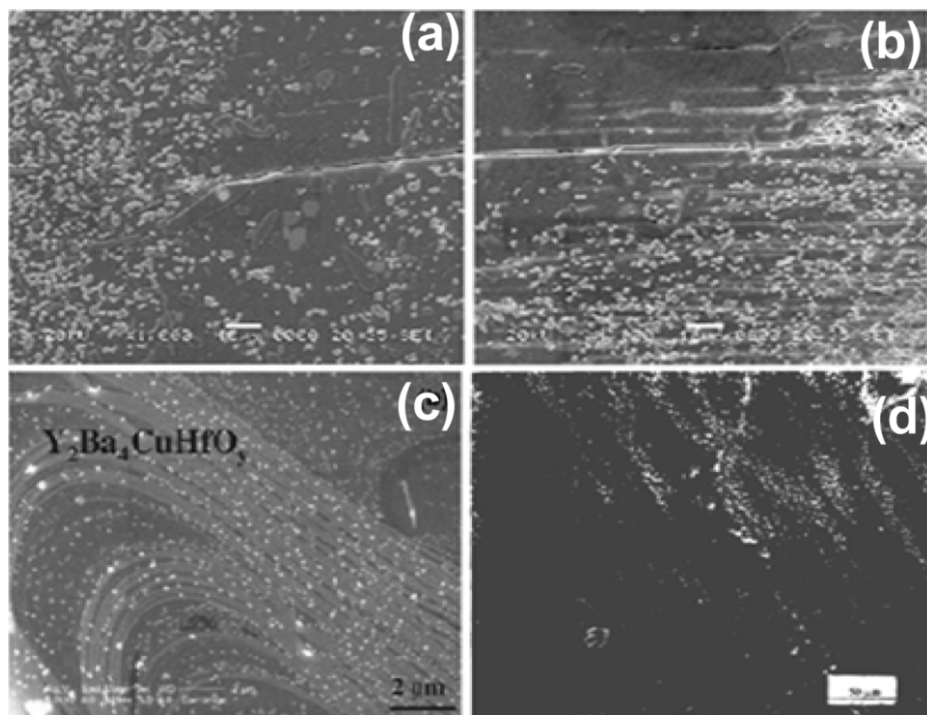
Fig. 3.1. (a) and **(b)** show the segregation of nanoparticles and existence of nanoparticle- free regions in melt grown YBCO composites [6] . **(c)** and **(d)** ([10] and [11] respectively) show the formation of bands of nanoparticles due to flow of liquid phases.

Another difficulty in adding nanoparticles during melt growth is that the movement of Y-211 and other nanoparticles during MG process leads to segregation and agglomeration of the fine particles (Fig. 3.1 (a) and (b) reproduced for convenience from Fig.1.18). Addition of nanoparticles during IG processing has been reported by some workers, but they have introduced them along with liquid phases [25] and not directly into the preforms, and the situation remains similar to that obtained in the MG process where the movement of liquid phases affects the distribution of the fine dopant particles.

In the present thesis a process is developed which enables the introduction of nanoparticles of materials such as CeO_2, ZrO_2 and $BaCeO_3$ into preforms used for IGP as isolated individual particles without agglomeration. The process further proceeds with the infiltration of liquid phases into the preforms and then by a long anneal below the peritectic formation temperature of Y-123 to form the Y-123 phase. Since the nanoparticles are adherent to the Y-211 particles in the preform, it is envisaged that their movement during further processing would be minimized. In the present chapter, we first describe the process developed for distributing nanoparticles, isolated and separate from one another in the Y-211 preform. The microstructural investigations on the nanocomposites prepared as above are then reported. From the microstructural observations, conclusions are then drawn on mechanisms leading to refinement of the Y-211 particles in the presence of the additives

3.2. Introduction of nanoparticles into Y-211 preform

3.2.1. CeO$_2$ nanoparticles

This section discusses the new process that was developed for the introduction of nanoparticles of different materials into preforms used for IGP, as isolated individual particles without agglomeration. We experimented with nanoparticles of CeO_2, ZrO_2 and $BaCeO_3$. The choice of the above materials was made on the observations in the literature that they, as do Pt, refine the Y-211 precipitates in melt processed Y-123 matrix. Considerable amount of literature exists on the doping of the above materials in YBCO [16-20, 25-27], as discussed in Chapter I.

In the present study, Y-211 powder with a nearly uniform particle size distribution around 1-2 μm was prepared through the citrate synthesis

method [28]. The process is described in Chapter II in detail. Y-211 slurry of required concentration was prepared by dispersing the Y-211 powder in water with a dispersing agent identified as described below. Water was chosen as a medium to work with, as it is known not to interact with Y_2BaCuO_5.

Attaining stable and free-flowing slurry involves finding proper dispersing agents and optimizing sedimentation conditions. Sedimentation test of Y-211 slurry was done to find out the best suited dispersant to obtain stable Y-211 slurry.

The Y-211 powder used in the study was first heated up to 300 ^{o}C to eliminate undesirable organic residues from the surface of the Y-211 particles. 5 g of the Y-211 powder was taken in 20 ml of de-ionized (DI) water along with the dispersant. The dispersants we have experimented with were Darvan 821A from R.T. Vanderbilt Company, Inc., Ammonium Polyacrylate (PAA) from National Chemicals, Gujarat, India and Dolapix 77, DOLAPIX PC21, DOLAPIX PC75, DOLAPIX A88, PRODUCT KV 5068, PRODUCT KV 5166 from Zschimmer & Schwarz, Germany. A flow point test [29] was used to decide the approximate amount of dispersant to be used. Nearly 1 wt. % of the dispersant was added in most cases. The Y-211 slurries with dispersants were tumbled in a ball mill for 12 hours to get a uniform coating of dispersant on the Y-211 particle. The sedimentation rates of the slurries thus prepared were studied by monitoring the process in transparent test tubes. It was observed that in many of the suspensions, the particles settled down within an hour and some of them reacted with Y-211 to form a bluish liquid. DOLAPIX 77, DOLAPIX PC21, DOLAPIX PC75 and PAA dispersants which did not react with Y-211 were used for prolonged sedimentation tests. Photographs of the slurries were taken periodically for 24 hours to study the

rate of sedimentation. Dolapix 77 showed the best dispersing ability among all the dispersants we tried. It was found that Y-211 slurry with DOLAPIX 77 was stable for more than 4 hours. The results of the sedimentation tests for a few slurries can be seen in Fig 3.2.
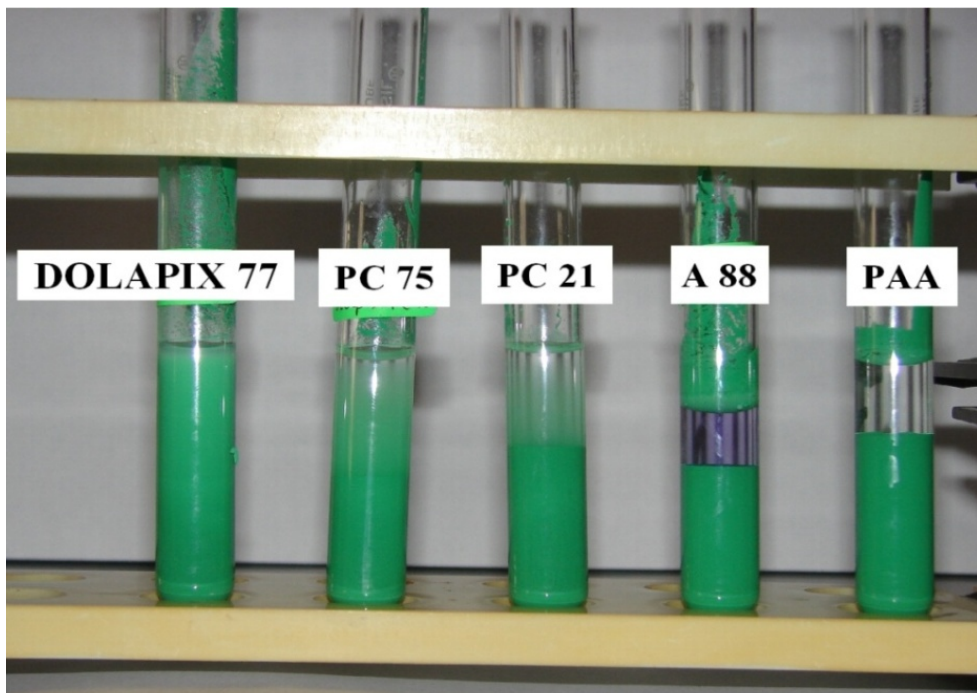
Fig. 3.2. Sedimentation test with 5 wt. % slurry of Y-211 in water, containing 1 wt. % of various dispersants. The suspension was kept for 12 hours to examine the sedimentation rate of the Y-211 particles, for preliminary optimization of dispersants. Y-211 particles remain suspended in the slurry with DOLAPIX 77, whereas with other dispersants the particles have either settled down, or reacted with the dopant as in the sample marked A 88. The good suspension observed with DOLAPIX 77 was sufficient to ensure the completion of the process of nanoparticle introduction without segregation, which required that the slurry is stable for about an hour after mixing.

A sol containing 5 wt. % of ceria nanoparticles was prepared from cerium nitrate $(Ce(NO_3)_3 6H_2O)$, as described by Chen et al. [30]. Cerium nitrate was first dissolved in DI water and was stirred rapidly in a glass beaker using a magnetic stirrer at 60 °C for 90 minutes. Appropriate amount

of NH$_4$OH was added to the solution to form Ce(OH)$_4$. The Ce(OH)$_4$ precipitates were then dehydrated to form CeO$_2$. The formation reaction of ceria from cerium nitrate is as follows:

$$2Ce(NO_3)_3 6H_2O + 7\frac{1}{2}O_2 + 6OH^- \rightarrow 2CeO_2 + 6NO_3^- + 15H_2O$$
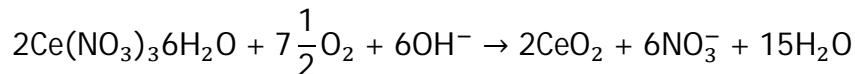
The ceria precipitates thus obtained were washed three times in DI water and then dispersed in DI water. To form a stable colloidal solution, pH of the ceria solution was adjusted to 8 and it was vigorously mixed in an ultrasonicator (OSCAR-PR 250). The sol thus obtained is shown in Fig. 3.3.
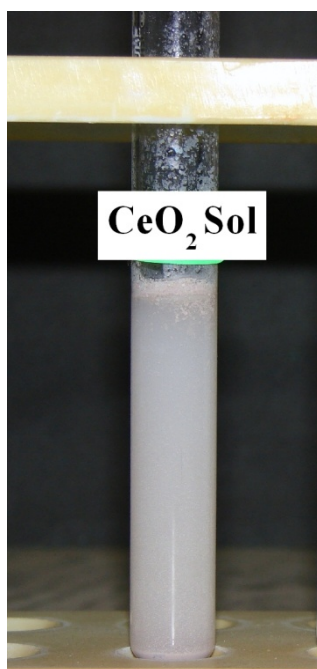
Fig. 3.3. Sol containing 5wt. % of CeO$_2$ nanoparticles.

The nanoparticles in the sol were observed under a Carl Zeiss-made Ultra 55 FESEM and elemental analysis was done using an OXFORD-made Energy dispersive X-ray (EDX) analysis attachment available with the FESEM. A drop of the sol was placed on a carbon tape, dried and coated with gold to

74

avoid charging in the SEM. Very fine networks of ceria nanoparticles are observed under FESEM as shown in Fig. 3.4. The particles were around 20-40 nanometers in size.
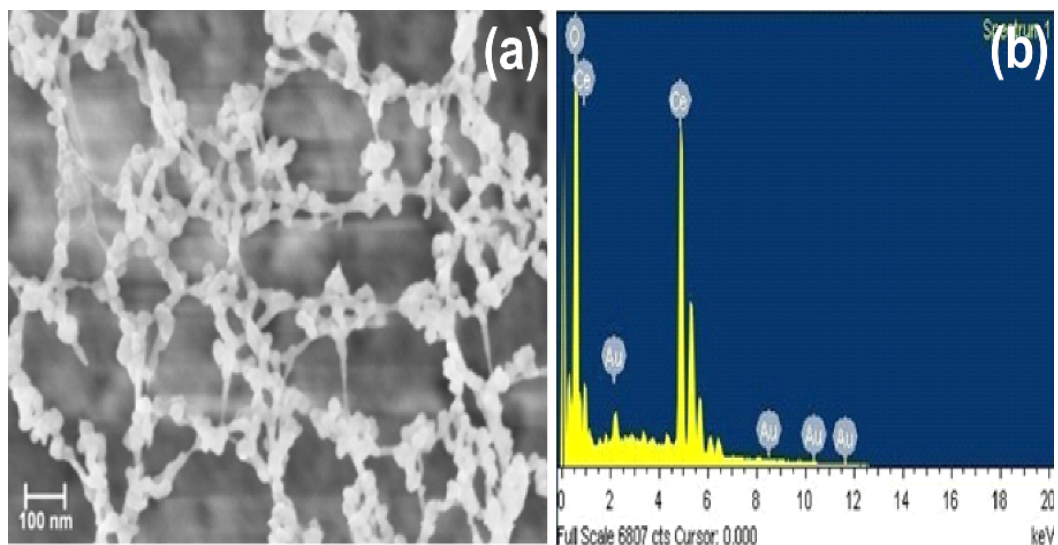
Fig. 3.4. (a) FESEM micrograph recorded from a dried droplet of CeO_2 sol at 100 kX. CeO_2 nanoparticles of 20-40 nm can be seen. **(b)** Elemental analysis on a particle observed in **(a)** shows that it contains Ce and O_2.

Slurries of Y-211 powder were prepared in DI water. About 1 wt. % of Dolapix 77 was used as dispersant. Maximum stability could be obtained in a slurry with 28 vol. % of Y-211. Different samples of the slurry were prepared by adding varying amounts of CeO_2 sol so as to yield slurries with 2 wt. %, 5 wt. % and 10 wt. % of CeO_2, by weight in Y-211. To the above slurries, small amounts of the monomer methacrylamide (MAM) and of the cross-linker methylene bisacrylamide (MBAM) were added. The organics constituted ~5 % of the slurry by weight. The monomer to cross-linker ratio was maintained 6:1 by weight. The slurry was tumbled in a homemade ball mill for 12 h. The slurries were then mixed with small amounts of initiator ammonium peroxydisulphate (APS) and catalyst N, N, N', N',- tetramethylethylenediamine

(TEMED), and cast in a mould and allowed to set. The monomers were completely polymerized within an hour of the casting. Dolapix 77 was suitable for use with the above monomer system because of its ability to disperse Y-211 very well for at least 4 h. The uniform dispersion of particles in the well-mixed slurry, and the quick formation of a polymeric network by setting, prevented segregation of particles.

Y-211 slabs thus obtained containing nano ceria and a small amount of organic matter (~5 wt. %) were dried at room temperature, and then slowly heated to 600 $^\circ$C to expel the organic binder. The slabs were ground and pressed into rectangular pellets of size 16mm x 16mm x 5mm in a stainless steel (SS) die under a uniaxial pressure of 460 MPa. The pellets were then heated at 950 $^\circ$C for 4 hours to form the Y-211 preforms to be used in the Infiltration Growth process (IGP) following a procedure described by Devendra et al. [31]. Fig. 3.5 shows the FESEM micrograph of a Y-211 preform in which 2 wt. % of CeO_2 nanoparticles were doped.

It can be observed from Fig. 3.5 (a) that the Ceria nanoparticles are distributed uniformly on the surface of the Y-211 particles. The Y-211 particles are of the order of 1-2 µm in size. The CeO_2 nanoparticles are around 40-60 nm in size as can be seen from Fig. 3.5 (b). No agglomeration or segregation of the nanoparticles is observed. We will call the process for the dispersion of isolated nanoparticles in Y-211 as Nano-Dispersed Sol-casting (NDSC), for convenience in future reference. The nanoparticles show minimal interaction with Y-211 or also among themselves. The preform is observed to retain enough porosity to allow the infiltration of the liquid phases at a later stage. The above observation highlights the efficiency of the NDSC process in dispersing nanoparticles individually in Y-211 preforms.
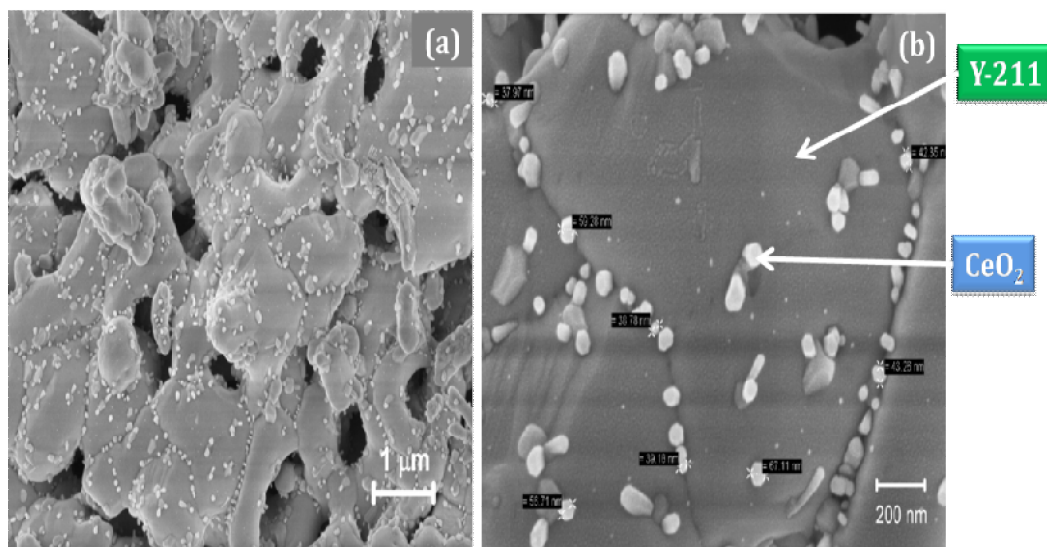
Fig. 3.5. Y-211 preform with CeO_2 nanoparticles, after adding 2 wt. % ceria and heat treating at 950 °C for 4 hours, as seen in an FESEM. **(a)** At a magnification of 10,000 X. Y-211 particles of size around 1-2 μm are observed to be coated almost uniformly with isolated nanoparticles of ceria. **(b)** At a magnification of 50, 000, the ceria particles anchored on the Y-211 particles are observed to be in the size range of 40-60 nanometers.

Among all melt processed or IG processed materials, as discussed earlier, the best current density values have been reported in melt grown NEG-123 system containing 35 mol. % of Gd-211 nanoparticles along with small amounts other nanoparticle additives [22]. Hence it is interesting to study the efficacy of the NDSC process in dispersing large amounts of nanoparticles individually in the Y-211 preforms. 5 and 10 wt. % of CeO_2 nanoparticles were also, therefore, added to the Y-211 preforms through the NDSC process. These preforms were also examined under the FESEM after the heat-treatment at 950 °C for 4 hours. Fig. 3.6 shows FESEM micrographs from Y-211 preforms with 2, 5 and 10 wt. % CeO_2 nanoparticles. In the following discussions, for the sake of convenience, the preform samples containing 2, 5, and 10 wt. % ceria will be referred to as Ce-2, Ce-5 and Ce-10 preforms respectively.

The following observations can be made from Fig. 3.6 We first note that the increase in concentration of CeO_2 nanoparticles in Y-211 preform does not lead to any agglomeration or segregation of the particles, revealing the potential of present NDSC process to avoid agglomeration or segregation while working with large concentrations of nanoparticles. We, however, note that the ceria nanoparticles start interacting among themselves as the concentration increases; we will find that this has significant consequences to the final microstructure of the IG processed superconductor and its critical current density. We also observe that the CeO_2 particles become more and more acicular (or rod-like) as the CeO_2 concentration increases. The length of ceria nano rods in Ce-5 is around 100 nm and in Ce-10; they are as long as 300 nm. In all the samples, the diameter of CeO_2 particles remains 40-60 nm. We also note that there is porosity to allow infiltration of liquid phases into the Y-211 preform in the case of Ce-2 and Ce-10 samples. In the former case, the mild reaction between the Y-211 and CeO_2 has not closed the pores in the preform; in the latter case, the relatively longer nano-rods of CeO_2 keep the Y-211 particles separated, generating increased porosity in the preform. In the case of the Ce-5 sample, the reaction between the dopants and Y-211 has almost completely closed the porosity in the preform.
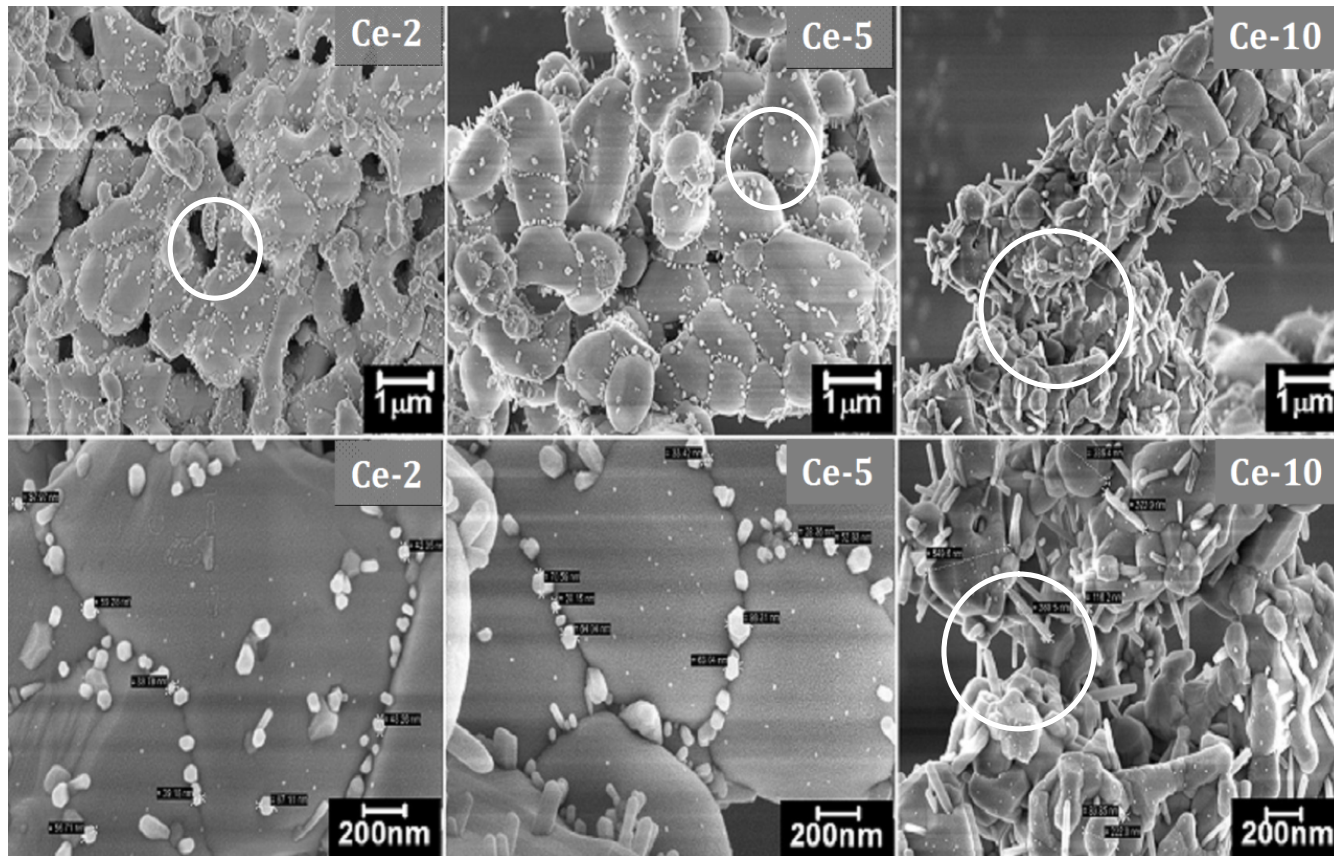
Fig. 3.6. FESEM micrographs recorded on NDSC processed Y-211 preforms with 2, 5 and 10 wt. % of CeO_2, referred as Ce-2, Ce-5 and Ce-10 respectively. The micrographs in the upper row are at a magnification of 10,000 X and those in the lower row are at 50,000 X. Encircled regions show examples of porosity in the preform. The Ce-2 sample shows substantial amount of porosity, whereas the porosity in the Ce-5 sample is much less. The Ce-10 sample again shows considerable amount of porosity, an effect of the acicular growth of the CeO_2 particles.

Fig. 3.7 shows an X-ray diffractogram from the Ce-10 sample. Also shown, in comparison, in the same figure is an X-ray diffractogram from an undoped sample of Y-211. The additional lines, marked by a star in the figure, could be indexed to CeO_{2-x} (JCPDS file no 49-1415).
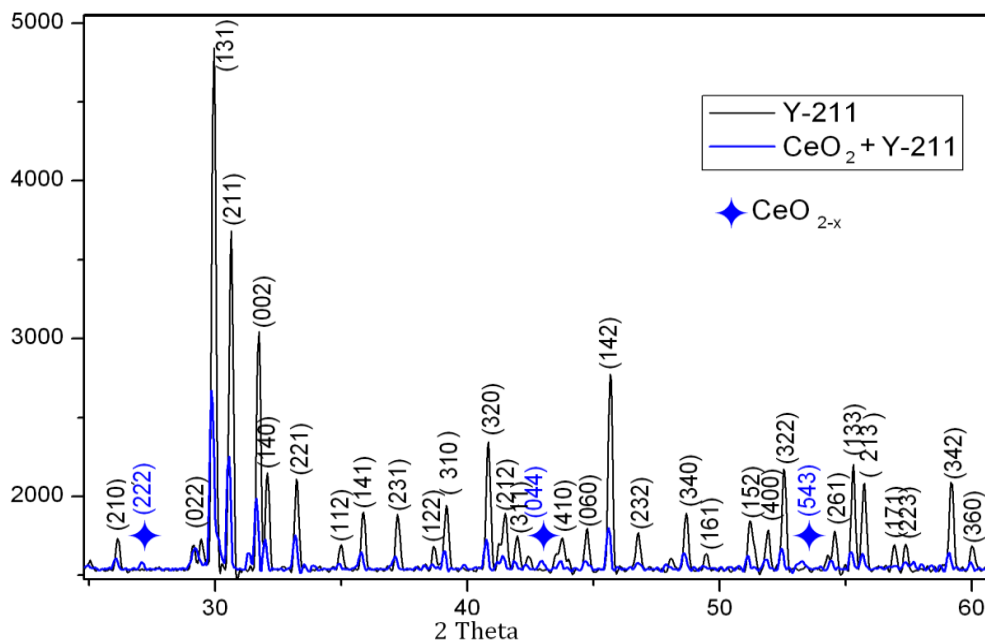
Fig. 3.7. X-ray Diffractogram of Ce-10 is compared with that of Y-211 without any additive. The extra peaks in the former could be identified as due to CeO_{2-x} (JCPDS file no 49-1415).

Vilalta et al. [32] had performed high temperature X-ray diffraction on a mixture of Y-211 and CeO_2, and found that Y-211 reacts with CeO_2 to form $BaCeO_3$ and Y_2O_3 at temperatures above 800 °C. This can be seen from Fig. 3.8 reproduced from their paper. Their results show that a reaction between Y-211 and CeO_2 produces $BaCeO_3$ and Y_2O_3 at high temperatures. Our XRD data suggest that the reaction is very mild at 950 °C, the temperature at which our preforms were fabricated.
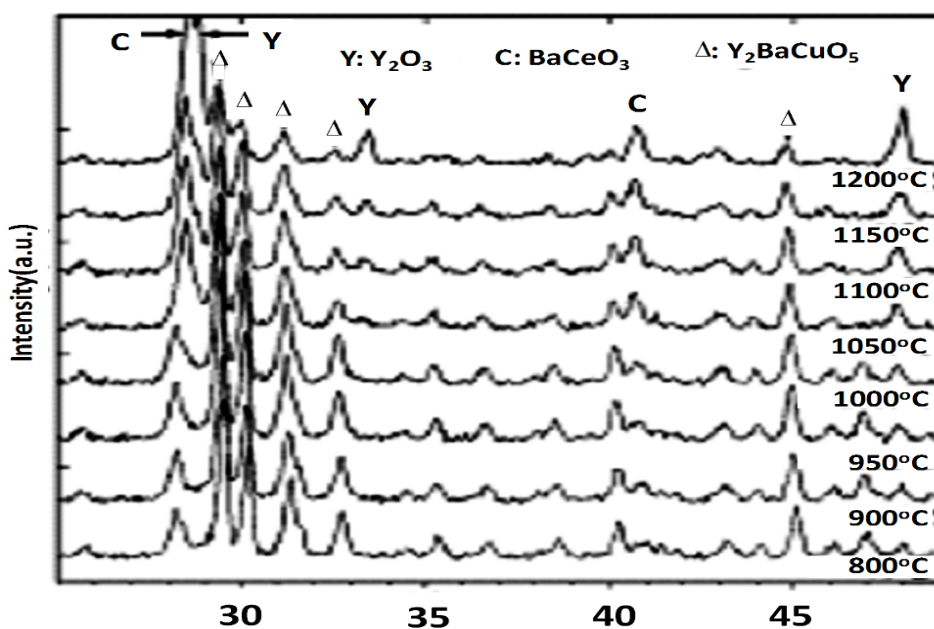
Fig.3.8. High temperature X-ray diffraction patterns from Y-211 containing 20 wt. % CeO_2, from 800 ºC to 1200 ºC. Y_2O_3 peaks are distinctly visible above 1000 ºC [32].

3.2.2. ZrO_2 and Ba-Ce-O nanoparticles

Nanoparticles of ZrO_2 and Ba-Ce-O were produced following essentially the same procedure as discussed in the previous section. The starting material used to produce ZrO_2 nanoparticles was Zirconium oxynitrate. A self-standing sol containing Zirconia nanoparticles were prepared starting with zirconyl oxynitrate ($ZrO(NO_3)_2$. X H_2O). An aqueous solution of the above salt was prepared and excess of ammonium hydroxide was added to it while stirring vigorously to precipitate Ziconium hydroxide. The precipitates were washed in DI water many times, and dried and dispersed in fresh DI water through ultrasonication, thus forming a sol containing ZrO_2 nanoparticles.

Barium carbonate and Cerium nitrate in the molar ratio 1:1 were used to prepare Ba-Ce-O nanoparticles. The above nanoparticles were introduced

into Y-211preforms following the NDSC procedure. Barium carbonate and cerium nitrate were weighed out in the proportion required to give $BaCeO_3$. They were dissolved in water and an intimate mixture of $Ba(OH)_2$ and $Ce(OH)_4$ were obtained by precipitation with excess NH_4OH. The precipitates were washed many times with DI water, dried and dispersed in water by ultrasonication to prepare a sol containing Ba-Ce-O nanoparticles, the exact composition of which could not be assessed.

The sol was then added to a self standing slurry of Y-211 prepared as discussed in Section 3.2. The mixture was tumbled in a ball mill for several hours and Y-211 powder coated with ZrO_2 nanoparticles were prepared as discussed for CeO_2 earlier (section 3.2.1).

A pellet was prepared from the powder under a uniaxial pressure of 460 MPa and sintered at 950 ^oC for 4 hours, to obtain the preform to be used in the IG process. Fig. 3.9 shows the microstructures of the preform observed using an FE-SEM. At the high magnification, Fig. 3.9 (b), individual particles of ZrO_2, well separated from one another, can be seen adhering to the surface of the Y-211 particles. The nanoparticles of Zirconia have reacted more with the Y-211 phase in comparison with ceria nanoparticles in Y-211 preform (Fig. 3.5). They are thus more adherent on the preform surface. Also, it can be observed that the presence of ZrO_2 has promoted the fusing of Y-211 particles into larger grains, from the micron-sized particles in the starting powder.

Figs. 3.9 (a) and (b) show the preforms of Y-211 produced by the NDSC procedure with 2 wt. % and 10 wt. % of ZrO_2 nanoparticles, respectively. We observe that the nanoparticles are isolated from one another and occur without agglomeration adhered on the Y-211 particle surface. The nanoparticles appear to have reacted with Y-211 and have

anchored themselves on Y-211 at the points of contact. We also note a strong tendency for the Y-211 particles to get rounded and fuse together at the temperature at which the preform was fabricated (at 950 $^\circ$C) in the presence of ZrO$_2$. This can affect the availability of continuous porosity to facilitate the infiltration of liquid phases at the later stage.
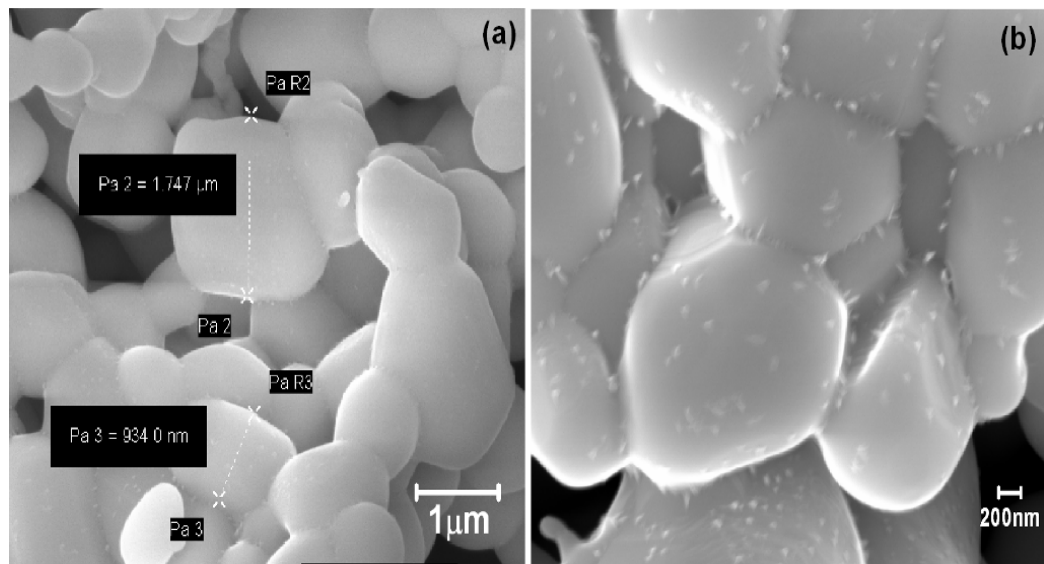
Fig 3.9. **(a)** Micrograph obtained on Y-211 preform with 2 wt. % ZrO$_2$ at a magnification of 20,000 X, shows that Y-211 particles reacted and **(b)** micrograph obtained on Y-211 preform with 10 wt. % ZrO$_2$ at a magnification of 50,000 X, very fine individual nanoparticles of ZrO$_2$ can be seen on Y-211 particles. Both the microstructures confirm strong interaction of ZrO$_2$ with Y-211 and cause fusing of Y-211 particles.

Fig. 3.10 shows the preforms of Y-211 produced by the NDSC procedure with 10 wt. % Ba-Ce-O nanoparticles. We observe that the nanoparticles are isolated from one another and occur without agglomeration, adhered on the Y-211 particle surface. The nanoparticles appear to have reacted with Y-211 and have anchored themselves on Y-211 at the points of contact. We also note a strong tendency for the Y-211 particles to get rounded and fuse together at the temperature at which the

preform was fabricated (at 950 °C) in the presence of Ba-Ce-O. This can affect the availability of continuous porosity to facilitate the infiltration of liquid phases at the later stage, as in ZrO_2 doping.
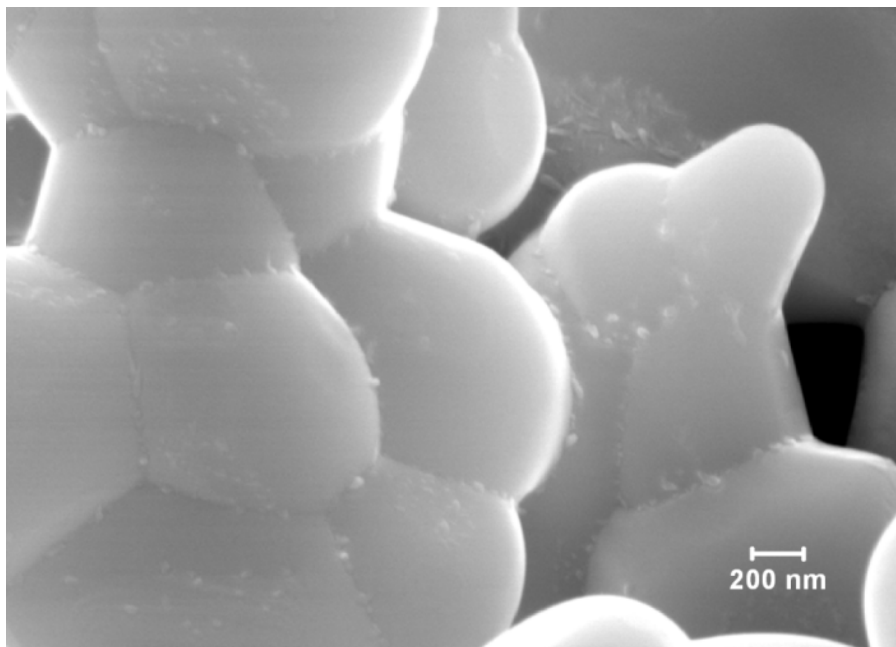
Fig 3.10. FE-SEM image from the Y-211 preform containing 10 wt. % of Ba-Ce-O nanoparticles. The particles are distributed separate from one another. They have reacted with the preform, and the 211particles of the preform have fused together to a large extent.

3.3. Microstructures of YBCO nanocomposites

The preforms containing CeO_2 nanoparticles which were discussed in section 3.2.1., were subjected to IG process. The procedure used in the IG process has been discussed in Section 2.2 in Chapter II. A schematic of the experimental arrangement is shown in Fig. 2.5 (c). The YBCO nanocomposites thus obtained were cut and polished as discussed in Section 2.3, in Chapter II, and observed under the FE-SEM. YBCO products formed from Ce-2, Ce-5 and Ce-10 preforms after IG process are referred to as

nanocomposites/samples of the same code in the remaining part of the thesis.

Microstructures from Ce-2, Ce-5 and Ce-10 nanocomposites are shown in Fig. 3.11. Histograms of Y-211 particle size distribution in the YBCO composites are also shown along with the micrographs. All micrographs are at the same magnification.
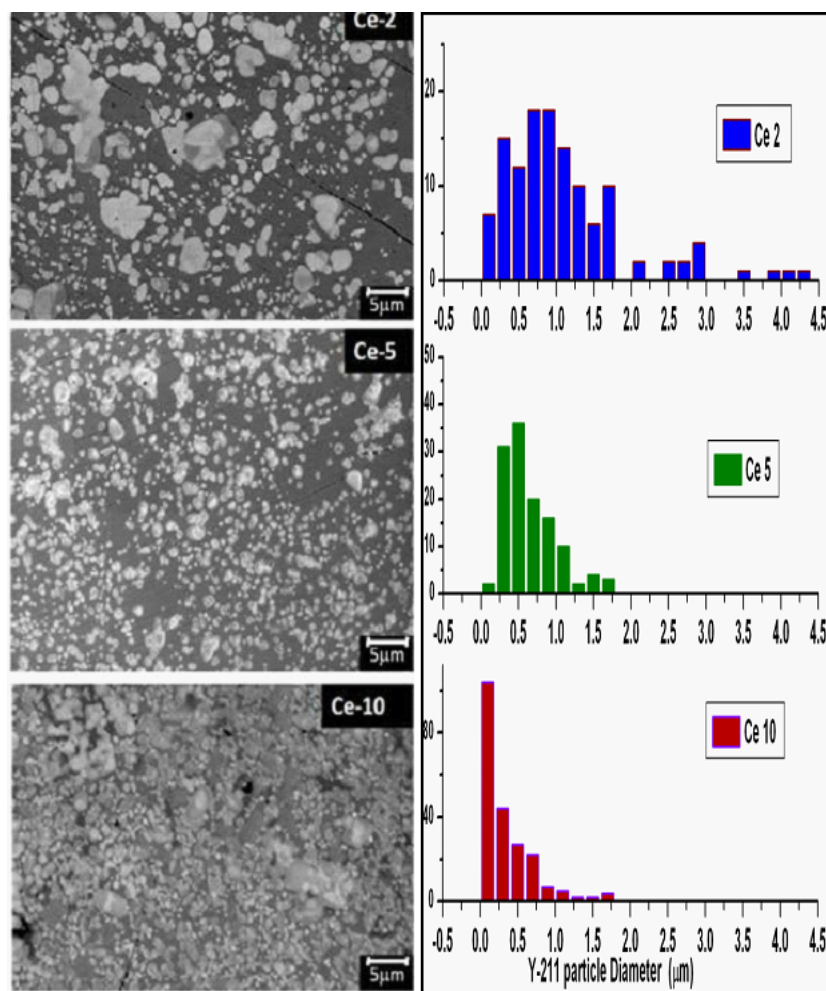
Fig. 3.11. FESEM micrographs obtained on Ce-2, Ce-5 and Ce-10 YBCO composites at 2000 X magnification; on the right side are the corresponding histograms of Y-211 particle size distribution.

85

We observe that the Y-211 size refines progressively when the CeO_2 concentration is increased. In the Ce-2 composite, the Y-211 size distribution is centered on 1 µm, but large grains of Y-211 with size up to 5 µm can be seen. There are also 211-free regions in the microstructure. The Y-211 size distribution becomes narrower in the Ce-5 composite; most of the particles have a size below 1 µm. The majority of the Y-211 particles are sized around 0.5 µm and all the particles are below 2 µm, which is much finer than the average size of Y-211 obtained in the IG process without additives.   There are still some Y-211-free regions, but the distribution of Y-211 particles is more uniform than in Ce-2. The Y-211-size distribution moves to even lower values in the Ce-10 sample, with most of the particles having size below 500 nm; and the distribution becomes still narrower.

Fig. 3.12 compares the FE-SEM micrograph from the Ce-10 sample with that of a POIGP sample with zero CeO_2 content. The latter might be referred to as Ce-0 composite. The respective histograms for Y-211 size distribution are also shown. The Ce-0 sample shows a uniform distribution of spherical Y-211, with the average particle size centered slightly above 1 µm. The observed size of Y-211 in the Ce-0 sample is much lower than that obtained in melt grown samples without any additives. The Ce-10 sample shows a size distribution centered at much lower values in comparison with even the Ce-0 sample, and the distribution is also much narrower. Unlike the Y-211 particles in the Ce-0 sample which shows uniform contrast, the Y-211 particles in the Ce-10 sample appear in different shades of grey.
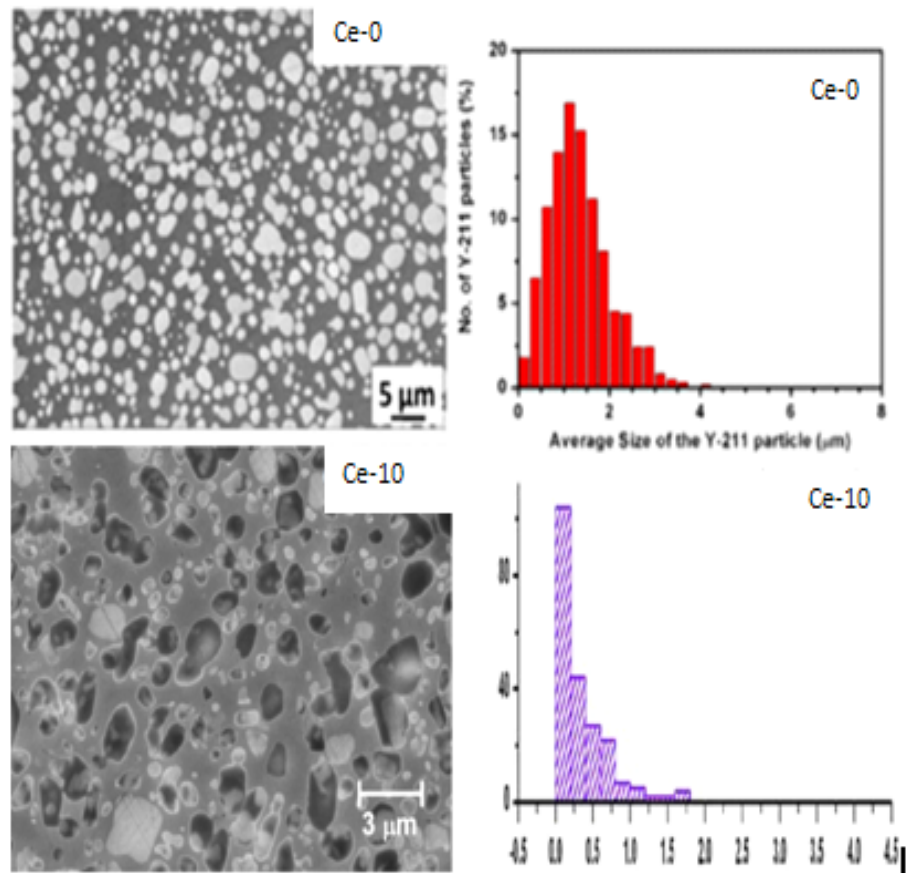
Fig. 3.12. Microstructures of samples with zero and 10 wt. % CeO$_2$, the Ce-0 and Ce-10 samples, both were processed through the POIGP route. The Y-211 size distribution in the Ce-0 sample is centered at slightly more than 1 µm, whereas most of the Y-211 particles in the Ce-10 sample have size below 0.5 µm. The Y-211 grains in the Ce-10 sample occur in different shades of grey suggesting compositional variations between particles and in different regions of the same particle.

3.4. Y-211 refinement with CeO$_2$ addition

As discussed in Chapter I, addition of small amounts of Pt to Y-123 before melt processing could result in substantial refinement of Y-211 particle size in the microstructure of the melt processed Y-123 composite. The J$_c$ supported by the Pt-added samples was also considerably enhanced [19]. The mechanisms leading to refinement of Y-211 particle size in Pt-

added Y-123 has been the subject matter of a large number of studies [13-16, 33-37]. CeO_2 and ZrO_2 added samples have also been reported to cause refinement in the Y-211 particle size in melt processed Y-123. In the previous section, we have shown that CeO_2 addition substantially reduces the particle size of Y-211 in the Infiltration Growth processed Y-123 also, and the reduction in size is considerably more than that obtained by IG processing alone (i. e. in the Ce-0 sample).

Kim et al. [35] have studied the effect of ceria doping in YBCO during melt growth. Microstructure of the resulting sample showed, along with Y-123 and Y-211, the presence of rectangular $BaCeO_3$ precipitates and islands of CuO (Fig. 3.13).
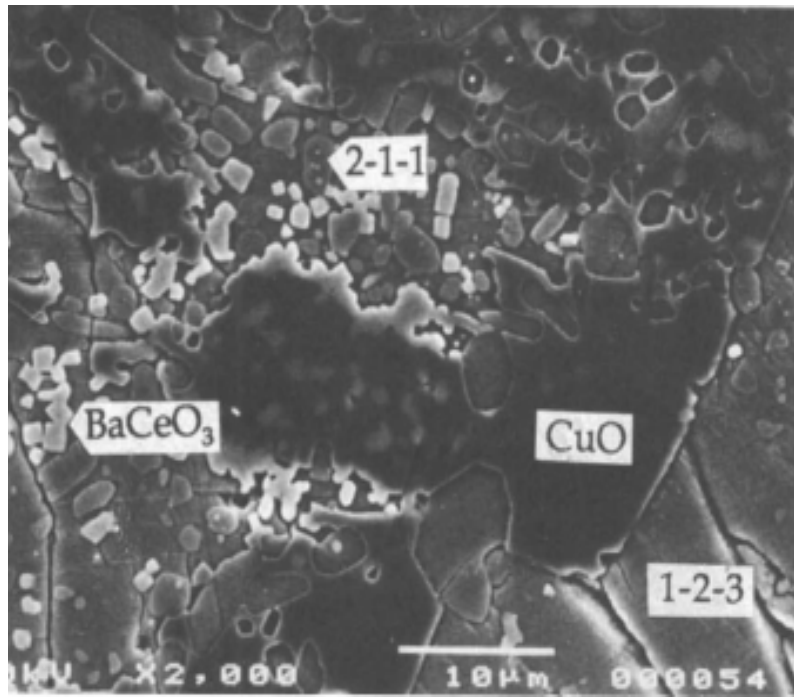
Fig. 3.13. Typical microstructure of Melt processed YBCO with Ceria showing the presence of $BaCeO_3$ particles along with CuO phase, which is a common observation [35].

88

Kim et al. [36] found that when the $Y_{1.2}Ba_{2.1}Cu_{3.1}O_y$ compound is sintered with ceria, it forms a lower T_c phase $Y_{1.2}Ce_xBa_{2.1}Cu_{3.1}O_y$, where 'x' varies from 0 to 0.5 %. In $Y_{1.2}Ce_{0.2}Ba_{2.1}Cu_{3.1}O_y$ and $Y_{1.2}Ce_{0.3}Ba_{2.1}Cu_{3.1}O_y$, twins due to oxygen ordering were observed, but at higher concentrations of ceria, the tetragonal to orthorhombic transition was suppressed. Fig. 3.14 (a) below, reproduced from their paper, shows the change over from the orthorhombic to tetragonal structure as the ceria concentration is increased and also the formation of increasing amounts of $BaCeO_3$. Also, accompanying the increase in ceria content is a lowering of the superconducting transition temperature (Fig. 3.14 (b)).
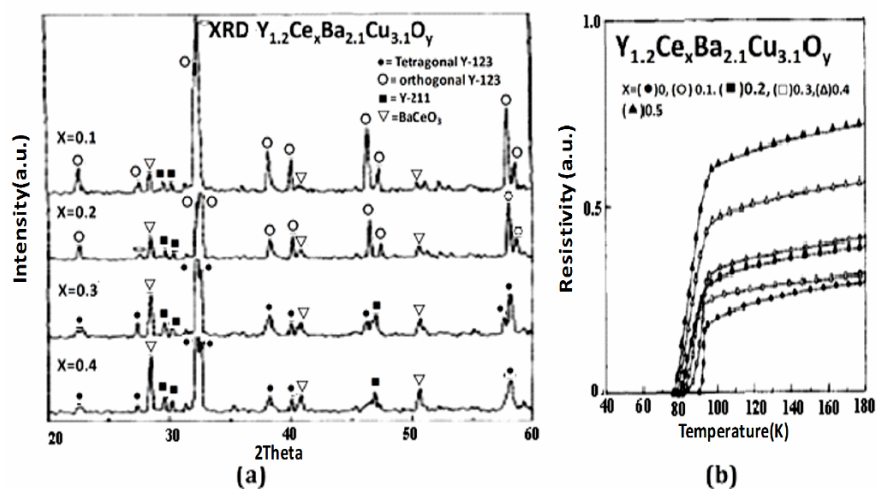
Fig. 3.14. (a) One of the first reports on CeO_2 addition in YBCO (Kim et al. [29]. The YBCO samples sintered with ceria showed the suppression of the formation of the orthorhombic superconducting phase at higher ceria concentrations, and also the formation of $BaCeO_3$. (b) T_c was also lowered as the ceria concentration was increased [36].

Kim et al. [35] studied the grain growth of Y-211, in Y-211 pellets with and without PtO_2 and ceria, when infiltrated with liquids and held at 1100 °C. The grain growth was observed as a function of holding time. No significant

growth in Y-211 particle size was observed with PtO_2 and CeO_2 addition even after 10 hours of holding at 1100 °C (Fig. 3.15), whereas, there was significant grain growth of Y-211 in pure Y-211.
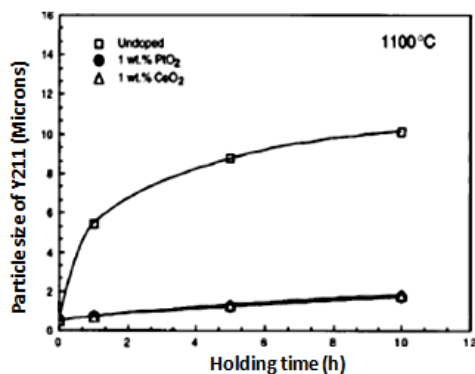
Fig. 3.15. Y-211 particles when held with liquids at 1100 °C increase in size with holding time, whereas the presence of refining agents such as PtO_2 and ceria restricts the growth to a maximum of 1.5 μm in 10 h [35].

Differential thermal analysis of Y-123 with added CeO_2 and $BaCeO_3$, given in Fig. 3.16, showed an increase in the freezing point of the melt with the dopants. This showed that the addition had modified the liquid phase composition and properties.
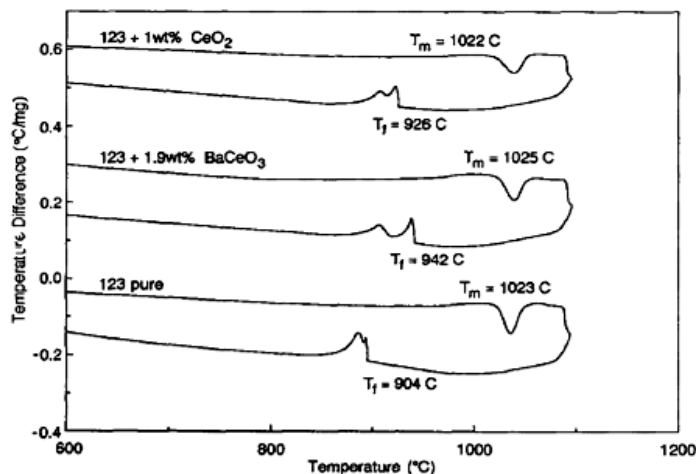
Fig. 3.16. Differential thermal analysis for Y-123, Y-123 + 1 wt. % CeO_2 and Y-123 + 1.9 wt. % $BaCeO_3$. With the additions, the melting point is mostly unaffected but the

freezing temperature is increased. Meignan et al. made use of this observation to conclude that CeO_2 addition modifies the melt characteristics, and thus restricts Y-211 growth [11].

Kim et al. [26] have studied the refinement of Y-211 in melt grown Y-123 containing added ceria. They proposed that the composition of the liquid phase, formed during the melting of Y-123 in the melt growth process, is altered by ceria by using up barium ions for the formation of $BaCeO_3$. This would cause the composition of the system to shift towards right in the phase diagram in Fig. 3.17 (from ref. [34]), explaining the observed formation of CuO. Also, this could result in the formation of non-superconducting $Y_2Cu_2O_5$, and also of other low T_c Cu-rich phases such as Y-124 ($T_c \sim 81$ K) and Y-247 ($T_c \sim 73$ K). Kim et al. [26] attributed the refinement of Y-211 in ceria containing melt grown Y-123, to the formation of $BaCeO_3$ using Ba from the liquid phase, which would alter the liquid phase property and affect the interfacial energy between Y-211 and the liquids; this would hinder the grain growth of Y-211.
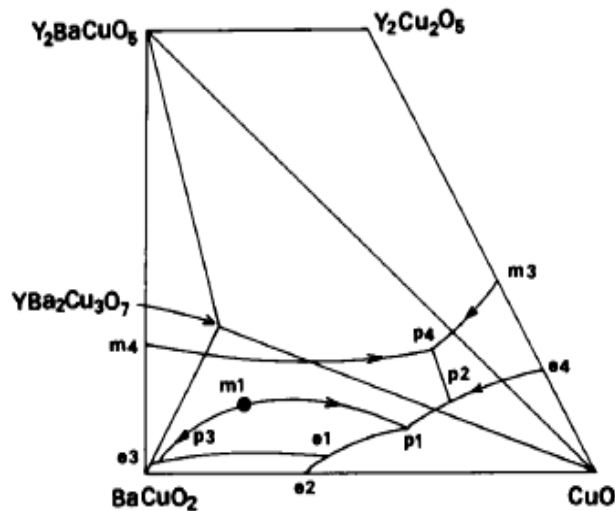
Fig. 3.17. Phase diagram related to the melt reaction of YBCO [34].

Vilalta et al. [32] observed using TEM, in their melt grown samples, some Y-211 particles with Y_2O_3 core/ cores of nanometer size; see Fig. 3.18 (a). This observation caused them to give an alternative explanation for the refinement of Y-211 particles in melt processed Y-123. They proposed that the fine particles of Y_2O_3 form as a result of the removal of barium from Y-211 by ceria according to the following equation,

$$Y_2BaCuO_5 + CeO_2 \rightarrow BaCeO_3 + Y_2O_3 + CuO_z$$

The formation of Y_2O_3 as a result of decomposition of Y-211 containing ceria, was further evidenced by high temperature XRD (Fig. 3.18 (b)).

(a)   **(b)**
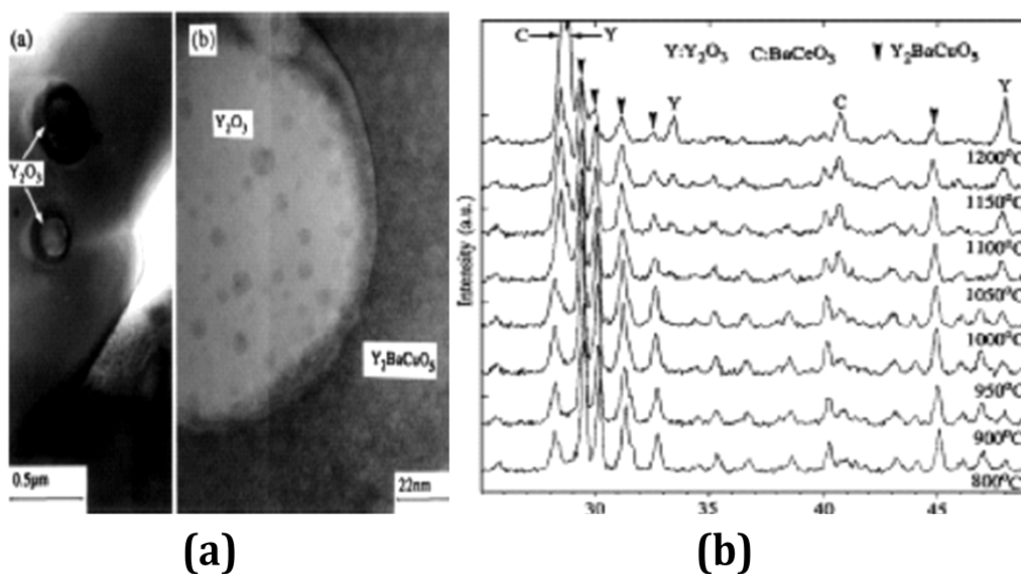
Fig. 3.18. (a) TEM micrograph showing the presence of Y_2O_3 cores within Y-211 particles in melt processed Y-123 with ceria [23]. On the left are two Y_2O_3 particles within a 211 particle and on the right is a magnified image showing one of the particles within the Y-211 background. **(b)** High temperature X-ray diffractograms obtained from Y-211 with CeO_2 [32] shows the formation of Y_2O_3 and $BaCeO_3$. These observations led Vilalta et al. [32] to conclude that the fine Y-211 formed during melt growth of Y-123 are those nucleating on nanometer-sized Y_2O_3 formed during the decomposition of Y-211 in the presence of ceria.

The Y_2O_3 particles thus formed were proposed to serve as nuclei for the crystallization of Y-211 formed by the decomposition of Y-123. But Y_2O_3 cores in Y-211 particles are not a commonly observed feature, and also no free Y_2O_3 has been found in the final melt processed products. The above two mechanisms, which have been advanced to explain Y-211 particle refinement by the addition of ceria during melt processing, have been invoked by other groups [22-23, 31, 32, 34,]. But both mechanisms were derived from observations on ceria addition to YBCO during melt growth. In the MG process, Y-123 is heated above its peritectic reaction temperature to form highly reactive liquid phases and Y-211 at a temperature above 1050 ^{o}C. Hence, it becomes difficult to arrive unambiguously at reaction paths and mechanisms that lead to the refinement of Y-211 in the end product.

3.5. Mechanism of Y-211 size refinement in CeO$_2$ doped YBCO nanocomposites

We had earlier, in Section 3.2, discussed Y-211 preforms containing ceria nanoparticles obtained by the NDSC process developed in this work. Isolated particles of ceria, about 40-60 nm in size, were adherent on the surface of the Y-211 particles in the preform (Fig.3.5). The ceria nanoparticles were separated from one another and at the temperature at which the preform was fabricated; i.e. at 950 ^{o}C, there was only minimal interaction between the Y-211 and ceria. The fact that the Y-211 particles of the preform have isolated nanoparticles on their surfaces before the liquids are infiltrated, allows the process that leads to Y-211 particle refinement during the IG process to be traced clearly from our experiments.

We had displayed in Fig 3.11 the microstructures of IG processed materials with different amounts of Ceria, as recorded in the FE-SEM images

in Fig. 3.11. Images from those samples at a higher magnification are shown Fig.3.19.
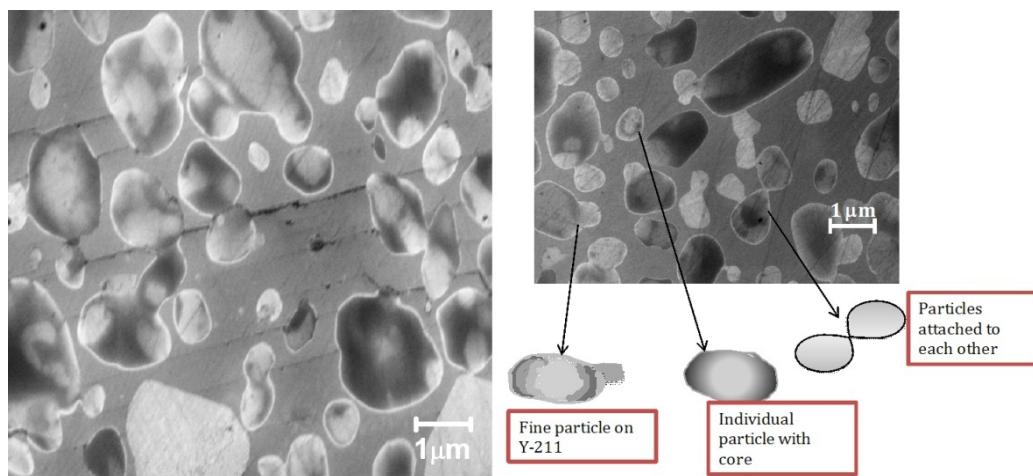
Fig. 3.19. Microstructure of CeO_2-doped YBCO composites. Y-211 particles with varying sizes and contrast are observed. Submicron sized bright particles identified to be $BaCeO_3$ by EDAX are attached to several Y-211 particles. Some $BaCeO_3$ particles are also free. Most of the Y-211 particles are with one or more bright core regions whose compositions were measured by EDAX to be Y- and Cu-rich, containing small amounts of Ba. Several particles of Y-211 appear to be developing necks and proceeding towards division into two or more particles by reaction of the Y-poorer regions with liquid phases.

A strong reaction between ceria and Y-211 material is evidenced in all the micrographs in the above figure. Most of the particles derived from Y-211 have one or more white cores. Such cores are surrounded by darker regions. Often, there are fine white particles in the size range 100-300 nm attached to the bigger particles derived from Y-211. The particles derived from Y-211 are often seen to be developing necks at one or two places as if they are about to split up.

Compositional mapping was performed on the YBCO composites to identify the composition of these regions, shown in Fig 3.20.
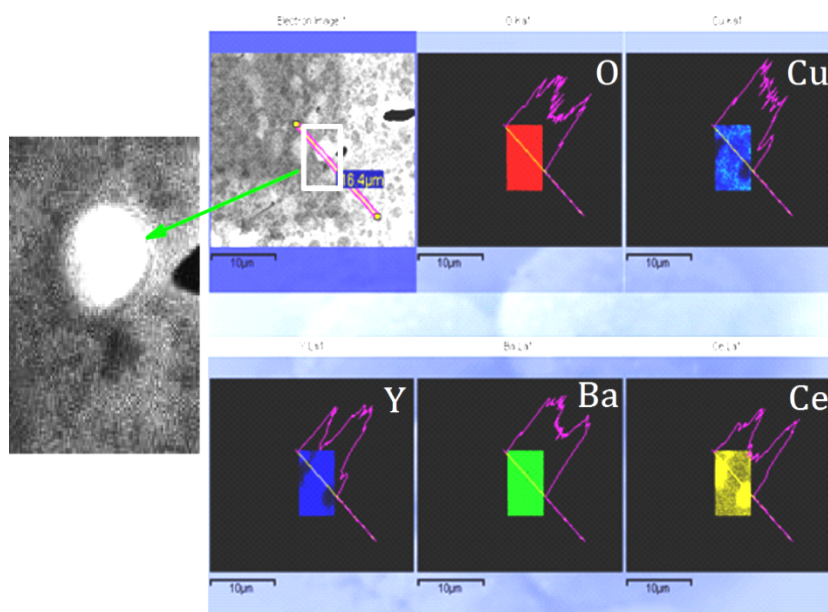
Fig. 3.20. Compositional mapping of Ce-10 on Y-211 particle with central bright core. Ba and O found through the particle as can be seen in red and green spectra. The center is rich in Y-atom as shown in blue colored and some amount of Cu and towards the edges presence of Ce-atom is found with no Cu and Y. The central region in these particles is Ba deficient and at the edges some amount of Ce is dissolved

Compositional analysis across the Y-211 particle having a central bright core was done using an EDAX attachment available with FESEM. Each element is represented by a different color, for example oxygen is represented by red, Yttrium by blue and so on, and the presence of color indicates the presence of the respective element. The pink colored graph on each elemental map represents the concentration of the element along the line, for example in case of Ce two peaks are seen in the graphs corresponding to the Ce-rich regions and central dip indicates absence of Ce at the center which is in agreement with the elemental map for Ce.

The central bright cores, found in Y-211 particles are Y and Cu-rich and deficient in Ce and Ba as seen from elemental maps. Towards the edge of

the particle Ce and Ba- rich regions are found without any Y and Cu. From the above observation following conclusions can be made

  I.   Central brighter regions found in Y-211 are rich in Y

  II. Ce is found at the edges along with Ba, suggesting possibility of the presence of BaCeO$_3$ phase

  III. Cu and Ce atoms are mutually exclusive so no compound with Ce and Cu are formed.

We have studied the compositions of various phases occurring in the micrograph by EDAX, in order to understand the mechanism leading to Y-211 refinement in IG processed ceria containing YBCO. It was observed that the white core regions within the larger precipitates had yttrium, barium, copper and oxygen. The cores were rich in yttrium. The darker regions surrounding the cores were close to Y-211 in composition, but with some cerium. The Y-123 matrix also was found to have some amount of dissolved cerium.

Based on the above observations, we propose the following mechanism for the refinement of Y-211 during IG processing with ceria doping. Please refer to Fig.3.21 below.
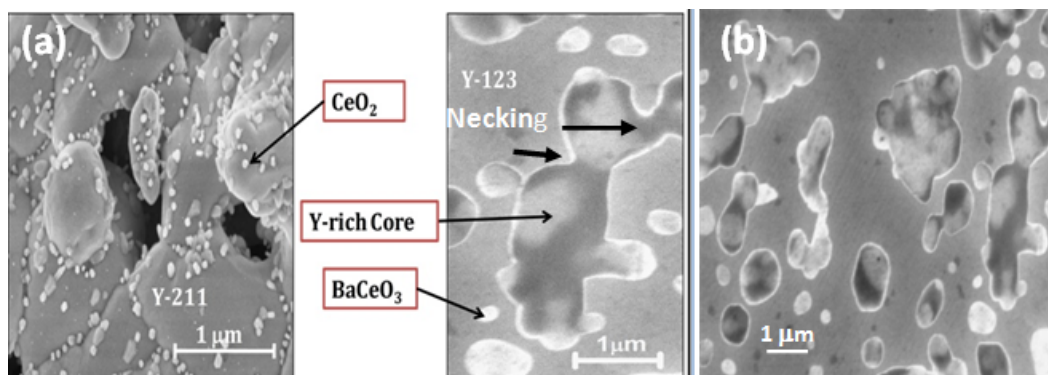
Fig. 3.21. (a) Y-211 particles in preform of Ce-2 with nanoparticles of ceria adhering to its surface. **(b)** A region from the FE-SEM micrograph of the Ce-10 composite showing many rounded Y-211 particles with small particles of BaCeO$_3$ attached. It is proposed that the Y-211 particles lose Ba in regions close to the

attached CeO_2 nanoparticles to form the white Y-rich core regions in the bigger Y-211 particles. Some $BaCeO_3$ particles have also detached themselves from the Y-211 particles after reaction of the supporting Y-211 substrate with the liquid phases. The liquid phases do not react with the Y-rich core region, but rather with the surrounding darker regions of the Y-211 grain, with compositions close to the original. This develops necks on the Y-211 particles which on breaking divide the particles.

In Fig. 3.21 (a) we see nanoparticles of ceria on Y-211 particles in the preform. They have, to some extent, mildly reacted with Y-211 surfaces and are attached to the surfaces. On the introduction of liquid phases into the preform at higher temperatures, the ceria nanoparticles do not get dislodged from the Y-211 surface. They draw barium from the bigger Y-211 grains leaving white yttrium and copper rich region/regions inside each grain. One or more such core regions are formed in a Y-211 particle. This view is supported by the observation in Fig. 3.21 (b). Many fine $BaCeO_3$ particles (as evidenced by EDAX) can be found fused to a Y-211 grain on the outside, most probably originating from the nanometer –sized ceria grains attached initially to the Y-211 preform. The white Y-rich core regions in the Y-211 grains are in close proximity to the $BaCeO_3$ particles. The phases that appear in this reaction are in accordance with what is expected when Y-211 gets depleted in Ba, from the phase diagram in Fig. 3.17. Regions of Y-211 which do not get enriched in yttrium react with the liquid phases to form Y-123 with some amount of dissolved ceria in the process. The original Y-211 particle, now with yttrium richer composition, divides to form more than one particle. The white particles either attached to the Y-211 grains or just detached from them is a compound of barium and cerium, clearly barium cerate. Those particles are quite small, and are in the size range 100-300 nm.

We note that in our observations, there are many points in common with observations of previous workers, cited earlier. The formation of

nanometer-sized yttria as a core in Y-211 was observed, though in isolated cases. However, the core region which in our experiments is of the size 300-500 nm is not Yttria, but rather has Y-rich compositions containing Cu and Ba. Those core regions also do not seem to be the nuclei for the nucleation of additional Y-211 produced at a later stage, as suggested by the earlier workers. In fact, the fact that there is no additional Y-211 produced by the decomposition of Y-123 as in the melt growth experiments makes our results easier to interpret. The main factor resulting in the refinement in size of the Y-211 particles is the division of those particles by the difference in the reactivity of the core region and the remaining part of the particles with the liquid phases. Nanometer-sized yttria cores in Y-211 do not seem to serve as additional nucleation sites for Y-211 in our IGP experiments, and also, changes in the liquid phase composition affecting the surface energies at the Y-211-liquid interfaces do not seem to play a major role in particle size refinement.

3.5.1. Extension of the mechanism to other refining agents such as ZrO_2

ZrO_2 has been studied quite extensively as an additive to YBCO [38], and also used for texturing bulk YBCO [39] and is very much significant in HTS thin film growth. It has been pointed out that $BaZrO_3$ particles form in YBCO when melt processed with ZrO_2. In this section, we report the results on YBCO, IG processed with isolated nanoparticles of Zirconia introduced through the NDSC process; we then compare them with those reported in the earlier sections on ceria added YBCO.

The preform of YBCO containing ZrO_2 nanoparticles as obtained above was used in the IG process. Fig. 3.22 shows the microstructure of the IG processed material containing 2 wt. % ZrO_2 nanoparticles.
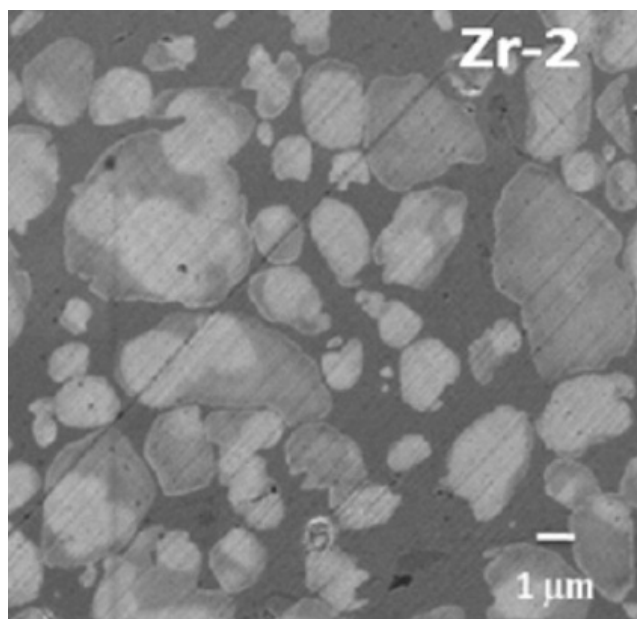
Fig. 3.22. Formation of white Y-rich core is observed in the Y-211 particles in IG processed YBCO with added ZrO_2. The formation of the core can be attributed to the depletion of barium from regions of Y-211 particles due to its reactivity with Zirconia. However, the reduction in size of the Y-211 particles is not much as the Y-211 particles get fused at the preform fabrication stage in the presence of ZrO_2 nanoparticles, as can be seen from Fig. 3.20.

Y-211 particles appear in different shades of grey, as in the ceria-containing samples. The Y-211 particles have a white core region rich in yttrium. This suggests a particle size refining mechanism similar to the one seen in the case of the ceria-doped samples. Though some Y-211 particles of size around 1 μm can be seen, the particle size of Y-211, in general, is much larger than that obtained in the POIGP samples without additives (Ce-0 in Fig. 3.12). The absence of size refinement of the Y-211 particles is probably related to the fusing of Y-211 into large grains, in the presence of ZrO_2 at the preform formation stage, see Fig.3.10. In comparison with the Y-211 grains in the preform, the refinement has been substantial. The grain growth of Y-211 in Pt containing YBCO was studied by Imagawa et al. [40] using four different sample fabrication techniques. They observed that in the two cases where

the Y-211 grew to relatively large sizes in the initial stages, refinement through the introduction of PtO_2 was not significant. An experiment with 2 wt. % ZrO_2 nanoparticles generated large grain growth of Y-211 in the IG processed material (see Fig. 3.23, reproduced for convenience from Fig. 3.9), fusing the Y-211 grains at the preform fabrication stage.
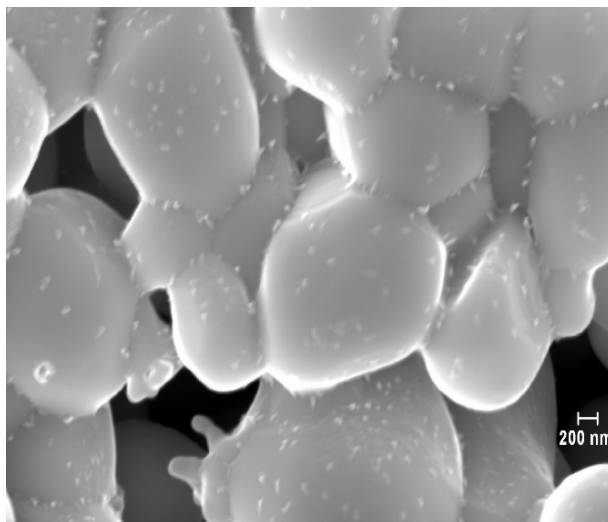
Fig. 3.23. ZrO_2 nanoparticles are seen individually deposited on the Y-211 grains in a preform of Y-211 heat-treated for 4 h at 950 °C. The nanoparticles appear to have reacted to a certain extent with the Y-211 grains. They are, therefore firmly adherent on the Y-211 surface and are unlikely to be dislodged during the infiltration of liquid phases. We also observe that the Y-211 particles have fused into large grains.

When the content of ZrO_2 nanoparticles was increased to 10 wt. %, grain growth of Y-211 was still considerable (Fig. 3.24), but less than that in the sample with 5 wt. % ZrO_2. The observation that the Y-211 grain growth peaks in the middle at ~5 wt. % was common to both ceria and zirconia containing samples, and we have verified that it is indeed so by repeating the experiments.

The final grain size of Y-211 can be considered to be a result of two competing processes: **(i)** The grain growth of Y-211 by reaction with the dopant at lower temperatures and **(ii)** the availability of the dopant to divide the grains during the IG process. Fig.3.24 also shows excess, unreacted ZrO_2 nanoparticles (size ~20 nm) segregated and pushed to the 211-free regions in the microstructure.
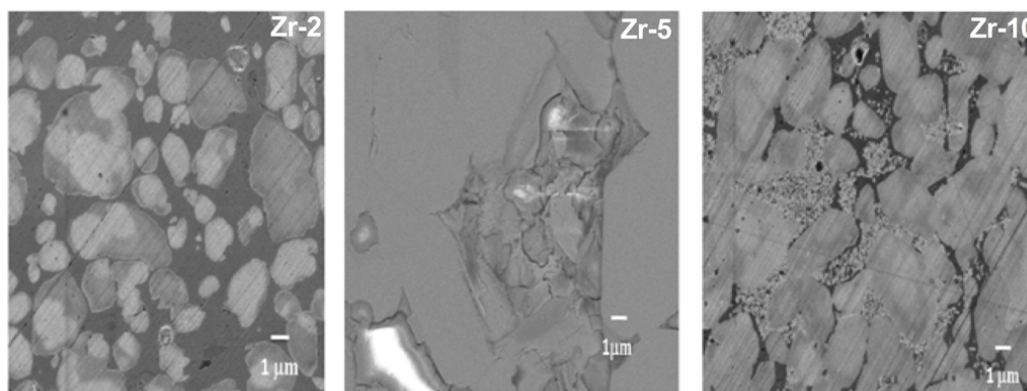
Fig. 3.24. The microstructure (as obtained by FE-SEM) of IG process YBCO containing 2, 5, and 10 wt. % ZrO_2 nanoparticles introduced by the NDSC procedure., referred to as Zr-2, Zr-5 and Zr-10 respectively. As low concentrations of ZrO_2, the grains of Y-211 which had grown considerably at the preform fabrication stage have been substantially refined, though the particle size is still more than 1 μm. The Y-211 grain growth could not be offset in the other two samples, and the IG processed samples have very large Y-211 grains. In the 10 wt. % sample, the Y-211 size has lowered in comparison with the 5 wt. % sample due to the refinement due to large amount of ZrO_2 available. The unreacted excess of ZrO_2 nanoparticles of size around 30 nm are found to be segregated in the micrograph.

3.5.2. Effect of $BaCeO_3$ on Y-211 refinement

Different amounts of the sol containing Ba-Ce-O nanoparticles namely 0.1 wt. %, 0.5 wt. %, 3 wt. % and 10 wt. % (with respect to the weight of Y-211) were added in the Y-211 preforms. The FE-SEM microstructure of a preform containing 10 wt. % of Ba-Ce-O nanoparticles is shown in Fig. 3.25 (Reproduced again for convenience from Fig. 3.10.)

We see that the nanoparticles are distributed individually and that they have reacted very strongly with the Y-211 particles in the preform. The Y-211 particles have fused into large grains.
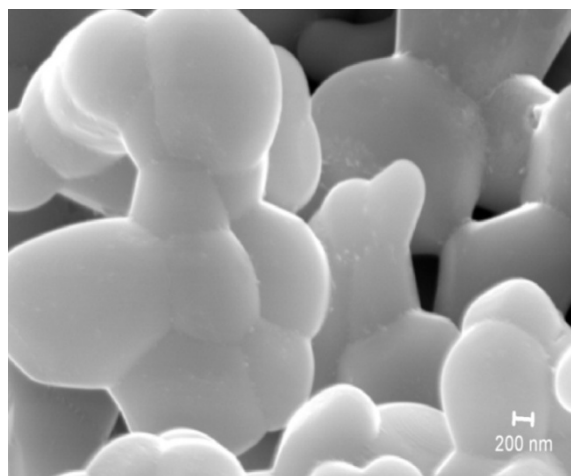
Fig. 3.25. FE-SEM image from the Y-211 preform containing 10 wt. % of Ba-Ce-O nanoparticles. The particles are distributed separate from one another. They have reacted with the preform, and the Y-211 particles of the preform have fused together to a large extent.

FE-SEM microstructures of Y-123, IG processed starting with preforms containing 0.1 wt. %, 0.5 wt. %, 3 wt. % and 10 wt. % of Ba-Ce-O nanoparticles are referred to respectively as BaCeO-x (x = 0.1, 0.5, 3, 10) and are shown in Figs. 3.26 (a), (b), (c) and (d). We observe from Fig. 3.26 (a) that with 0.1 wt. % of Ba-Ce-O added, there is considerable Y-211 grain growth which can be attributed to the fusing of Y-211 particles in the preform. Signs of vigorous reaction between Ba-Ce-O and Y-211 in the final microstructure is missing, unlike in the micrographs of IG processed samples with ceria and Zirconia doping. This might have to do with the fact that the Ba-Ce-O nanoparticles have sufficient Ba to form $BaCeO_3$ and do not draw much Ba from the Y-211 grains. There is no formation of white Y-rich core within the Y-211 grains for the same reason. The effect of the particle

division mechanism in the sample with 0.1 wt. % of Ba-Ce_O has been to bring about a certain amount of size reduction for the Y-211 particles in comparison with the particle size in the preform, but not enough to bring down to the levels observed in ceria containing samples. We also note that the large grain growth of Y-211 in the samples has prevented the Y-123 grains from growing into long parallel platelets as is usual in IGP. The Y-123 grains in different colonies are oriented differently. The microstructure is close to that obtained in sintered samples and hence, one can expect a low current density to be supported by the sample.
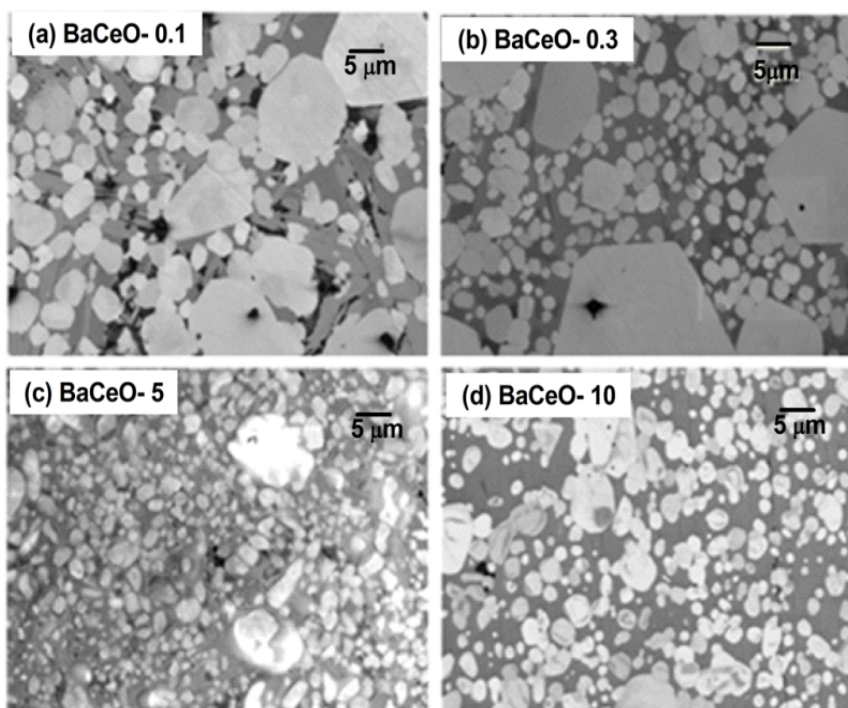
Fig. 3.26. FE-SEM images from IG process samples containing various amounts of Ba-Ce-O nanoparticles. **(a)** In the sample with the smallest Ba-Ce-O content, viz. 0.1 wt. % Ba-Ce-O, formation of the the usual long parallel platelets of Y-123 characteristic of melt processed and IG processed samples have been disturbed by the grain growth of Y-211. In **(b)**, **(c)** and **(d)**, with 0.5 wt. %, 3.0 wt. % and 10.0 wt. % of Ba-Ce-O respectively, we see that the Y-211 particle size decreases continuously with increasing Ba-Ce-O content. The parallel, long Y-123 grains have been restored in the samples with higher Ba-Ce-O content.

103

It can be observed from Fig. 3.26 that with increasing Ba-Ce-O content, the Y-211 size progressively refines and that the platelets become longer and parallel as is usual in melt grown or IG processed samples. In the sample with the maximum Ba-Ce-O content, we can observe signs of reaction between the Y-211 and Ba-Ce-O similar to that observed in ceria containing samples. With increasing Ba-Ce-O levels, the mechanism of particle division as discussed in the case of the ceria-added samples in Section 3.5, progressively offsets the effect of grain growth during preform fabrication.

A magnified FE-SEM in Fig. 3.27 for the sample containing 10 wt. % of Ba-Ce-O shows signs of reaction between the Ba-Ce-O and Y-211; Y-211 grains with Y-rich phase in the core can be seen in Fig 3.27. Some of them can be seen to be in different stages of division, and small white $BaCeO_3$ grains can be seen as in the ceria-doped samples.
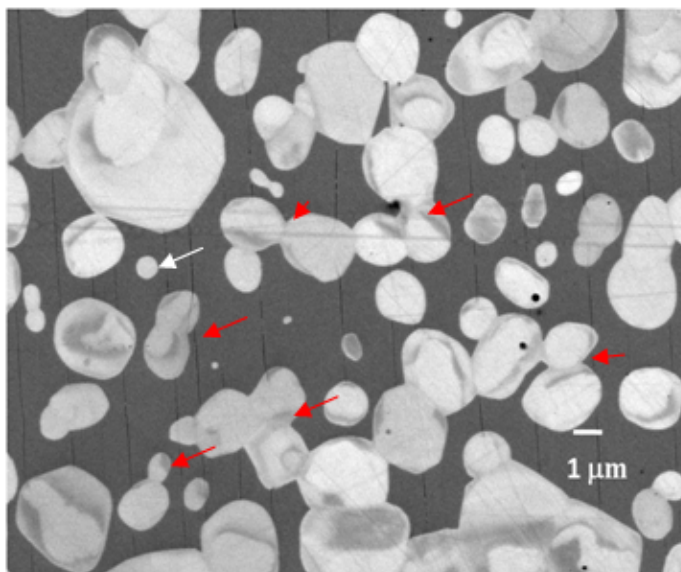
Fig. 3.27. An enlarged image from the YBCO sample with 10 wt. % of Ba-Ce-O. Y-rich cores can be observed in the Y-211 grains. Particles in different stages of division can be seen. Small white $BaCeO_3$ particles can be seen.

3.6. Conclusion

A novel method, referred to as NDSC, of introducing uniformly distributed, individual nanoparticles in Y-211 preforms used for IG processing is developed. In this context it is of interest to note that the best possible current densities have been reported in melt processed REBCO containing nanometer sized dopants: viz. nanometer-sized Gd-211 (35 mol. %) and nanometer-sized NbO_3 (0.1-0.35 mol. %) in NEG-123 gave a current density of ~600 kA/cm^2 at zero field, 200 kA/cm^2 at 4T and more than 1 kA/cm^2 up to 7 T. These values are much more than what have been reported either in melt processed or IG processed materials to date. In the present work we have devised a method of introducing well-dispersed nanoparticles in the Y-211 preform. The additives that we have worked in the present thesis show strong interaction with Y-123 and, by their dissolution in Y-123, cause considerable lowering of T_c. There is a definite potential for using the present technique to introduce well dispersed nanoparticles of non-interacting phases into the Y-211 preforms. Also, the technique can be used in conjunction with IG processing which offers advantages of near net shaping of components for application.

Since we have worked with preforms with well-dispersed nanoparticles of various materials, we have been able to track the mechanism that causes Y-211 refinement in IG processed Y-123. Addition of Pt, CeO_2, etc. has been an important step in the melt processing of YBCO bulk, due to their ability to refine Y-211 particles substantially to improve the current densities supported by such materials. Tracking the reaction paths leading to the observed refinements have been a subject matter of several studies. In the present work, we have introduced nanoparticles of grain refiners into the Y-211 preform which was subjected to IG processing

afterwards. Since the nanoparticles remained separate and adhered to the Y-211 grains during the IG process, the effect of the particles on the final microstructures could be tracked, unlike when introduced along with liquid phases.

In the case of the 10 wt. % ceria doped IG processed samples, substantial reduction in the size of Y-211 particles, with the size distributed around 0.5 μm in a narrow range, was obtained. The particle size reduction was considerably more than that obtained in normal IG processing.

An important characteristic of the materials we have worked with is their tendency to react strongly with Ba to form compounds. It has been reported that Pt refines Y-211 size in melt processed YBCO because of its ability to form a compound with barium, $Ba_4CuPt_2O_9$. It has been reported that Pt, Ce and ZrO_2 react with Ba as per the following equations:

$$Y_2BaCuO_5 + CeO_2 \rightarrow BaCeO_3 + Y_2O_3$$
$$Y_2BaCuO_5 + ZrO_2 \rightarrow BaZrO_3 + Y_2O_3$$
$$2YBa_2Cu_3O_{7-\delta} + 2PtO_2 \rightarrow Ba_4CuPt_2O_4 + Y_2O_3 + 5CuO$$
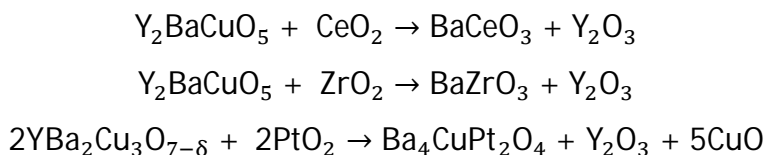
We have observed in our experiments that the nanoparticles absorb Ba from the Y-211 grains to generate one or more Y-rich core regions in them. The liquid phases, during IGP, react with the Y-poorer regions whose stoichiometry is close to that of Y-211 to form Y-123. In the process, the initial Y-211 particle develops necks and is divided into smaller particles. Many very small, about 200 to 400 nm in size, nanoparticles of the Ba-compound of the additive (like $BaCeO_3$) also are left back in the microstructure.

Another important observation is the significance of the Y-211 grain growth at the preform fabrication stage. Even small amounts of the dopants promote substantial grain growth of Y-211. This process plays an important role in deciding the final microstructure.

Ba-Ce-O nanoparticles were introduced into the Y-211 preforms to study the effect of a compound that is unlikely to draw out barium from Y-211 particles. It was observed that Ba-Ce-O nanoparticles introduced into Y-211 preforms before IG processing did not cause the formation of Y-rich cores in the Y-211 grains at small concentrations of the nanoparticles. In such cases the grain growth in the preform in the presence of small amounts of the dopant was the dominant factor deciding the microstructure. Because of the low reactivity of the system, Ba-Ce-O compound was effective in refining Y-211 grains only when it was in large concentrations.

References

[1]   K. Yamaguchi, M. Murakami, H. Fujimoto, S. Gotoh, T. Oyama, Y. Shiohara, N. Koshizuka and S. Tanaka, *J. Mater. Res.* **6** (1991) 1404

[2]   T. Haugan, P. N. Barnes, R. Wheeler, F. Meisenkothen and M. Sumption, *Nature* **430** (2004) 867

[3]   B. Batlogg, *Physics Today* **44** (1991) 44

[4]   W. M. Yang, L. Zhou, Y. Feng, P. X. Zhang, M. Z. Wu, C. P. Zhang, J. R. Wang, Z .H. Du, F. Y. Wang, Z.M. Yu, X. Z. Wu, W. Gawalek and P. Gornert, *Physica C* **305** (1998) 269

[5]   Caixuan Xu, Anming Hu, Naomichi Sakai, Mitsuru Izumi and Izumi Hirabayashi, *Physica C* **445** (2006) 357

[6]   Chan-Joong Kim, Najam ul Qadir, Asif Mahmood, Y. H. Han and T. H. Sung, *Physica C* **463–465** (2007) 344–347

[7]   N. Moutalibi, A. M'chirgui and J. Noudem, *Physica C* **470** (2010) 568–574

[8]   Y. Zhao, C. H. Cheng and J. S. Wang, *Supercond. Sci. Technol.* **18** (2005) S43–S46

[9]   P. Diko and K.C. Goretta *Physica C* **297**(1998) 211–215

[10]   D. A. Cardwell and N. Haribabu, *Physica C* **444-448** (2006) 1-7

[11]   T. Meignan, A. Banerjee, J. Fultz and P.J. McGinn ,*Physica C* **281** (1997) 109-120

[12]   W. D. Kingery, H. K. Bowen and D. R. Uhlmann, Introduction to Ceramics, Wiley, New York, (1960)

[13]   N. Ogawa, I. Hirabayashi and S. Tanaka, *Physica C* **177** (1991) 101

[14]   M. Murakami, *Mod. Phys. Lett.* **4** (1990) 163

[15]   S. Jin, T. H. Tiefel, R. C. Sherwood, R. B. van Dover, M. E. Davis, G. W. Kammlott, and R. A. Fastnacht, *Phys. Rev. B* **37** (1988) 7850

[16]   M. Morota, M. Tanaka, s. Takebayashi, K. Kimura, K. Mayamoto and K. Sawano, *Jap. J. Appl. Phys.* **30** (1991) L813

[17]   L. Shlyk, K. Nenkov, G. Krabbes and G. Fuchs, *Physica C* **423** (2005) 22-28

[18]   G. Krabbes, P. Schatzle, W. Bieger, U. Wiesner, G. Sto ver, M. Wu, T. Strasser, A. Ko hler, Litzkendorf, K. Fischer and P. Gornert, *Physica C* **244** (1995) 145

[19]   D. Litzkendorf, T. Habisreuther, R. Muller, S. Kracunovska, O. Surzhenko, M. Zeisberger, J. Riches and W. Gawalek, *Physica C* **372** (2002) 1163

[20]   L. S. Uspenskaya, I. G. Naumenko, G. A. Emelchenko, Yu. B. Boguslavskii, S. A. Zver_kov, E. B. Yakimov, D. Litzkendorf, W. awalek and A. D. Caplin, *Physica C* **390** (2003) 127

[21]   Ravi-Persad Sawh, Roy Weinstein, Drew Parks and Victor Obot, *IEEE trans. Applied. Supercond.* **19** (2009) 2941-2944

[22]   M. Muralidhar, N. Sakai, M. Jirsa, M. Murakami and I. Hirabayashi, *Appl. Phys. Lett.* **92** (2008) 162512

[23]   S. Pinol et al., *Appl. Phys. Lett.* **65(11)** (1994) 1448-1450

[24]   Chan-Joong Kim et al. *Supercond. Sci. Technol* **9** (1996) 76–87

[25]   Po-Wei Chen et al *Supercond. Sci. Technol* **24** (2011) 085021

[26]   Chan-Joong Kim and Gye-Won Hong, *Supercond. Sci. Technol.* **12** (1999) R27–R41

[27]   C. J. Kim and P. J. McGinn *Physica* C **222** (1994) 177–83

[28]   S. H. Shieh and W. J. Thomson, *Physica C* **204** (1992) 135

[29] Hideki Okamoto, Minoru Hashiba, Yulkio Nurishi and K. Hiramatsu, *J. Mater. Sc.* **26** (1991) 383-387

[30] H. I. Chen and H. Y. Chang, *Colloids and Surfaces A: Physicochem. Eng. Aspects* **242** (2004) 61–69

[31] N. Devendra Kumar, T. Rajasekharan, K. Muralidharan, A. Benerjee and V. Seshubai, *Supercond. Sci. Technol.* **23** (2010) 105020

[32] N. Vilalta, F. Sandiumenge, S. Pinol and X. Obradors, *J. Mater. Res.* **12** (1997) 1

[33] M. P. Delamare, I. Monot, J. Wang, J. Provost and G. Desgardin, *Supercond. Sci. Technol.* **9** (1996) *534–542*

[34] M. Sumida, Y. Nakamura, Y. Shiohara and T. Umeda, *J. Mater. Res.* **12** (1997) 1979

[35] C. J. kim, II hyun kuk, Gye Won Hong, Tae hyun Sung, Sang Chul Han and Jin Joong kim, *Material letters* **34** (1998) 392-397

[36] Chan Joong Kim, KI Balk KIM, Sang Chul Kwon, In Soon Chang and Dong Yeon Won, *J. Mat. Sc. Let.* **11** (1992) 346-348

[37] M. P. Delamare, I. Monot, J. Wang, J. Provost and G. Desgardin, *Supercond. Sci. Technol.* **9** (1996) 534–542

[38] K. Iida, N. Hari Babu, Y. Shi and D. A. Cardwell, *Supercond.Sci. Technol.* **18** (2005) 1421

[39] J. Y. Juang, C. L. Wu, S. J. Wang, M. L. Chu, K. H. Wu, T. M. Uen, and Y. S. Gou, H. L. Chang and C. Wang, M. J. Tsai, *Appl. Phys. Lett.* **64** (1994) 2306-2308

[40] Y. Imagawa and Y.Shiohara, *Physica C* **268** (1996) 61-70

<div align="right">Chapter-**IV**</div>

Superconducting properties of YBCO Nanocomposites

4.1. Introduction

In the earlier chapter we had discussed the macro- and microstructures of IG processed YBCO with ceria, zirconia and Ba-Ce-O additions. Dramatic differences were observed in the macro- and microstructures based on the nature of the additives and their concentration. In this chapter, we present results of current density measurements on the above samples and attempt to correlate them to the observed microstructures.

4.2. Superconducting properties of Ceria dope YBCO nanocomposites

The current densities (J_c) supported by the samples Ce-2, Ce-5 and Ce-10 (see Section 3.2 of Chapter III, for an explanation of the nomenclature) as a function of applied magnetic field, were estimated from magnetic hysteresis loops recorded at different temperatures using a PPMS facility.

The $J_c(H)$ obtained in samples Ce-2, Ce-5 and Ce-10 at 65 K and 77 K are shown in Figs. 4.1 (a) and (b) respectively. The Ce-10 sample shows the best performance and Ce-5 the worst. Since, the observed variation in $J_c(H)$ is not systematic with ceria content; we have repeated the complete experiment and confirmed that such an anomalous $J_c(H)$ behavior of the Ce-5 sample is reproducible.
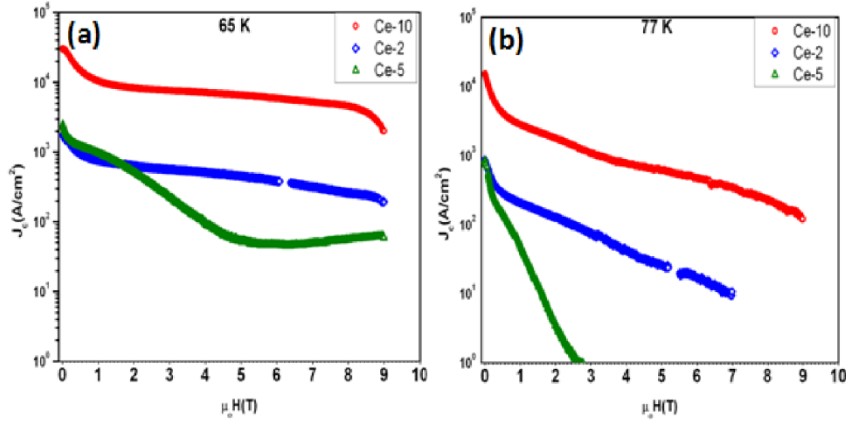
Fig. 4.1. J_c is plotted against applied magnetic field for the samples Ce-10 (red), Ce-2 (blue) and Ce-5 (green) at **(a)** 65 K, and **(b)** at 77 K.

The J_c versus H, (J_c(H)) curves, obtained in the Ce-10 sample at different temperatures are plotted in Fig. 4.2. We note that the current densities observed in the sample do not decay substantially even up to 9 T at 77 K. The observation of flat J_c(H) to high fields at 77 K is similar to that reported in the un-doped POIGP (Ce-0) sample which showed a zero field J_c of 19 kA/cm^2 at 77 K [1].
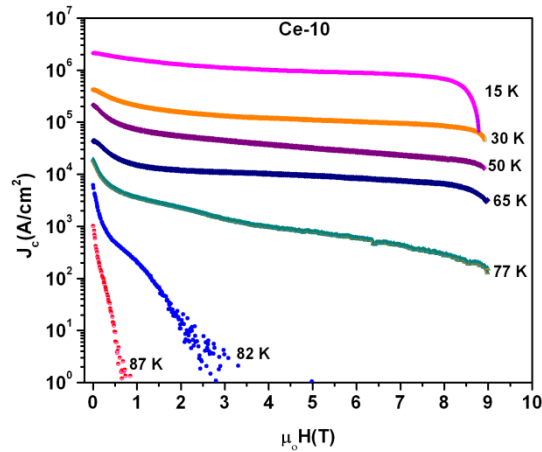
Fig. 4.2. Critical current density versus applied magnetic field is plotted for the Ce-10 sample at different temperatures.

It has been proposed [2] that the current density obtained in superconducting samples can be correlated to the size of the flux pinning defects occurring in them, as per the following equation:

$$H_p = \frac{2\emptyset_0}{\sqrt{3}(a_f)^2} \text{---------------- (4.1)}$$

where H_p is the peak field at which the maximum pinning occurs, $\emptyset_0$ is the flux quantum and a_f is the vortex lattice spacing.

It has been proposed that the observed high current density in the POIGP samples to high fields is a result of flux pinning defects occurring in the sample spanning wide size ranges [1]. The high values of J_c near 9 T in Ce-0 sample was correlated to the occurrence of wide spread twinning in the Y-123 matrix. Such twins were observed by FESEM. Their presence was also revealed by EBSD. The EBSD also suggested that the occurrence of fine defects around the Y-211 particles was associated with dense distribution of fine Y-211. Transmission electron microscopy studies [3] on the Ce-0 sample revealed the presence of still finer defects ~15 nm starting at the twin boundaries. The Ce-10 and Ce-2 samples show J_c values almost independent of H up to 9 T at 65 K, just as the Ce-0 sample. This might be correlated with the fine grain (≥ 0.5 µm) size of the Y-211 and a narrow distribution in Y-211 size in Ce-10, shown in Fig. 3.11. Similar microstructure but with a Y-211 distribution in larger size range (≥ 1 µm) was observed in Ce-2 sample. Fig. 4.3 shows twinning in all the CeO_2 doped samples. Absence of macro defects and presence of homogeneously distributed Y-211 and nanoparticles and the resultant twinning in Ce-2 and Ce-10 samples account for the observed flat J_c, being almost independent of H up to 9 T at 65 K. Further discussion can be found in section 4.4.
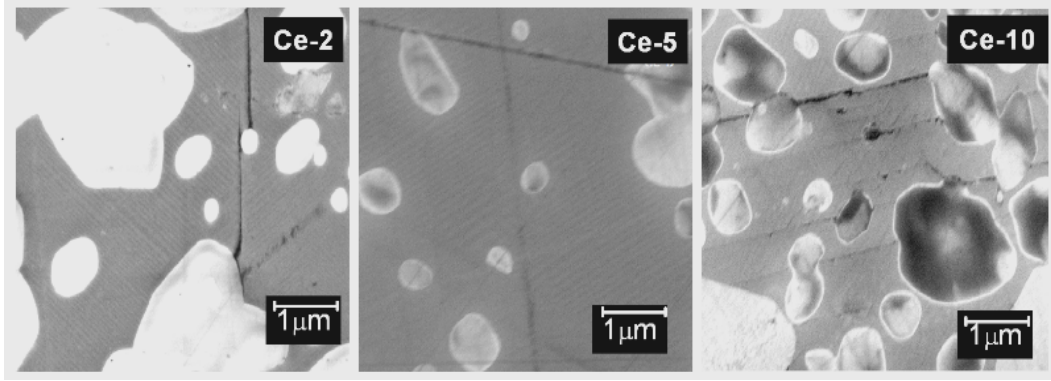
Fig. 4.3. Twinning is observed in all CeO$_2$ doped YBCO nanocomposites (Ce-2, Ce-5 and Ce-10).

The electrical resistivity and ac susceptibility of the samples Ce-2, Ce-5 and Ce-10 were measured as a function of temperature following the procedures discussed in Chapter II, Section 2.6. and 2.7.1. The results are shown in Figs. 4.4 (a) and (b) respectively.
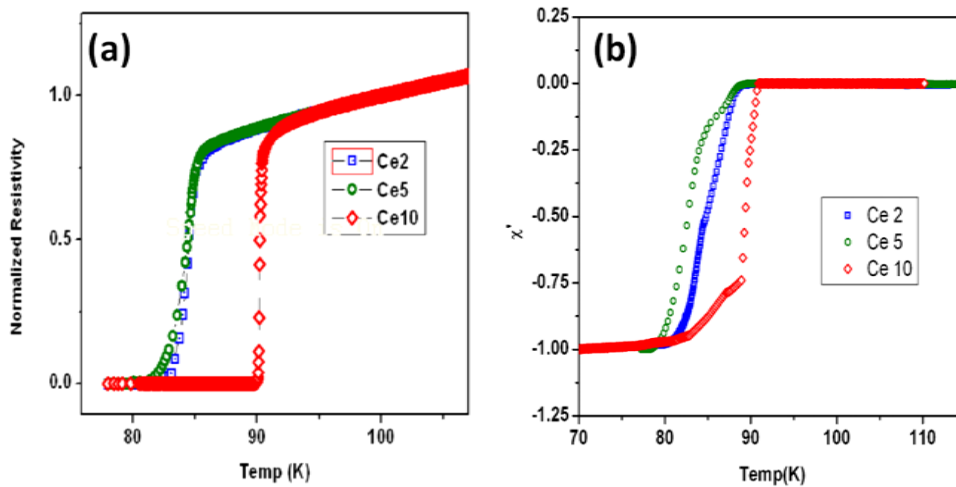
Fig. 4.4. (a) The electrical resistivity, and **(b)** the real part of ac susceptibility of the samples Ce-10 (red), Ce-2 (blue) and Ce-5 (green) are plotted with respect to temperature.

A shift in the diamagnetic transition to below 92 K and considerable width of the transition in χ' vs. T can be observed predominantly in Ce-2 and Ce-5. An examination of the curves, in Fig. 4.4, show that in the Ce-10 sample, there is a considerable amount of Y-123 phase with T_c close to 92 K, whereas in Ce-2 and Ce-5 samples, substantial part of the material consists of lower T_c phases. This can possibly be attributed to the dissolution of Ce in the Y-123 phase forming solid solutions having lower T_c.

In Fig. 3.20 of Chapter III, it was observed using elemental mapping that the outer regions of the Y-211 grains contained ceria. Such regions dissolve in the liquid phases to generate a matrix of Y-123 containing some amount of cerium. Cerium substitution in Y-123 lowers the T_c as can be seen in Fig. 4.5 [4].
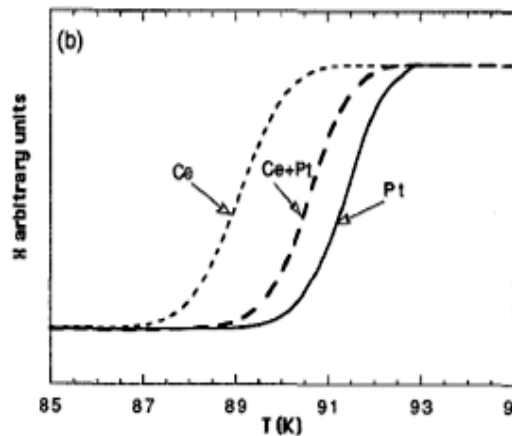
Fig. 4.5. The figure shows that the addition of ceria and Pt to Y-123 lowers its superconducting transition temperature [4]. The effect is less pronounced with Pt addition, and this suggests that the J_c of Pt-containing samples are likely to be seriously affected by the additive. We note by comparing the present figure with Figs. 4.4 (a) and (b) of measurements in our samples that the Ce-10 sample retains considerable volume of Y-123 without ceria dissolution. It might be noted from Fig. 3.6 that the ceria nanoparticles in the preform used for the fabrication of the Ce-10 sample grow into much fewer number of nano-rods, which get converted to barium cerate particles during the IG process. This leads to localization of ceria distribution in the Y-123 matrix of the Ce-10 sample.

Ce was detected by elemental mapping in the Y-123 phase in the regions close to the Y-211 grains. The lower current densities observed in the Ce-2 sample in comparison with the Ce-10 sample, and the relatively lower current densities of both the Ce-10 and Ce-2 samples in comparison with the Ce-0 sample, might be attributed to the presence of significant amount of low T_c phase containing cerium dissolution in the 123 phase.

The difference in the behavior of the Ce-5 sample can be traced to the nature of the preform used in fabricating it. The SEM micrographs of Y-211 preforms with varying amounts of ceria nanoparticles, after 4 h at 950 ^{o}C, are reproduced from Chapter III (Fig. 3.6) in Fig. 4.6 for convenience of discussion.
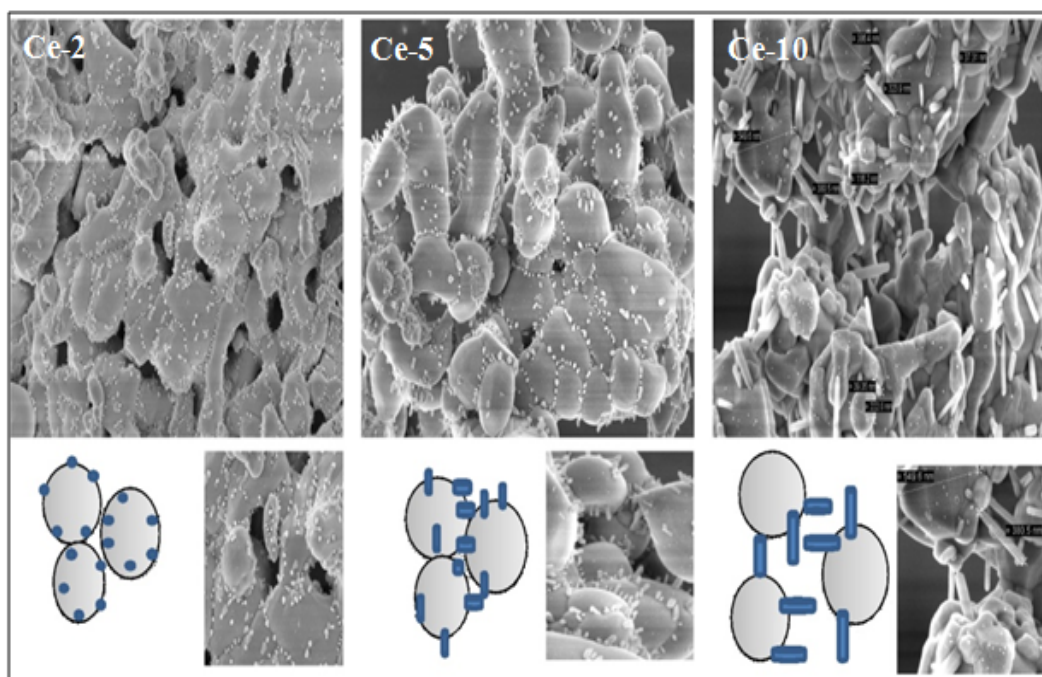
Fig .4.6. The micrographs in the top row show from left to right, the preforms used in the fabrication of the Ce-2, Ce-5 and Ce-10 samples, respectively. The preform used in the fabrication of the Ce-2 sample has the least amount of ceria and retains its porosity. In the preform used for the fabrication of the Ce-10 sample, the porosity

is retained because the ceria nanoparticles fuse among themselves to form ceria nano-rods. In the preform used in the fabrication of the Ce-5 sample, the Y-211 particles have fused together in the presence of ceria, eliminating continuous porosity needed for liquid phase entry.

It can be observed that the preforms with 2 and 10 wt. % of ceria nanoparticles have enough porosity to facilitate infiltration of liquid phases during the IG process, but in the preform with 5 wt. % ceria nanoparticles, the Y-211 particles are nearly fused blocking the entry of liquids. As schematically shown in Fig. 4.6, the sample with 10 wt. % of ceria is able to retain porosity because of the tendency of the ceria particles to grow into nano-rods, a few hundreds of nanometers long, with a diameter of 40-60 nm. The formation of the nano-rods makes the preform porous.

The mechanism proposed above for the difference in the behavior of the Ce-5 sample is supported further in Fig. 4.7. In the Infiltration Growth experiments, a Y-123 pellet, which served as a source of liquid phases, was kept on top of the Y-211 preform. After the liquids infiltrate the preform at a few tens of degrees above the peritectic formation temperature of Y-123, the Y-123 pellet would shrink considerably. This is shown schematically in Fig. 4.7 (a). In Figs. 4.7 (b) and (c), we show the Ce-10 sample after the IG process. It can be observed that the Y-123 pellet on top has shrunk considerably and the Y-211 pellet retained has its size as expected. In Figs. 4.7 (d) and (e), it can be seen that in the case of the Ce-5 sample, there is not much shrinkage of the Y-123 pellet. This shows that the liquid phases were unable to infiltrate into the Y-211 preform in this case due to the fused Y-211 particles reducing its porosity.
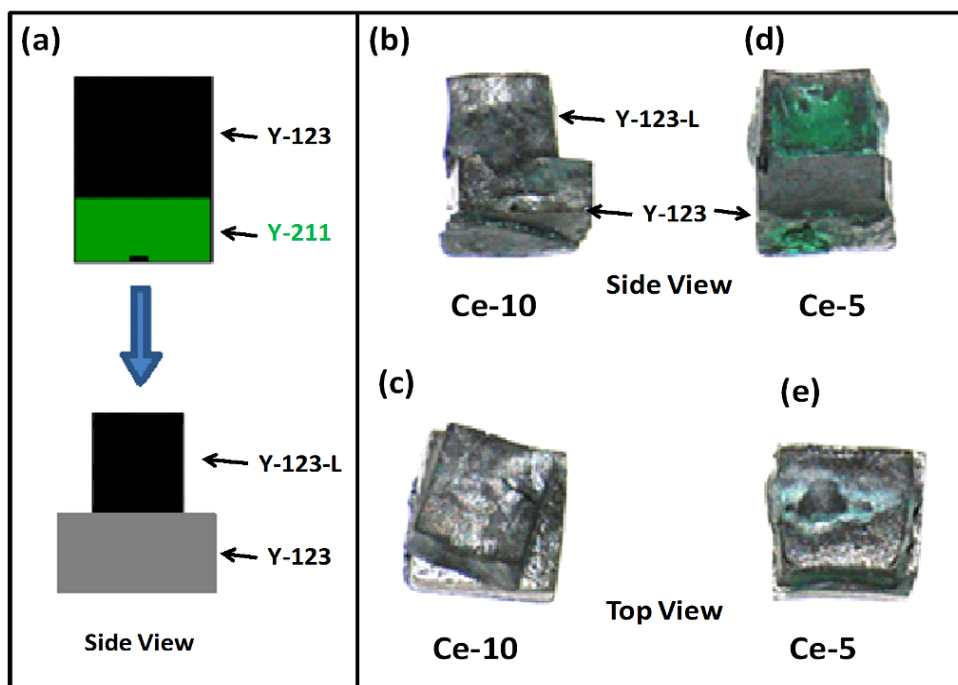
Fig. 4.7. (a) A side view of the arrangement used in the IG process is shown schematically. After melting and infiltration of the liquid phases into the Y-211 preform the 123 pellet shrinks. In **(b)** and **(c)** the side and top views respectively, of the Ce-10 sample are shown after IG processing. The observed shrinkage in the top Y-123 pellet is due to infiltration of liquid phase from Y-123 into the Y-211 perform, can be observed. **(d)** and **(e),** which show the side and top view respectively of the Ce-5 sample demonstrates the fact that the Y-123 pellet had not shrunk after the experiment suggesting that the entry of liquid phases into the Y-211 perform was blocked in this case.

Fig. 4.8 shows the FE-SEM image of the Ce-5 sample in comparison with those of the Ce-2 and Ce-10 samples at the same magnification. It is observed from the low magnification picture of the Ce-5 sample that there is considerable amount of macro-porosity occurring as a result of improper infiltration. On the other hand the Ce-2 sample shows very little porosity, and the Ce-10 sample, almost none at all.

(a)   (b)   (c)
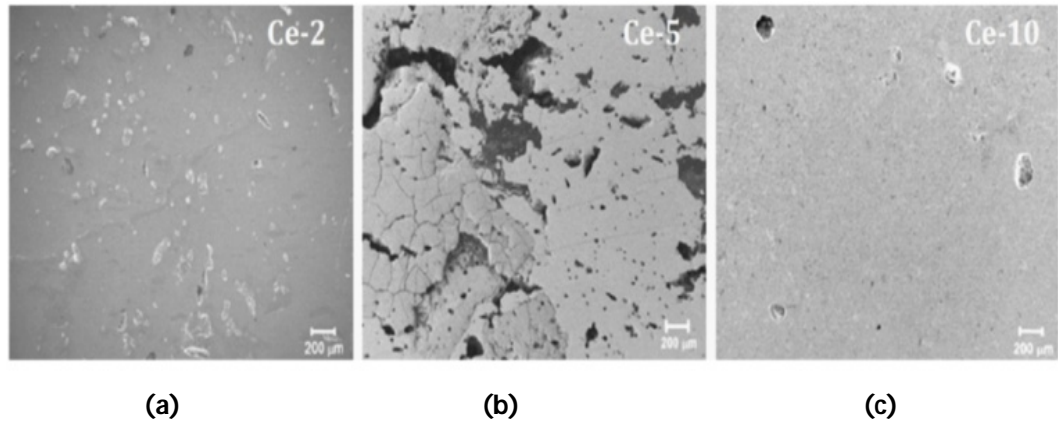
Fig. 4.8. It can be observed that there are very few macroscopic defects in the **(a)** Ce-2 sample and **(c)** the Ce-10 sample. **(b)** Large areas with macroscopic defects can be observed in the Ce-5 sample due to improper liquid phase infiltration.

Table 4.1 summarizes the information on the defect sizes in the samples Ce-2, Ce-5 and Ce-10. It can be observed from the Table that Ce-5 sample shows the maximum amount of porosity and also the maximum values for the inter platelet gaps. The size and quantum of defects then decrease in the order Ce-2 to Ce-10. The superconducting performances of the samples also decrease in the same order.

	Y-211 Avg. size	Porosity (%)	Platelet width
Ce-2	~1-2 µm	~7	2-5 µm
Ce-5	~1 µm	~16.5	10 µm
Ce-10	0.5 µm	~1.5	~500 nm

4.3. Flux pinning force

Flux pinning forces (F_P) [5] are calculated from the J_c vs. H graphs at 65 K and 77 K for the Ce-2, Ce-5 and Ce-10 samples, using the following equation

$$F_p = J_c \times \mu_0 H \text{ ---------------- (4.2)}$$

F_p is plotted as function of the applied field at 65 K and 77 K in Figs. 4.9 (a) and (b) respectively.

119
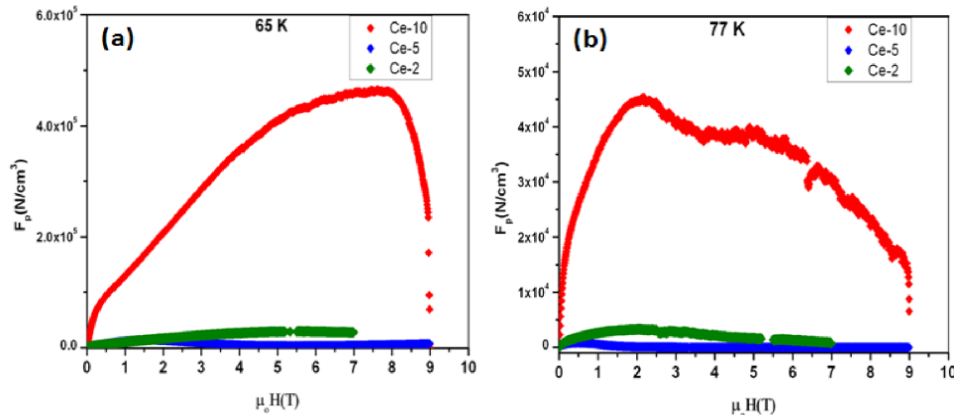
Fig. 4.9. Flux pinning forces (F_P) are plotted as function of the applied field at **(a)** 65 K and **(b)** 77 K, for the Ce-2 (green), Ce-5 (blue) and Ce-10 (red) samples.

The flux pinning force in the Ce-10 sample which has extremely fine Y-211 grains and also wide-spread twinning, shows very high levels of flux pinning in comparison with the Ce-2 and Ce-5 samples, and the flux pinning in the Ce-10 sample peaks at relatively high magnetic fields at 65 K and in a broad range of fields at 77 K.

4.4. Flux profile studies

In the discussion of the observed $J_c(H)$ of the Ce-2, Ce-5 and Ce-10 samples in the above section, we observe that the $J_c(H)$ is strongly dependent on macroscopic features such as porosity and other kind of defects like platelet gaps, which might be considered as weak-links. Experiments on flux penetration into the sample on application of magnetic field would be of interest in exploring the role of such weak-links on the $J_c(H)$ of the sample. The experiment consists of applying a dc field (in the order of Teslas) and then studying the flux penetration into the sample by using an ac field as a probe. In order to understand flux penetration at various dc fields into the present samples, flux penetration depths were calculated from the real part

of ac susceptibility measured in the Ce-10 and Ce-2 samples with increasing amplitude of ac field. Flux penetration depth (p/R) is determined using the formula suggested by Campbell [6], which is given below

$$\frac{p}{R} = 1 - \sqrt{-\frac{1}{k}\frac{dS}{dH_{ac}}} \qquad \text{---------- (4.3)}$$

p/R is the normalized penetration depth where R is the radius of a cylindrical sample and p is the depth to which magnetic field has penetrated. An external dc field (H_{dc}) and a small superimposed ac field (H_{ac}) parallel to the longest axis of the sample are applied. The induced signal in the secondary coils (with one of the two coils containing the sample) is fed to a lock-in amplifier and the in-phase signal (S) is measured as a function of ac field amplitude.

The above experiments were carried out at 77 K using the PPMS facility. In Fig. 4.10, we plot the variation in p/R, computed using Eq. 4.3, against the ac field amplitude for the Ce-10 sample at different applied dc fields which exhibit different lines shifted along the p/R axis. The intercept of the lines on the p/R axis gives p_o/R which is a measure of reversible fluxoid motion through the sample discussed in literature [7]. The entry of flux into voids and cracks contributes to a finite p_0/R, which is a shift along the p/R axis. In textured high J_c superconductors there are different types of weak-links like domain boundaries, platelet gaps, and presence of low T_c phases in the path of shielding current loops. Flux enters these weak-links at different applied field strengths depending on the distribution and nature of the weak-links and their J_c. In a sample containing superconducting materials of varying T_c, such 'voids' might also be constituted by regions of the sample gone normal at the applied dc field. Regions of stronger flux pinning do not contribute to reversible fluxoid motion or shift along p/R axis. This causes a

continuous variation of p_o/R with increase in dc field. A finite value of p_o/R under a constant dc field suggests that the flux has already entered the sample to a finite depth and application of ac field induces further entry as described by the lines shown in Fig. 4.10 for Ce-10 sample.
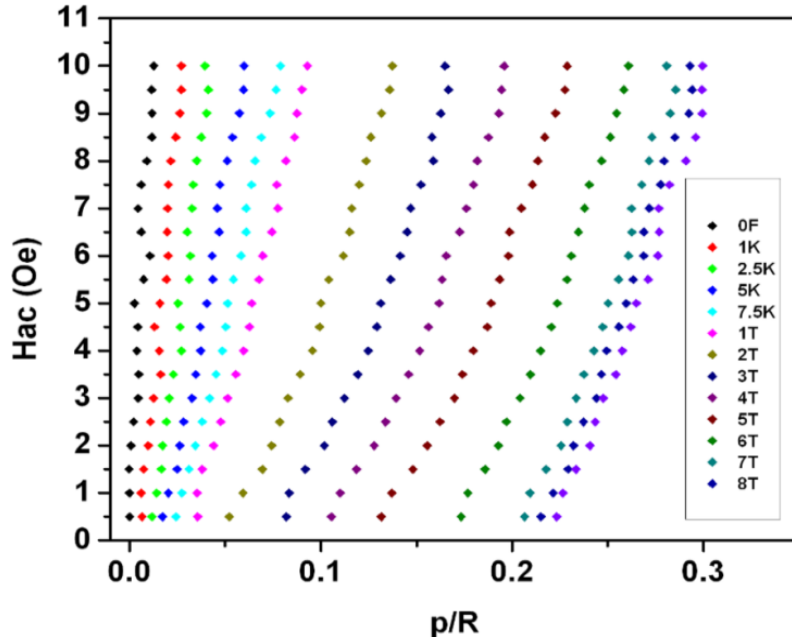
Fig. 4.10. A plot showing Normalized magnetic flux penetration depth (p/R) into the Ce-10 sample on the X-axis, with the applied ac magnetic field on the Y-axis. The graphs correspond to observations at various applied dc fields, from 0 to 8 Tesla towards the right. R is the radius of the sample; p is the depth to which the magnetic flux penetrates into the sample.

In Figs. 4.11 (a) and (b), we compare the variation in p_o/R with the dc field strengths for the Ce-10 and Ce-2 samples, respectively. Distinct changes in the slope can be observed in both the figures. A slope change suggests that the flux is starting to enter a different region in the sample with a different J_c. In Ce-10, (Fig. 4.11 (a)), at low applied dc fields (0 - 0.5 T), the flux penetrates into ~2 % of the sample, suggesting a low J_c region that allows flux

penetration at low fields. At higher dc fields (0.5-7 T), the flux continues to enter into weak-link regions of higher J_c, penetrating up to 20 % of the sample. Beyond 7 T, there is a further slope change indicating much slower flux entry between 7–9 T, with an increase from 20 to 22 % of the sample penetrated by 9 T. In contrast, in the Ce-2 sample, Fig. 4.11 (b) shows only one slope change at low fields, and the flux entry is much more and is up to 36 % of the sample at 9 T. An understanding of this behavior is attempted in comparison with the microstructural features observed in Figs. 4.12- 4.13, recorded at different magnifications.
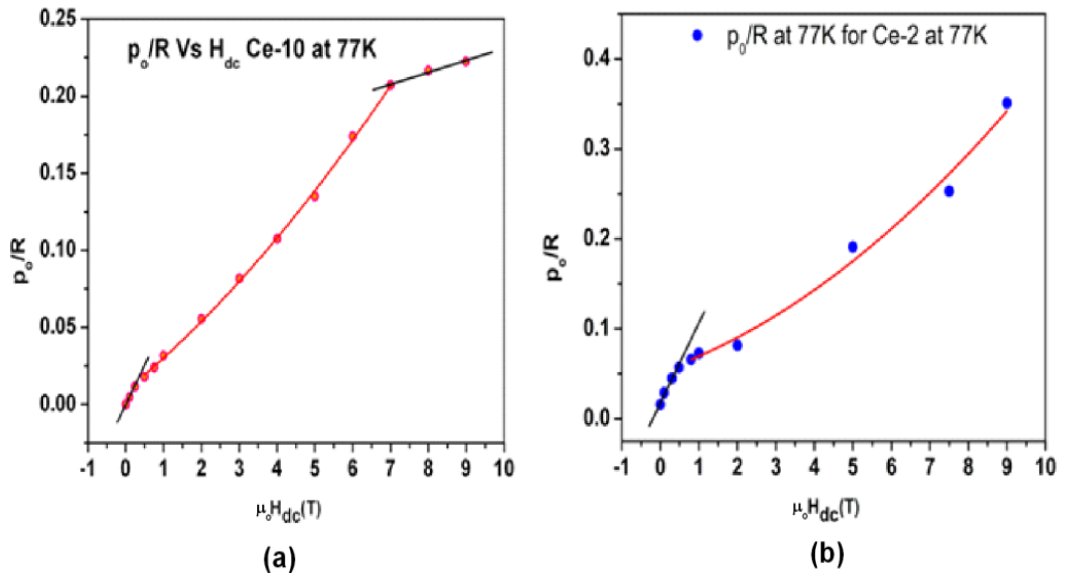
Fig. 4.11. p_o/R, a measure of flux penetration into YBCO matrix at 77 K, is plotted versus applied dc magnetic field **(a)** for the Ce-10 and **(b)** for the Ce-2 samples.

The initial high slope regions in the p_o/R versus H_{dc} plot, indicating easy entry of flux, and observed at low fields, might be associated with flux penetration into regions such as cracks and voids. Flux penetration up to 6 % in Ce-2, in contrast to 2 % in Ce-10, can be correlated to the higher porosity levels in Ce-2 sample as can be seen in Figs. 4.12 and 4.13.
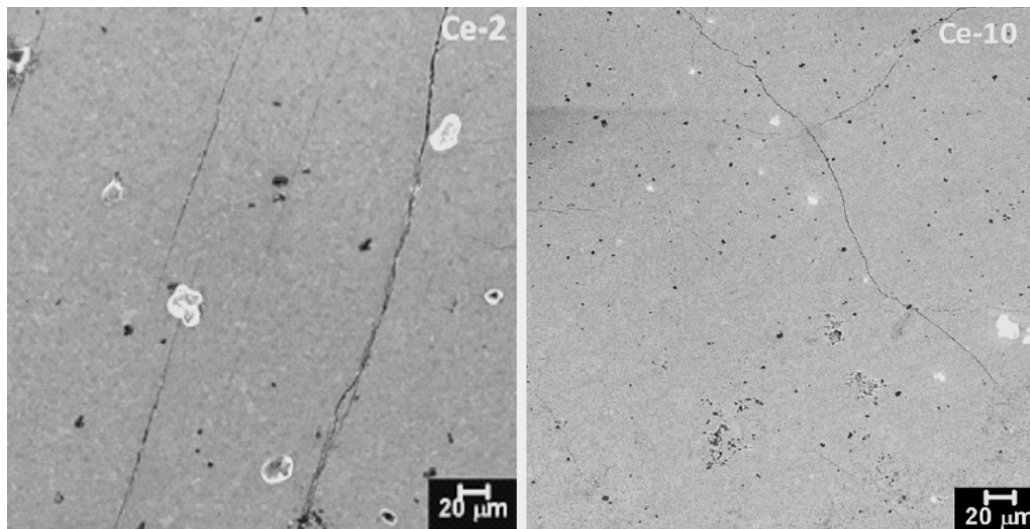
Fig. 4.12. FESEM micrographs obtained on Ce-2 and Ce-10 samples at a magnification of 500 X, shows macro defects such as pores, cracks etc. In Ce-2, large pores (~5 μm) and cracks can be seen almost through the entire field of view in the smaple accounting for nearly 5-7 % of macro defects, whereas in Ce-10, very fine pores and cracks are seen acounting for a smaller percentage (1.5-2 %) of macro defects.

The region between 0.5 and 9 T for Ce-2 in Fig. 4.11 can be associated with progressive flux entry into the lower T_c region, more of which turns normal with increasing dc field, and increases to 40 % of the sample at 9 T. Amount of lower T_c phases is considerably large in Ce-2 compared to Ce-10 as was seen in Fig. 4.4 (b). In the case of Ce-10, the lower T_c phases are less in volume in comparison with the high T_c component, and this accounts for the lower flux penetration of 22 % into Ce-10 at 9 T. Much slower rate of flux entry between 7 T to 9 T in the Ce-10 sample is possibly associated with flux entry into the high T_c (~92 K) matrix seen only in the Ce-10 sample (see Fig. 4.4).
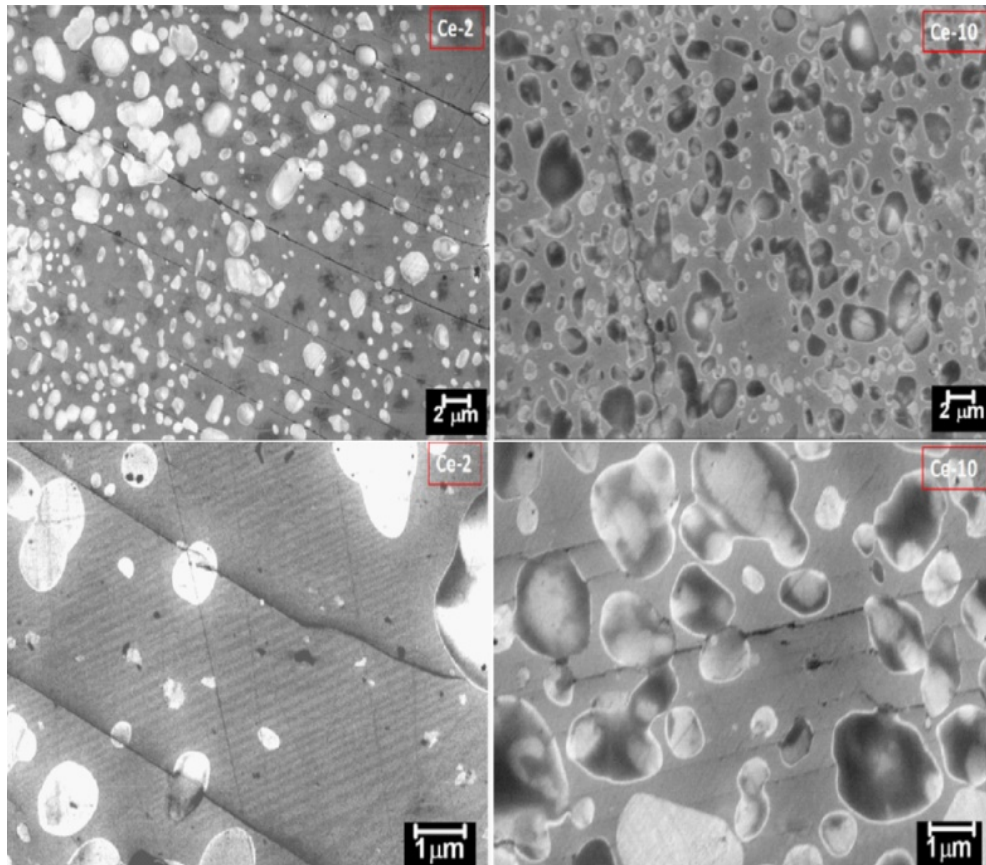
Fig. 4.13. Micrographs shown in the upper row are obtained at a magnification of 5000 X for both Ce-2 and Ce-10 samples. Ce-2 shows platelet cracks which are not seen in Ce-10. The micrographs shown below are obtained at a magnification of 20,000 X for Ce-2 and Ce-10; they show large plateelet gaps in Ce-2, and very fine platelet gaps in Ce-10 and most of the platelet gaps in Ce-10 are fused.

In Fig. 4.14, the $J_c(H)$ of the IG processed Y-123 sample containing 10 wt. % zirconia nanoparticles is plotted in comparison with that of the Ce-10 sample. The perfomance of the Zr-10 sample is poor; and the performance of samples containing lower amounts of zirconia were even poorer. It is evident from the microstrures of the samples in Fig.3.9, that the poor performance of the zirconia containing samples might be attributed to excesssive Y-211 grain growth at the preform formation stage. This had made it difficult for

125

the liquid phases to enter uniformly into the preforms leading to large grain growth for the Y-211 phase.
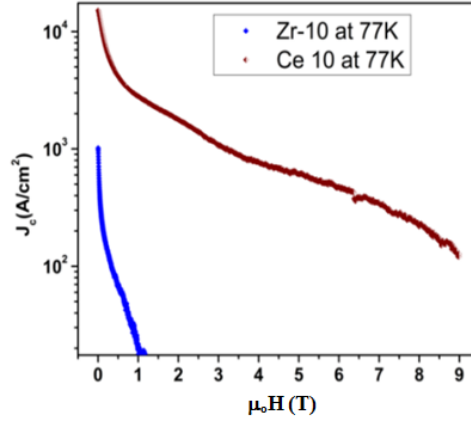
Fig. 4.14. J_c versus H of the IG processed Y-123 sample containing 10 wt. % zirconia nanoparticles is plotted in comparison with that of the Ce-10 sample, at 77 K.

In Fig. 4.15, we plot the critical current densities obtained in the samples containing 0.1 wt. %, 0.5 wt. %, 3 wt. % and 10 wt. % Ba-Ce-O nanoparticles.
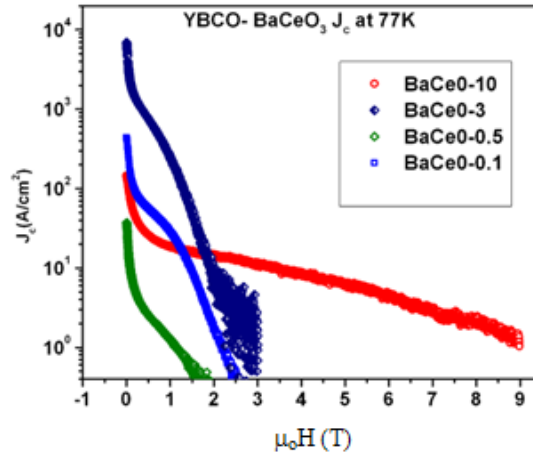
Fig. 4.15. Variation of J_c with H at 77 K, in YBCO composites fabricated from preforms containing various amounts of Ba-Ce-O nanoparticles; 0.1 % (green), 0.5 %(blue) 3 %(dark blue) and 10 %(red) in weight with respect to Y-211.

It might be recalled from Fig. 3.26 (reproduced in Fig. 4.16) that the sample with the smallest amount of Ba-Ce-O had the least favorable microstructure to support high current densities; the sample had large Y-211 grains generating isolated colonies of short Y-123 platelets in different orientations. By comparing with the preform microstructure, we had concluded that the particle refinement caused by small amounts of Ba-Ce-O was not sufficient to bring down Y-211 sizes substantially. In samples with higher Ba-Ce-O content, we find that, with increasing Ba-Ce-O content, the Y-211 size becomes more and more refined and the grain structure of the Y-123 with long parallel platelets is restored back in the case of Ba-Ce-O-10, which also showed better performance in field dependence of J_c.
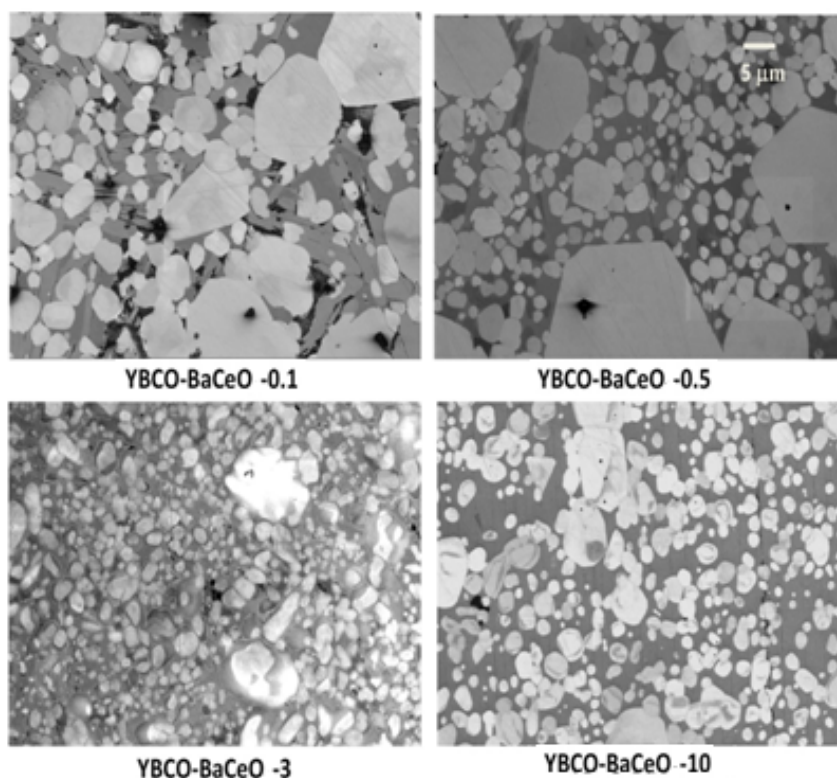
Fig.4.16. FESEM micrographs obtained on YBCO samples with 0.1 %, 0.5 %, 3 % and 10 % of Ba-Ce-O nanoparticles at a magnification of 2,000 X.

4.5. Conclusions

Melt processed YBCO containing Pt, CeO_2, ZrO_2 and $BaCeO_3$ have been widely studied because of the ability of these additives to considerably refine Y-211 grain size in the final product [8-11]. The grain size refinement is expected to result in enhanced current densities in the materials. However, the observed results were not absolutely systematic with the dopant concentration and there were considerable differences based on the processing route. For instance, in the samples differently processed in the presence of Pt, grain refinement of Y-211 was observed in some cases and was not observed in some other cases [8]. It was observed that in the samples where the initial processing led to Y-211 grain growth, Pt was not effective in reducing the Y-211 size later on. Also, the current densities reported in the samples are widely scattered based on the processing route.

In experiments reported in the present thesis, we find that even very small amounts of ZrO_2 and Ba-Ce-O additives cause substantial deterioration in the current densities in comparison with that obtained in undoped IG processed samples. A dramatic effect is observed in the sample containing only 0.1 % of Ba-Ce-O; in this case the microstructure of the IG processed sample gets close to that of a sintered sample and the current densities drop to very low levels. The additives, when present in larger amounts, improve the current densities supported by the samples substantially. These observations can be explained by the fact that, even with very small amount of these additives, Y-211 particles in the preform fuse leading to considerable Y-211 grain growth. The effect of more amounts of additives is to divide the Y-211 grains into smaller particles by a process discussed in Chapter-III. The fusing and grain growth of Y-211 can also affect the liquid phase entry into the preforms and affect the performance of the samples. The behavior of the

sample containing 2 wt. % of ceria was somewhat different; in this case reaction between Y-211 grains and their fusing in the preform was not as much as in other samples. Therefore, J_c versus H for Ce-2 samples was relatively better. The Ce-10 sample also did not lose porosity in the preform because of the formation of ceria nano-rods; thereby the infiltration of liquid phases into the preform was good, and also the starting grain size of the Y-211 particles were close to that of particles in the powder used, i. e. ~1 μm. Hence, the Y-211 particles in IG processed Ce-10 sample were much smaller than in the Ce-0 sample, i.e. in the IG processed sample without any additives. It might be noted that a Y-211 distribution finer than what is obtained in the Ce-10 sample has not been generated in MG or IG processed samples until now. We observe that the current densities in these samples remain flat up to 9 T magnetic field and the irreversibility field is better than 9 T at 77 K. This is attributed to the presence of the very fine second phase particles present in it and because of extensive nano-twinning. However, in spite of substantial refinement of Y-211, there is no remarkable improvement in J_c in Ce-10 sample over that in the Ce-0 sample.

The lowered J_c in the doped samples, in spite of a 'favorable' microstructure, might turn out to be a difficult problem to solve; it results from lower T_c of the Y-123 phase with the dopant dissolved in it. It is therefore likely that the method that we have developed in this thesis to distribute nanoparticles individually and separately in the preform will be more attractive in the case of nanoparticles which do not react with Y-211 or Y-123; an example would be nanoparticles of Gd-211 and NbO_3 which have been introduced into melt processed NEG-123 system to dramatically improve its J_c, as discussed in the literature [12].

References

[1]   N. Devendra Kumar, T. Rajasekharan, Ravi C. Gundakaram, and Vummethala Seshubai, *IEEE transactions on applied superconductivity* **21** (2011) 3612-3619

[2]   H. Suematsu, H. Okamura, S. Nagaya and H. Yamauchi, *Supercond. Sci. Technol.* **12** (1999) 274

[3]   N. Devendra Kumar, T. Rajasekharan, K. Muraleedharan, A. Banerjee and V. Seshubai, *Supercond. Sci. Technol.* **23** (2010) 105020

[4]   I. Monot , K. Verbist M. Hervieu , P. Laffez , M.P. Delamare J. Wang G. Desgardin and G. Van Tendeloo, *Physica C* **274** (1997) 253-266

[5]   M. Murakami, **S.** Gotoh, H. Fujimoto, K. Yamaguchi, **N.** Koshizuka and **S.** Tanaka, *Supercond. Sci. Technol.* **4** (1991) s43-50

[6]   A. M. Campbell, *J. Phys. C* **2** (1969) 1492

[7]   N. Hari Babu, T. Rajasekharan and V. Seshu Bai, *Physica C* **330** (2000) 203–207

[8]   Y. Imagawa and Y. Shiohara, *Physica C* **268** (1996) 61-70

[9]   D. Shi, S. Sengupta, J. S. Lou, C. Varanasi and P. McGinn, *Physica C* **213** (1993) 179

[10]   Kim et al. *Journal of ceramics Processing Research* **7** (2006) 235

[11]   M. P. Delamare, I. Monot, J. Wang, J. Provost and G. Desgardin, *Supercond. Sci. Technol.* **9** (1996) 534–542

[12]   M. Muralidhar, N. Sakai, M. Jirsa, M. Murakami and I. Hirabayashi, *Appl. Phys. Lett.* **92** (2008) 162512

<div align="right">**Chapter-V**</div>

Shape forming of YBCO superconductors

5.1. Introduction

In the earlier chapters, we have discussed the introduction of nano-sized inclusions into YBCO matrix in IG processing. It is of interest to have a near net shape processing technique which is compatible with the slurry-based processing technique developed therein. Some of the potential applications of bulk REBCO high temperature superconductors are as magnetic shields , tubes carrying high currents for use as fault current limiters, large flat disks for use as levitation platforms , vibration dampers , transmission antennas etc. Fabrication of YBCO into different shapes is of particular interest from the view point of a large number of possible practical applications.

Gelcasting is a well established ceramic processing technique enabling near-net shape fabrication. In this chapter, we have extended the technique to the fabrication of high current density near net shaped superconductor parts.

5.2. Shape forming techniques for ceramics

YBCO is a black ceramic powder. There are various techniques employed for the fabrication of ceramic products. Some of them are:

Pressure casting: Green bodies are processed by compacting ceramic powders under pressure. A small amount of binder, added to the powder holds the particles together so that the green body maintains its shape after removal of the pressure. Uniaxial pressing, cold and hot isostatic pressing are very widely used variants of pressure casting technique. Uniaxial pressing is

limited to fabrication of simple shapes and any change in shape/dimensions requires new set of dies. Cold/ Hot isostatic pressing can deliver complex shaped products [6-7] than uniaxial pressing but it is quite expensive for small scale productions. Pressure casting cannot be integrated to modern and advanced techniques such as rapid prototyping.

Slip casting: Suspension of colloidal powders in an immiscible liquid, usually water with help of dispersants is called slip. In slip casting a slip is cast into a porous mold, usually made of plaster .Capillary suction draws the liquid into the mold and leaves a layer of particles deposited against the walls of the mold. Pressure can be applied to the mold to increase the rate of deposition. Hollow objects can be made by allowing a certain layer thickness to form before draining the rest of the slip from the mold. Solid objects can be made by allowing the whole volume to solidify. Slip casting is an economical process for the fabrication of objects such as crucibles and chinaware. A disadvantage of this method is that it is relatively slow, taking tens of minutes to hours to cast a part.

Injection molding: Ceramic injection molding is similar to plastic injection molding. A heated powder and binder mix is forced into a mold under pressure and allowed to cool before being removed from the mold A polymer or wax binder is usually used for injection molding and this produces high strength green parts, but the drying and burnout steps are long and difficult. The die can also be expensive and usually has long lead times. Die life will be shortened by the abrasive nature of the materials used.

Gelcasting technique: Gelcasting is a generic process. In this process, high-quality complex-shaped ceramic parts were formed by in-situ polymerization through which a macromolecular network is created to hold the ceramic particles together. Unlike injection moulding, gelcast parts have

low polymer content and hence can avoid complicated binder burnout process. Gelcast green bodies additionally have uniform density and high mechanical strength, which is of great advantage for handling the parts before firing and especially for large castings. Additionally, this process does not involve use of expensive machinery which causes a drastic reduction in the overall cost and energy [10-14]. The compatibility of the process with wide range of mold materials and mold type opens up a range of options for shaping: staring from simple sand molds to complicated rapid proto-typing (RPT) molds.

Table 5.1. Advantages and disadvantages of various ceramic processing techniques.

Property	Gelcasting	Slip casting	Injection Molding	Pressure Casting
Molding time	5-60 min	1-10 hrs	10-60 sec	10 min - 5 hr
Strength (As-formed)	Moderate to high depending on gel system	Low	High	Low
Strength (Dried)	Very High	Low	N/A	Low
Mold Materials	Metal, glass, polymer, wax	Plaster	Metal	Porous plastic
Binder Burnout	2-3 hours	2-3 hours	Up to 7 days	2-3 hours
Molding defects	Minimal	Minimal	Significant	Minimal
Maximum Part Dimension	> 1 meter	> 1 meter	~30 cm, 1 dimension must be ≤1 cm	~1 meter
Warpage during drying/binder removal	Minimal	Minimal	Can be severe	Minimal
Thick/thin sections	No problem	Thick section increases time of cast	Problems with binder removal in thick sections	Thick section increases time of cast
Particle size	Viscosity goes up as size goes down	Casting time goes up as size goes down	Viscosity goes up as size goes down	Casting time goes up as size goes down

In the context of the discussion above, we note that none of the processes above can be directly applied to Y-123, as subsequent melt processing to generate a microstructure that supports high current density will shrink and distort the product. An alternative is to fabricate Y-211 into the required shape and to use it as a preform in the IG process. Y-211 does not react with water and hence water-based processing routes are feasible. When complex shapes are desired, one can use the computer-based manufacturing technique of rapid prototyping to manufacture the preform/mold. Such molds can be used in conjunction with the gelcasting technique to manufacture useful components. The technique will integrate with relative ease with the NDSC process for the introduction of nanoparticles into IG processed Y-123 product.

In the present work, we have first standardized the gelcasting technique and Rapid Prototyping procedure using alumina as a prototype material. This process was also extended to tungsten products. Procedures appropriate for shape forming Y-211 preforms were subsequently optimized. Various experimental methods involved in the optimization of gelcasting are discussed in section 2.5 of chapter II.

5.2.1. Gelcasting of Al_2O_3

Gelcasting technique was invented by Janney and Omatete by combining ideas from polymer chemistry and ceramic processing techniques. The ease of making complex parts of ceramic materials through gelcasting technique has drawn lot of attention for fabricating functional ceramic components . Fig 5.1 shows the flow chart for the gelcasting process which was discussed briefly earlier in Section 2.5 of chapter II.
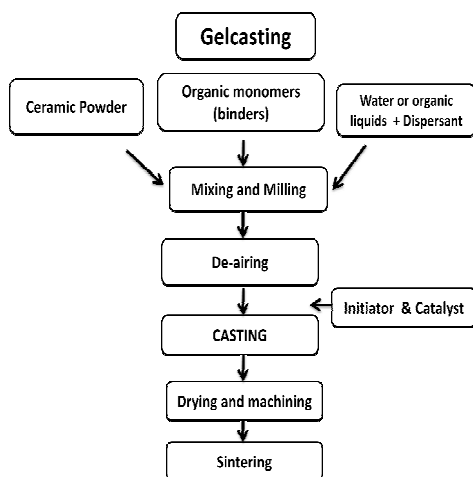
Fig 5.1. A schematic representation of gelcasting process.

The crucial element of the gelcasting process is to identify the characteristics of powder, finding out the best dispersing agent to get a free flowing slurry with high solid content (~50 vol. %) and understanding the binder removal process.

Alcoa alumina A16SG of specified particle size 0.34μm and a locally available alumina powder from NALCO, India were used in our experiments. Dispersants such as DARVAN 821A, DOLAPIX PC21, DOLAPIX PC75, DOLAPIX A88, PRODUCT KV 5068, PRODUCT KV 5166 were obtained from Zschimmer & Schwarz, Germany. Surface areas of the Alcoa alumina as well as of the other locally available alumina (1-3μm) were measured using a BET surface area analyzer and the details of the measurements are given in Table 2.

Table 2. Surface area analysis of the alumina powders by the BET technique.

sample	Particle size in μm	Surface area m^2/g
Aloca alumina A16SG	0.34	10.4
NALCO alumina	1-3	1.337

Surface area of the particles play major role in slurry-based processing techniques as the suspension of the powder in a suitable fluid using a dispersant is a phenomenon dependent on the surface characteristics of the powder. A 30 vol. % slurry of the alumina along with 1.5 wt. % of each of the above said dispersants were made and sedimentation tests were carried out to find the most suitable dispersant. The sedimentation tests give an approximate idea on the best dispersant and powder combination. DARVAN 821A was found to be best dispersing agent for alumina powder from the sedimentation test.
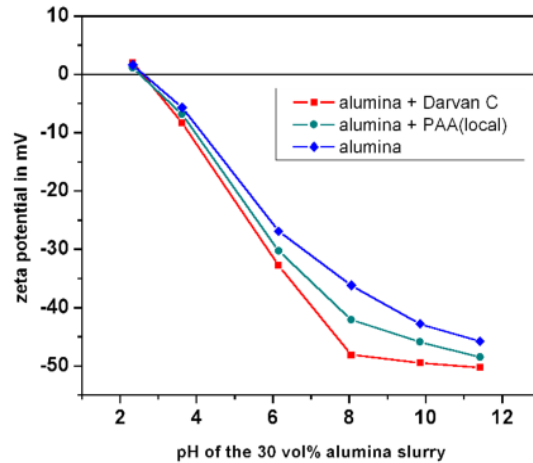
Fig, 5.2. Zeta-potential of alumina slurry as a function of pH with different dispersants.

Zeta potential on the alumina particles with the best dispersant (Fig 5.2), at different pH values was measured to ensure that the pH of the slurry is away from the isoelectric point.

Viscosity of the slurries was also measured using a Brookfield soft solid tester viscometer as shown in Fig 5.3. Fig 5.3 (a) shows the viscosity of the alumina slurry with different concentration of dispersants at a fixed sheer rate. It was noted slurry with 1 wt. % dispersant has minimum

viscosity and the slurry became more viscous by either increasing or decreasing the dispersant content from the optimal value of dispersant. As the dispersant content is increased from zero, more and more particles in the slurry get coated and start dispersing in the slurry, which aid in smooth flow of slurry till it reaches the minimum value of viscosity where all the particles are coated with the dispersant. Further addition of dispersant in the slurry starts entangling the dispersed particles and forms agglomerate, which hinder the flow of slurry and increase the viscosity. Fig. 5.3(b) shows a flow curve of the alumina slurry with solid loading of 55 vol. %., achieved by adding 1 wt. % of DARVAN 821A.

To prepare a highly loaded slurry, alumina powder with dispersant was tumbled along with the premix solution containing monomer and cross-linker, in a homemade tumbler mill in a polyethylene container. Alumina balls of 10mm diameter were used as milling media. The ratio of alumina powder to the milling media was kept at 1:1.5 by weight so as to get a uniform slurry without reducing the particle size. The mixture was tumbled for about 12 hours to get a uniform slurry.

(a)   **(b)**
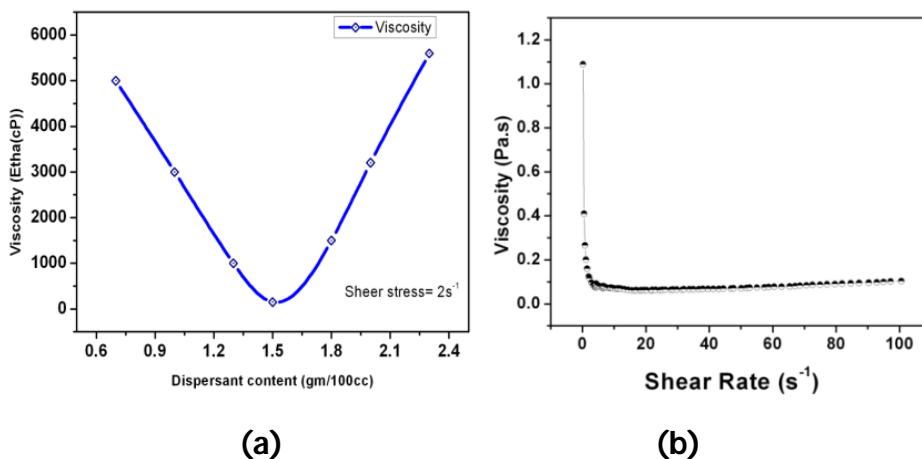
Fig. 5.3. (a) Optimization of dispersant content and **(b)** Viscosity of 55 vol % Alumina slurry with optimal dispersant content.

Air bubbles usually get entrapped in the slurry because of prolonged tumbling. They can, if allowed to remain in the slurry, result in pores and voids in the final product. These trapped air bubbles were removed by de-airing the slurry in a home-made de-airing unit. 0.1ml of APS (10 wt% solution) was used to initiate the polymerization reaction and 0.1 ml of TEMED was used as catalyst to promote controlled polymerization process. The slurry was poured into a mold fabricated using ABS plastic shown in Fig. 5.4, right after the polymerization reaction in the slurry started.

Fig. 5.4. A Mold prepared by ABS plastic to fabricate aerofoils, to demonstrate the possibility of fabrication of a complex-shaped object with thicker and thinner cross-section.

Drying is the one of the most important steps in the gelcasting process as ~50 vol. % solvent, in the present case water; need to be removed from the gelled parts. Non-optimal drying can lead to cracks and distortion as discussed in section 2.5.3 of chapter II. Drying process was optimized in a humidity controlled environment. The samples were dried in high humid atmosphere (~95%) at 50 ^{o}C for 24 hours so that the rate of water removal from the gelled part will be minimal which will give enough time for the polymer network to set and strengthen. Further drying was done in a relatively low humid atmosphere at higher temperatures. It takes nearly 60-70 hours to remove the water completely form the gelled parts.

The next crucial part of gelcasting is removal of organic binders. In the present study the binders are removed by thermal debinding where the dried gelcast green part is heat-treated above the decomposition temperature of binders to expel the binders. The heat-treatment schedule is planned according to the decomposition behavior of the binders. Thermo-Gravimetrical Analysis (TGA) was performed on gelcast performs to get the decomposition temperature of the organic binders used in the present investigation. The TGA plot (shown in Fig 5.5) shows a fast decrease in the weight of the preform up to 400 °C and then onwards a no loss in weight was observed. The debinding schedule for gelcast preforms is as follows, up to 400 °C a slow heating rate of 0.5 °C/min maintained for steady decomposition of binders and then up to 600 °C the rate of heating was increased to 1 °C/min, followed by dwell at 600 °C for 2 hours to complete the removal of binders from the preforms.
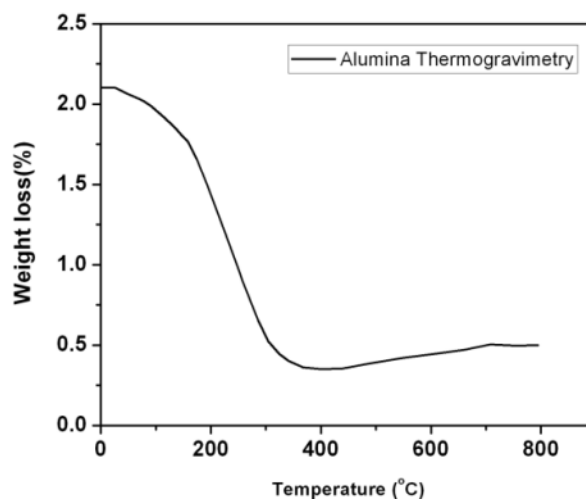
Fig. 5.5. TGA of Gelcast alumina preform shows the binder burn out process is completed at 400 °C.

The debinded samples were sintered at 1680 °C in a Nabertherm furnace, a heating rate of 5 °C/min. was used. After a dwell of 2 h at 1680 °C,

139

the samples were furnace cooled. An SEM micrograph (Fig 5.6) shows a 100% dense alumina sample with no porosity. No crack or pores were seen in the final micrograph.
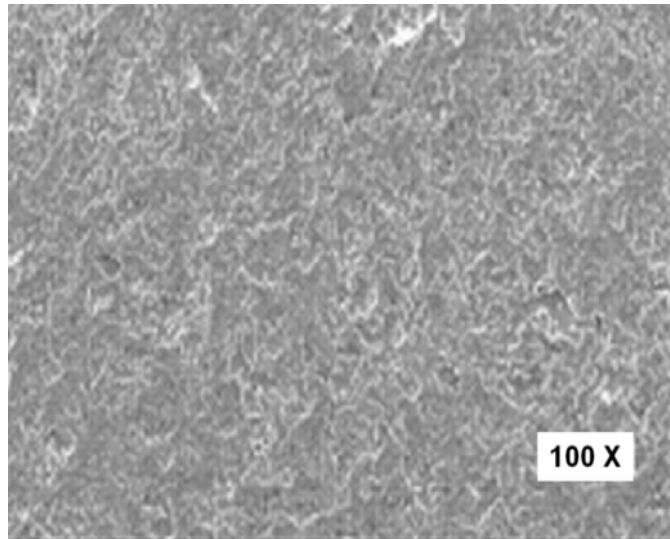
Fig.   5.6. Micrograph of sintered alumina processed through gelcasting rout, showing zero porosity and uniform microstructure.

5.2.2. Rapid prototyping of Al_2O_3

In order to demonstrate the feasibility of making complex ceramic parts out of the gelcasting process, complex molds of wax and plastic fabricated by the rapid prototyping technique. One such mold is shown in Fig 5.4. An **a**erofoil-shaped mold was chosen initially so as to study the parameters affecting the fabrication of complex components with varying thicknesses and curvatures.

A CAD image was developed of the desired mold and fed into a rapid prototyping machine. In the present work, a commercially available Rapid Prototyping machine (STRATASYS-make, Model FDM 3000), using the Fused Deposition Molding method (FDM), was used to fabricate sacrificial moulds having the negative shape of the desired structure. Two types of materials in

wire form were used as feedstock. These were melted and deposited layer-by-layer under computer control, guided by the CAD model fed into the computer. In each pass, a layer of 0.25 mm thickness was deposited. The RPT process is outlined in Fig. 5.7.
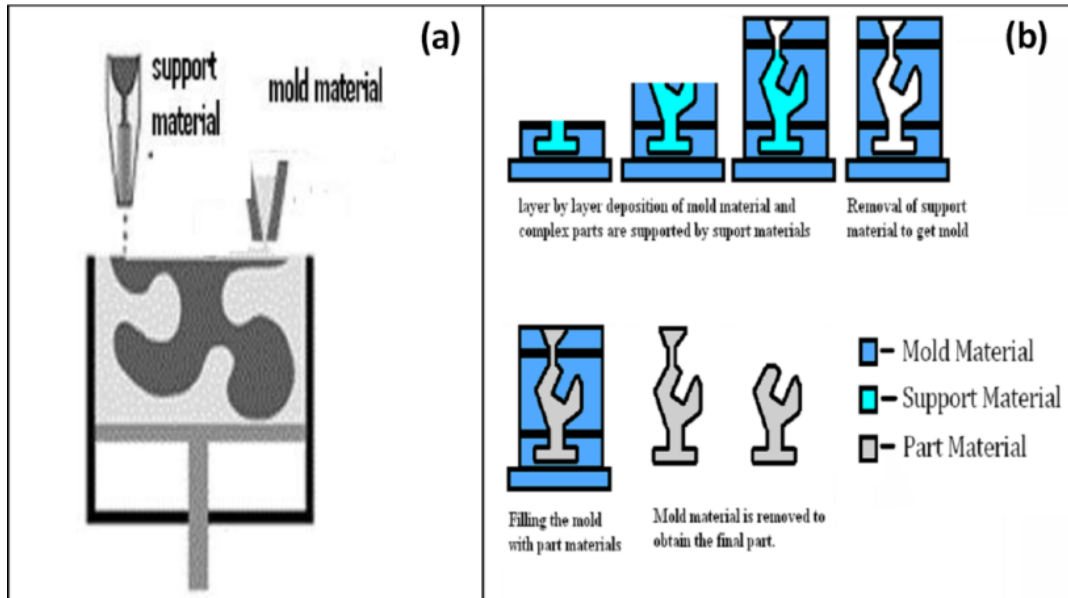
Fig. 5.7. A schematic of mold and final product making process through rapid prototyping method (a) Layer by layer deposition of mold and support material (b) top row shows various stages of RPT to fabricate molds through layer by layer deposition of mold material and support material, support material is deposited in the hollow region to give additional strength. After the mold is fabricated support material is removed and filled with part material.

One of the materials was chosen to be water-soluble and was used to build support structures. The support structures were subsequently removed by leaving the molded part in water, mixed with a proprietary powder material supplied by STRATASYS, under ultrasonic excitation, at 60 °C for several hours, the duration being dependent on the complexity of the internal cavities. After several trials, the mould design was finalized in such a way that it was essentially a shell of plastic with a wire mesh of plastic internally supporting the shell. Fig 5.8(a) shows the CAD model of an object

made in the present study. Fig 5.8(b) shows a CAD picture of the mould showing the final design adopted by us. It consisted of a shell supported by a wire-mesh like structure. Such a design reduced the use of material and also made the dissolution of the mould at a later stage trouble-free. The mould thus prepared was treated to avoid leaks of the highly fluid slurry. Complex alumina parts were then prepared successfully by casting alumina slurry into the mold.
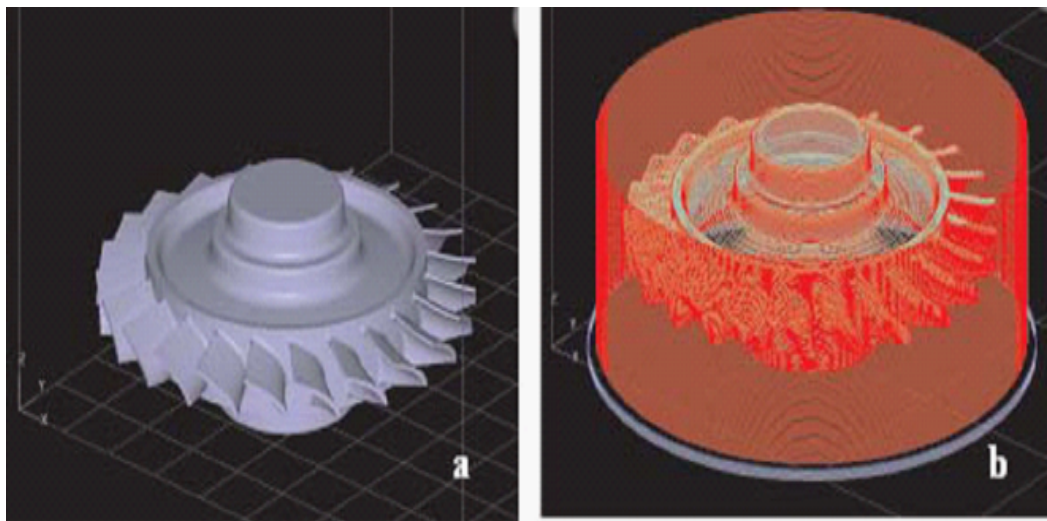
Fig. 5.8. (a) CAD model of a trial rotor **(b)** CAD image of the rotor mold, which was fed to the RPT machine to fabricate molds for rotor .

Highly loaded slurry of alumina was prepared and poured into these RPT mold. As these molds are complex with thick and thin parts, the drying process and drying time was modified. Above all, the mold releasing of these complex parts with intrinsic detail was studied carefully. Different approaches like burning and dissolution of the mold were studied. Debinding and sintering of the green component obtained after the mold removal were done as per the schedule described earlier. Final complex alumina parts fabricated by Gelcasting and RPT were shown in Fig 5.9.

Fig. 5.9. Final complex shaped product fabricated through integrating gelcasting process with Rapid prototyping technique .

5.2.3. Gelcasting of W

After successfully fabricating very complex shaped parts from alumina (Fig.5.9), the gelcasting process was extended to metal powders such as tungsten and stainless steel. The whole exercise of identifying suitable dispersant, optimal dispersant content and modification to gelcasting process, were done to obtain defect free SS, tungsten and tungsten heavy alloy parts (Fig. 5.10).

Fig. 5.10. Tungsten and SS metal products processed through gelcasting technique.

One of the advantages of gelcasting tungsten is the control over final densities and porosity, which can be explored to process porous tungsten parts. A dispenser cathode used in high energy microwave tubes (Fig. 5.11) is one such application where continuous porosity to locate electron emitter compounds is needed in 80% dense tungsten parts.
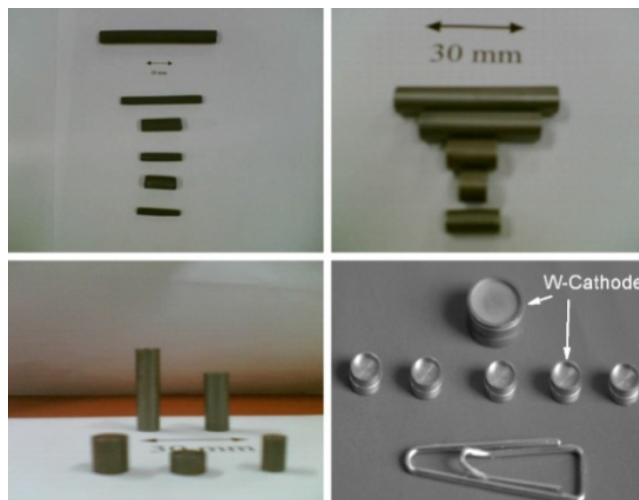
Fig. 5.11. Sintered and machined tungsten rod and tungsten cathodes processed through gelcasting technique.

Gelcasting process could successfully render cathode with desired pore morphology, size distribution and pore density. Fig. 5.12 shows that the final density increases with increase in solid loading in the slurry.
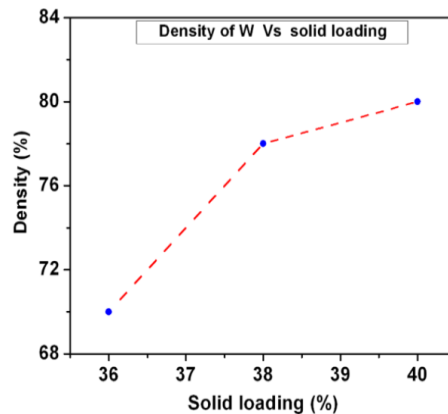
Fig. 5.12. Final density of tungsten is plotted against the solid loading of the slurry it was found that final density increases with increase in solid loading in the slurry.

Fig. 5.13 shows the microstructure of porous tungsten processed through gelcasting technique. No macro-defects were observed at lower magnification of 250 X and at higher magnification of 1000 X. Continuous and uniformly distributed pores of the size 2-5 μm were observed, which is essential for W-cathode applications.

(a)   (b)
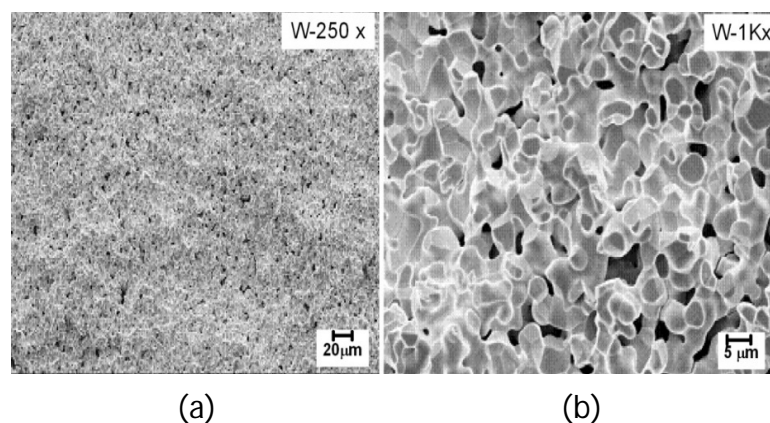
Fig. 5.13. Micrographs obtained on gelcast tungsten in SEM at a magnification of 250X **(a)** shows uniformity in the distribution of fine pores and at 1000X **(b)** continuous pores of 2-5 μm size can be observed.

5.2.4. Larger W-parts through gelcasting

In the previous sections fabrication of complex alumina parts and tungsten rods and cathodes, which are of smaller dimensions, were discussed. In order to explore the ability of gelcasting technque in fabricating larger components, tungsten nose tips for rockets, each weighing around 5-7 kgs were fabricated. After tuning the process parameters, especially the drying stage, tungsten nose tips as shown in **Fig5.14** were fabricated.
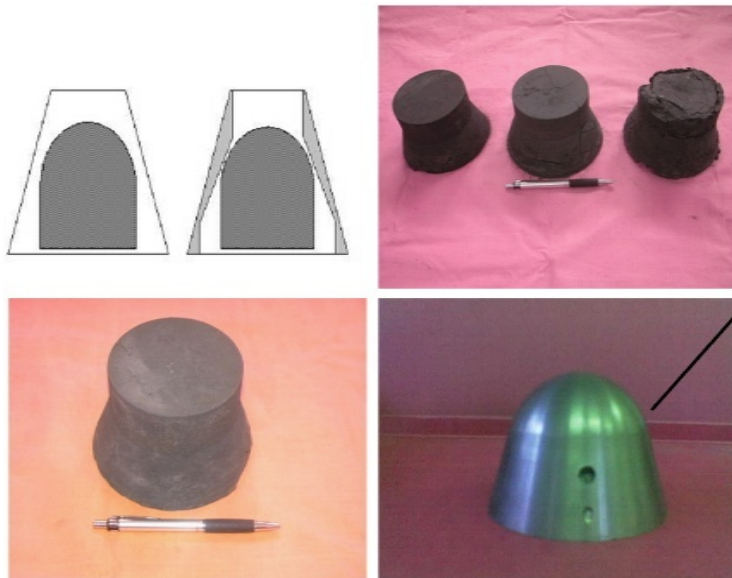
Fig. 5.14. Development of tungsten nose tips used in missiles, to demonstrate the potential of gelcasting technique in fabricating large components.

The gelcasting technique, which was successfully used for the fabrication very complex-shaped components of Al_2O_3 using RPT molds, and for making large and heavy components out of tungsten, was applied to develop a process for the manufacture of YBCO components.

5.3. Gelcasting of YBCO superconductors

In order to explore the possibility of integrating gelcasting with IG process as discussed in the section 5.3, a simple hollow cylinder of Y-211 preform is prepared through gelcasting technique and then subjected to IG

processing to get superconducting YBCO cylinder as product. The curved surface with hollow regions inside cylinder will be sufficient to demonstrate the credibility of the present approach.

5.3.1. Fabrication of YBCO cylinder

A YBCO cylinder was fabricated starting with a Y-211 preform produced using the gelcasting process. Y-211 powder was produced through the citrate synthesis technique, as discussed in section 2.1.1 of chapter II. The particle size was ~ 1 -2 μm. Methacrylamide (MAM) and methylene bisacrylamide (MBAM) were used as monomer and cross linker respectively in the present work. An aqueous premix solution containing 16 wt.% of MAM and MBAM (in 6:1 weight ratio) was prepared and aged for 12 hours. Weighed amount of Y-211 powder along with 1.5 wt. % dispersant (Dolapix 77) was added to the premix solution. Then the mixture was tumbled in a polyethylene container for 12 - 16 hours at varying speeds employing a home-made tumbling machine. Zirconia balls of 10 mm diameter were used for homogenous mixing. The slurry of Y-211 was degassed in a vacuum unit to remove air bubbles. 0.1 ml of 10 wt. % Ammonium peroxydisulfate (APS) and N,N,N,N-tetramethylethylenediamine (TEMED) solutions were added to the slurry, just before casting the slurry into a mold as initiator and as catalyst respectively. The part was dried carefully, and the organic binders were removed by controlled thermal debinding process. A detailed discussion of the fabrication of Y-211 slurry can be found in Section 3.2 of chapter III.

The dried Y-211 preform thus obtained by gelcasting route was pre-sintered at 950 ºC for 4 hours, prior to infiltration. The pre-sintered Y-211 preform thus obtained was subjected to IG process. Y-123 was used as source

of liquid phases ($BaCuO_2$ and CuO) in the present experiment. The ratio Y-123:Y-211 was maintained as 2:1 by weight.
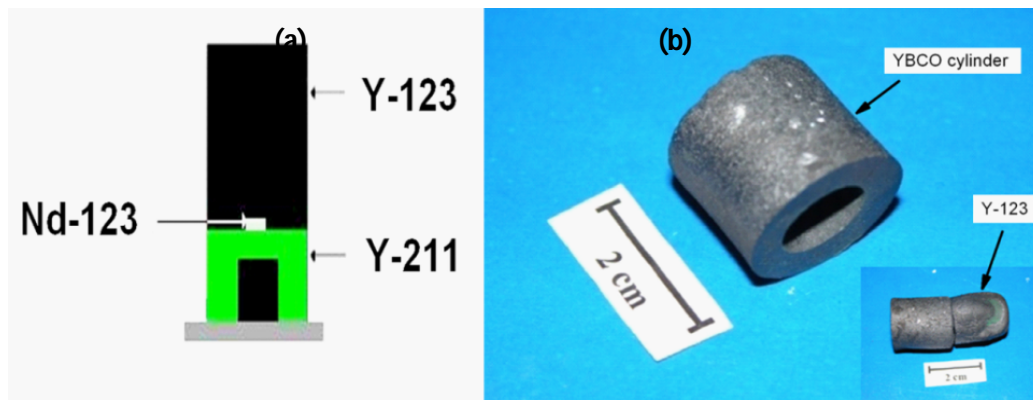
Fig. 5.15. (a) A schematic of experimental arrangement for fabricating YBCO cylinder is shown. Y-123 pallet is used as liquid source for the Y-211 cylinder. Nd-123 seed is places in between Y-123 pallet and Y-211 cylinder for texturing and **(b)** YBCO cylinder processed through IGP by using Y-211 cylinder, fabricated through gelcasting technique, as preform.

A schematic sketch showing the sample assembly used for the fabrication of a YBCO cylinder is shown in Fig5.15. Nd-123 seed was used to promote the textured growth of Y-123 during the IG process. The assembly was heat-treated in a tubular furnace following a heat-treatment schedule described elsewhere. Fig 5.15 shows the YBCO cylinder obtained as above.

5.3.2. T_c and $J_c(H)$ of YBCO cylinder

Thin sections were sliced from the IG processed YBCO cylinder using a low speed saw for various studies. Temperature dependence of electrical resistivity (ρ) was measured employing the four probe techniques to determine the critical temperature (T_c) and transition width (ΔT_c) as discussed in section 2.6 of Chapter II.

The temperature dependence of dc electrical resistivity carried out on the sample showed a sharp superconducting transition as shown in Fig. 5.16

indicating the high quality of the sample. The onset of T_c was observed to be ~ 92.9 K and the sample showed a transition width ΔT_c < 1 K indicating that there are no major oxygen deficient regions/solid solutions. The sharp transition confirms that the process followed has efficiently removed the chemicals used in gelcasting.
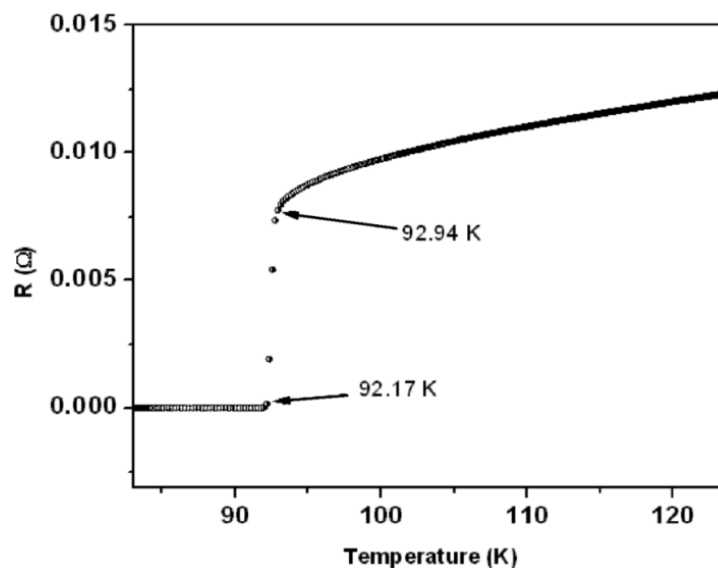
Fig. 5.16. A plot of showing DC electrical resistivity as a function of temperature of YBCO cylinder produced through gelcasting technique. A sharp transition (T_c) at 92 K with a narrow transition width (ΔT_c) ~0.6 K indicates absence of low T_c phases.

A typical micrograph obtained using SEM operating in secondary electron detection mode is shown in Fig 5.17. It can be observed that the sample is nearly free from major macro-defects like cracks, pores etc. It can be observed from Fig 5.17 that the Y-211 particles are uniformly distributed in Y-123 matrix. A histogram constructed from the micrograph indicating the particle size distribution is shown in Fig 5.17.

(a)   (b)
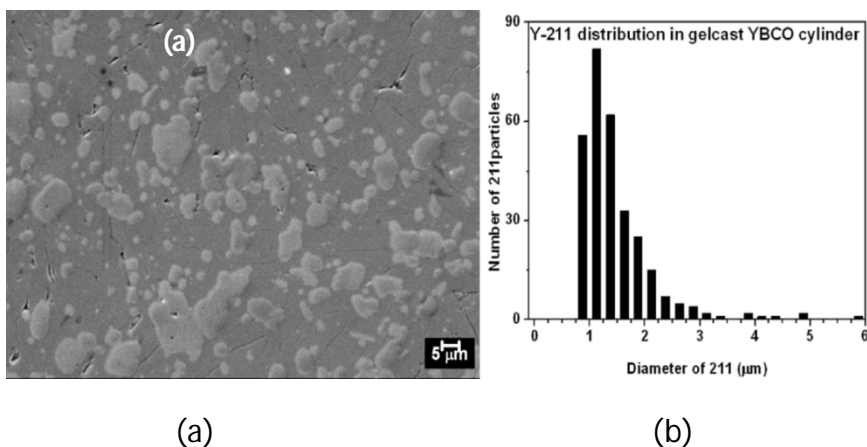
Fig. 5.17. (a) Micrograph of gelcast YBCO cylinder obtained form SEM at a magnification of 2000 X . The micrograph shows Y-211 particles in Y-123 matrix without any reaction as observed in case of CeO_2, ZrO_2 doped YBCO samples (Fig. 3.19 and Fig. 3.22) **(b)** Histogram obtained on the micrograph shows that most of the particles are below 2μm.

It is evident from the micrograph and histogram that the Y-211 particle size distribution is centered around 1.5 μm. However, a few large particles (larger than 10μm) can also be seen.

Magnetic hysteresis (M-H) loops were recorded at 50 K and at 77 K in specimens extracted from the sample, by varying the magnetic field H up to 10 T and 14 T respectively, using PPMS. The M-H loops recorded from the sample at 50 K and 77 K are shown in Fig 5.18 and Fig 19. The field dependence of current density obtained in the sample at 50 K is shown in Fig 5.18. It is evident that the sample shows nearly flat $J_c(H)$ response to fields as high as 14 T. The sample showed a $J_c(0)$ of ~11 kA cm^{-2} at 50 K. The sample showed a peak field H_p at 5 T at 50 K. It can also be seen that the loops are open to fields up to14 T at 50 K. We note that no grain refiners such as platinum have been used in this work.
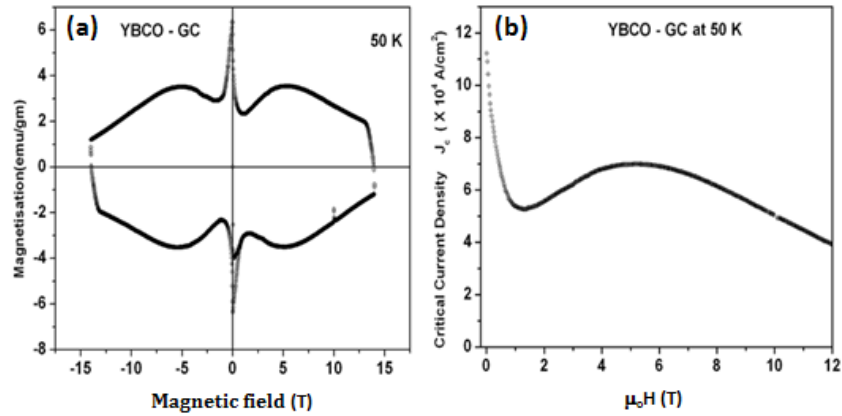
Fig. 5.18. (a) magnetic hysteresis loop for YBCO cylinder at 50 k and **(b)** critical current density calculated using bean's critical state model showing J_c higher than 10^4 A/cm^2 up to 12 T of applied field.

The sample showed a $J_c(0)$ of 2 kA cm^{-2} at 77 K. The sample showed a peak field H_p, (defined as the field where the slope of M versus H curve changes), of 1 T at 77 K. It can also be seen that the loops are open to fields as high as 5 T at 77 K establishing the high irreversible nature of the sample. The sample was found to possess irreversibility field larger than 3.5 T at 77 K. J_c of the present sample up to high fields are found to be interesting from the view point of engineering applications with complex geometry.
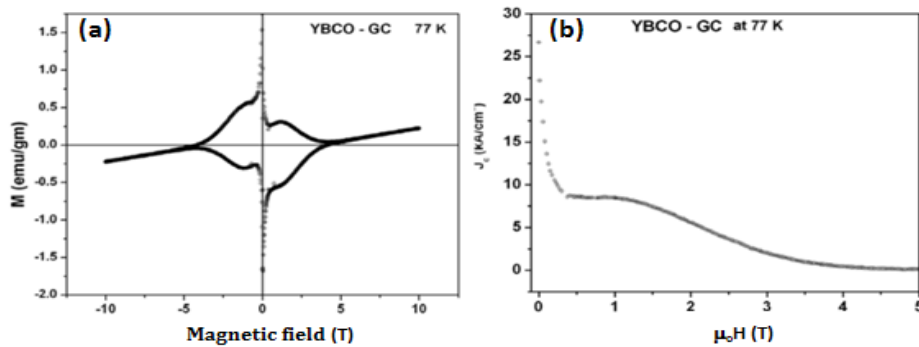
Fig. 5.19. (a) Magnetic hysteresis loop for YBCO cylinder at 77 K and **(b)** critical current density calculated using Bean's critical state model showing J_c up to 3 T of applied field.

5.4. Conclusions

The versatile shape forming technique applied to various ceramic materials, viz. gelcasting has been extended to the fabrication of bulk YBCO components possessing a microstructure that supports high current densities. This was accomplished by fabricating the preform of Y-211 used in Infiltration Growth processing by the gelcasting technique. Y-211 could be processed in an aqueous environment because of its lack of reactivity with water. The efficacy of the process was demonstrated by the fabrication of a hollow cylinder. The cylinder was characterized by microstructural and magnetic measurements. The microstructure is similar to that typically observed in melt or IG processed materials. The observed current density is good enough for many applications, say for use of the material as magnetic shields. Further improvement in J_c might be possible through refinement of the process, like addition of Pt or CeO_2 to make the Y-211 further divided, devising methods to pack the Y-211 denser in the Y-123 matrix etc. Another possibility is the introduction of nanoparticles of non-reactive phases into the Y-123 matrix by the NDSC process. It is also important that the process can be carried out using molds fabricated by the Rapid Prototyping technique, which makes it possible to prepare high J_c YBCO in shapes hitherto not possible.

Reference

[1]   J. O. Willis, M. E. McHenry, M. P. Maley, and H. Sheinberg, *IEEE transactions on magnetics*, **25** (1989) 2

[2]   Mathias Noe and Michael Steurer, *Supercond. Sci. Technol* **20**. (2007) R15–R29

[3]   W. K. Chu, K. B. Ma, C. K. McMichael and M. A. Lamb, *Applied Superconductivity* **1(7-9)** (1993) 1259-1264

[4]   H. Teshima, M Tanaka, k. Miyamoto, K. Nohguchi and K. Hinata, *Physica C* **74** (1997)17-23

[5]   S. Ohshima, T. Ogasawara and K. Ehata *IEEE transactions on applied superconductivity*, **7(2)** (1997) 3060-3063

[6]   H. B. Bever (Ed.), *Encyclopedia of Materials Science and Engineering*, Pergamon Press, Oxford **1** (1986) 707–711

[7]   Hans T. Larker and Robert Lundberg, *Journal of the European Ceramic Society* **19** (1999) 2367-2373

[8]   C. Falamaki and M. Beyhaghi, *Materials Science-Poland*, **27(2)** (2009) 427-441

[9]   B. C. Mutsuddy and R. G. Ford, "*Ceramic Injection molding*", Springer, (1994)

[10]   A. C. Young, O. O. Omatete, M. A. Janney and P. A. Menchhofer. *J Am Ceram Soc* **74(3)** (1991) 612-618

[11]   L. J. Vandeperre, A. M. De Wilde and J. Luyten, *Journal of Materials Processing Technology* **135** (2003) 312–316

[12]   Mark A. Janney, Ogbemi O. Omatete, Claudia A. Walls, Stephen D. Nunn, Randy J. Ogle, and Gary Westmoreland, , *J. Am. Ceram. Soc.*, **81 (3)** (1998) 581–591

[13]   Tsuru, Sangkyun Kang, Alexander G. Cooper, Alexander Nickel and Fritz B. Prinz, *Materials Science and Engineering* **A334** (2002) 187–192

[14]   Isabel Santacruz, M   Isabel Nieto and Rodrigo Moreno, *Ceramics International* **31** (2005) 439–445

[15]   T. Rajasekharan, P. M. Swaroop Raju, Rakesh Kumar Pandey, V. Seshu Bai, R. Pradyumna and M. A. H. Baig, *Metals Materials and Processes*, **19(1-2)** (2007) 41-46

[16]   T. H. Johansen, M. R. Koblischka, H. Bratsberg and P. O. Hetland, *Phys. Rev. B* **56** (1997) 11273

Chapter-VI

Summary and Conclusions

The present thesis discuses the introduction of nanoparticles of ceria, zirconia and Ba-Ce-O into Infiltration Growth processed YBCO superconductor composites and its effect on the final microstructure and superconducting properties.

A method is developed for the introduction of nanoparticles separate from one another and without agglomeration into the Y-211 preforms used for IG processing. A certain amount of reaction between the preform and the nanoparticles keeps the particles anchored to the Y-211 grains during the infiltration of liquid phases and further texturing stages. Using the Infiltration Growth process, and introducing the nanoparticles as separate entities into the preform, has the advantage that the agglomeration and flow-tracks formed by accumulated particles due to their movement along with liquid phases can be avoided: such tracks have been reported in melt growth experiments [1].

The main motivation for the above work is the reported observation that very high current densities can be obtained in melt processed samples containing large concentrations of nanometer-sized additives. For instance, the best current densities reported till today in any superconductor bulk has been in the melt processed NEG-123 with 35mol. % of nanometer-sized (70 nm) Gd-211 and 0.1 mol. % of nanometer-sized NbO_3 it showed a zero filed current density of ~600 kA/cm^2 , and a current density of ~200 kA/cm^2 at 4 T [2].

IG process offers advantages of near net shape processing. The process used in the present thesis to disperse nanoparticles in Y-211 preforms, starting with a colloidal solution of the required nano-material and mixing it intimately into a stable Y-211 slurry, has the advantage that it can be combined with the gelcasting process developed in this study. The gelcasting process involves the preparation of a stable suspension of the Y-211 powder using a suitable dispersant in water, along with small amount monomer and cross liners. The dispersant was identified in the present study. The slurry is set in a mould. The mould can be fabricated by the rapid prototyping technique which can potentially allow the formation of extremely complex-shaped superconductor components, if needed. The preform of Y-211 thus prepared is dried, debinded and sintered. It is used in IGP to make superconductor parts with a microstructure that supports high current densities. We have demonstrated the fabrication of a superconductor hollow cylinder by the gelcasting process and have studied its microstructure, and have measured the current densities supported by it.

The NDSC process developed for the introduction of nanoparticles separate from one another and without agglomeration into the Y-211 preforms has the potential to yield high current densities in IG processed samples, just as it was obtained in the melt processed samples. However, the nano-materials that we worked with did not help increasing the current density much due to a variety of reasons. A basic problem observed was the lowering of T_c of the Y-123 material by the dissolution of the additives in the Y-123 phase. There were earlier reports of such lowering of T_c [3], and we have confirmed that it occurred in our materials by measurements of electrical resistivity and ac magnetic susceptibility as function of temperature. Another problem was the enormous grain growth of the Y-211

grains in the preforms in most cases, even at low levels of doping. The particle size refinement due to the added material was not sufficient in most cases to reverse this large grain growth and the J_c s observed in those materials were very low. An added effect was the reduction in continuous porosity in the Y-211 preform due to the reactivity of the nano-materials with the Y-211 grains of the preform resulting in Y-211 grain growth. This would affect the liquid phase inflow into the preforms for IGP.

An exception was ceria-doped Y-123. The reaction of ceria with Y-211 preform material was minimal at low concentrations, in the Ce-2 sample. At high concentrations, in the Ce-10 sample, the ceria particles sintered together to form nano-rods. The grain growth Y-211 in the preforms of ceria-added Y-211 was therefore low. Easy infiltration of liquid phases into the preforms was facilitated by the porosity available in their preforms; in the case of the Ce-10 sample, the nano-rods separated the individual Y-211 grains. As a result, the microstructures obtained in those materials, especially in the Ce-10 sample, were very attractive. The IG process, without any doping, inherently gives substantial grain refinement in comparison with the melt growth process; the addition of ceria in IGP lowers the Y-211 grain size even further and narrows the particle size distribution (Fig. 3.12 in Chapter III, reproduced below as Fig. 6.1). The average Y-211 particle size is around 500 nanometers, which we believe is unprecedented.

The current density recorded in the Ce-10 sample decreases only slowly as a function of the applied magnetic field up to 9 T. This is just as in the POIGP (Ce-0) sample; i. e. in a sample prepared from optimized Y-211 preforms just as in the present case, but without the additives [4].
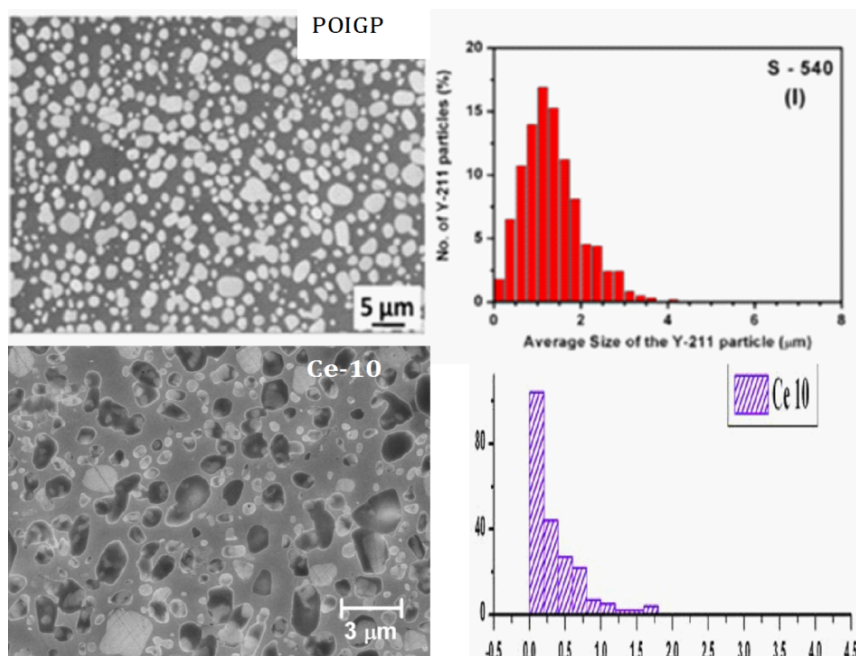
Fig. 6.1. The Y-211 size distribution in the Ce-10 sample is below 0.5 μm (bottom row), whereas the Y-211 particles in the Ce-0 sample are sized around 1 μm (top row).

The reasons for the observed high current density to high fields in the Ce-0 sample occur in the Ce-10 sample as well; there is extensive nano-twinning [5] in the Ce-10 sample, and the Y-211 grain size is even smaller (see Fig.6.1). But the observed J_c values are lower in the Ce-10 sample in comparison with the Ce-0 sample (Fig. 6.2). This can be attributed to the dissolution of ceria in the Y-123 matrix and the associated lowering of T_c. We have studied the flux entry into the Ce-2 and Ce-10 materials as function of the applied dc field using an ac field of varying amplitude as the probe: we have correlated the observations to the content of lower T_c phases.

158
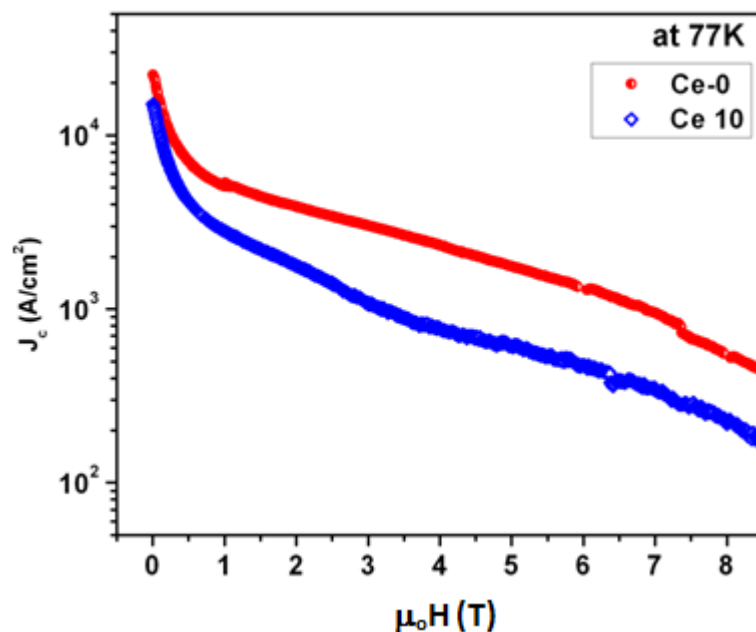
Fig.6.2. Critical currents in both Ce-0 and Ce-10 are sustained up to 9 T due to extensive twinning. But in case of Ce-10 the magnitude of the Jc is lower when compared with Ce-0.

We can also conclude from the above study that Y-211 particle size refinement, though attractive, if brought about by a nano-material that interacts with the matrix and lowers T_c, the benefits to improvement of the current carrying capacity of the material would be limited.

The refinement of the Y-211 particle size in melt processed Y-123 through the introduction of dopants such as Pt, ceria, barium cerate and zirconia has been a matter of intense study. The NDSC process developed in this work enables the deposition of nanoparticles separately without agglomeration on the Y-211 particle surface in the preform, and this enables the study of the reaction taking place between various components of the reaction system more clearly. We observe that the particle size refinement takes place because of the ability of the above materials to draw Ba from the Y-211 material [6]. Other work in the literature also has pointed out that the

reactivity of the above dopants to form stable compounds with Ba is behind the particle size refinement [7-9]. The chemical reactions involved are as follows.

$$Y_2BaCuO_5 + CeO_2 \rightarrow BaCeO_3 + Y_2O_3$$

$$Y_2BaCuO_5 + ZrO_2 \rightarrow BaZrO_3 + Y_2O_3$$

$$2YBa_2Cu_3O_{7-\delta} + 2PtO_2 \rightarrow Ba_4CuPt_2O_4 + Y_2O_3 + 5CuO$$
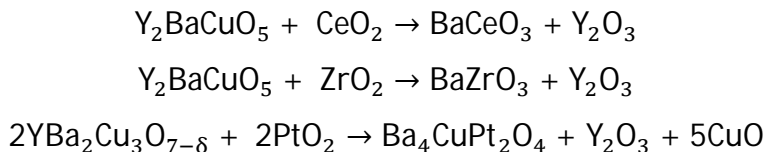
Withdrawal of Ba from regions where the nanoparticles are attached forms one or more Y-rich regions within the Y-211 grains. The regions of the Y-211 grains which have not thus become Y-rich react with the liquid phases and develop necks (Fig.3.16 and Fig. 3.27) which can break in cases where the reaction continues. This accounts for the particle size reduction of Y-211 in the presence of the reactive additives like the ones mentioned above. The particles that are residual in the Y-123 matrix after IG processing are mostly Y-rich compositions of the Y-Ba-Cu-O system. In the samples to which ceria nanoparticles were added, there are also very fine, $BaCeO_3$ particles, with sizes in a few tens of nanometers, which originated from the added ceria nanoparticles.

In the case of samples with Zirconia and Ba-Ce-O nanoparticles, the influence on microstructure and on the field dependence of current density by even small amounts of the dopants was very dramatic. With only 0.1 wt. % Ba-Ce-O added, the microstructure of the IG processed material resembled that of a sintered material and the J_c values were very small. But increasing the amounts of the dopants refined the Y-211 size, restored the typical melt processed microstructure, and the J_c (H) improved. This could be attributed to the grain growth of Y-211 in the preform even with small amounts of additives and the effect of more of the additives in refining the Y-211 by

particle division. We have also seen, especially in the case of the Zirconia – doped samples, that the increased grain growth of Y-211 particles in the preform, even with small amounts of the additive, could become a problem in IGP because the continuous porosity needed to allow the infiltration of liquid phases could get closed leading to samples of very poor microstructure and J_c.

References

1. T. Meignan, A. Banerjee, J. Fultz and P. J. McGinn, *Physica C* **281** (1997) 109-120

2. M. Muralidhar, N. Sakai, M. Jirsa, M. Murakami and I. Hirabayashi, *Appl. Phys. Lett.* **92** (2008) 162512

3. I. Monot , K. Verbist, M. Hervieu, P. Laffez, M. P. Delamare, J. Wang, G.Desgardin, G.Van Tendeloo, *Physica C* **274** (1997) 253-266

4. N. Devendra Kumar, T. Rajasekharan, K. Muraleedharan, A. Banerjee and V. Seshubai, *Supercond. Sci. Technol.* **23** (2010) 105020

5. N. Devendra Kumar, T. Rajasekharan, Ravi C. Gundakaram, and Vummethala Seshubai, *IEEE transactions on applied superconductivity* **21** (2011) 3612-3619

6. Chan-Joong Kim and Gye-Won Hong, *Supercond. Sci. Technol.* **12** (1999) R27–R41

7. M. Yoshida, A. Tsuzuk and I. Hirabayashi, *Proc. Int. Workshop on Superconductivity (Honolulu, HI, 1992)* p 270

8. C. J. Kim, H. C. Moon, K. B. Kim, S. C. Kwon, D. S. Surh, I. S. Suh and D. Y. Won, *Mater. Sci. Lett* **11** (1992) 831

9. Chan-Joong Kimy, Ki-Baik Kimy, Hai-Woong Parky, Tae-Hyun Sungz, II-Hyun Kuky and Gye-Won Hongy, *Supercond. Sci. Technol* **9** (1996) 76–87

Figure Captions

Chapter-I

after a hold of 20 minutes, showing Gd-211 particles in liquid. In samples containing (a) 0 (b) 10 (c) 20 (d) 30 and (e) 40 mol% Y-211 added to Y-123, we observe that the Y-211 particles become finer, denser in distribution and spherical in morphology, with increasing Y-211 concentration [31].

Chapter II

Chapter-III

wt% of various dispersants. The suspension was kept for 12 hours to examine the sedimentation rate of the Y-211 particles, for preliminary optimization of dispersants. Y-211 particles remain suspended in the slurry with DOLAPIX 77, whereas with other dispersants the particles have either settled down, or reacted with the dopant as in the sample marked A 88. The good suspension observed with DOLAPIX 77 was sufficient to ensure the completion of the process of nanoparticle introduction without segregation, which required that the slurry is stable for about an hour after mixing.

magnification of 50,000 X, very fine individual nanoparticles of ZrO_2 can be seen on Y-211 particles. Both the microstructures confirm strong interaction of ZrO_2 with Y-211 and cause fusing of Y-211 particles.

Y_2O_3 particles within a Y-211 particle and on the right is a magnified image showing one of the particles within the Y-211 background. (b) High temperature X-ray diffractograms obtained from Y-211 with CeO_2 [32] shows the formation of Y_2O_3 and $BaCeO_3$. These observations led Vilalta et al. [32] to conclude that the fine Y-211 formed during melt growth of Y-123 are those nucleating on nanometer-sized Y_2O_3 formed during the decomposition of Y-211 in the presence of ceria.

Fig. 3.23. ZrO$_2$ nanoparticles are seen individually deposited on the Y-211 grains in a preform of Y-211 heat-treated for 4 h at 950 ^{o}C. The nanoparticles appear to have reacted to a certain extent with the Y-211 grains. They are, therefore firmly adherent on the Y-211 surface and are unlikely to be dislodged during the infiltration of liquid phases. We also observe that the the Y-211 particles have fused into large grains. **102**

Fig. 3.24. The microstructure (as obtained by FE-SEM) of IG process YBCO containing 2, 5, and 10 wt. % ZrO$_2$ nanoparticles introduced by the NDSC procedure. As low concentrations of ZrO$_2$, the grains of 211 which had grown considerably at the preform fabrication stage have been substantially refined, though the particle size is still more than 1 µm. The 211 grain growth could not be offset in the other two samples, and the IG processed samples have very large Y-211 grains. In the 10 wt. % sample, the 211 size has lowered in comparison with the 5 wt. % sample due to the refinement due to large amount of ZrO$_2$ available. The unreacted excess of ZrO$_2$ nanoparticles of size around 30 nm are found to be segregated in the micrograph. **103**

Fig. 3.25. FE-SEM image from the Y-211 preform containing 10 wt. % of Ba-Ce-O nanoparticles. The particles are distributed separate from one another. They have reacted with the preform, and the Y-211particles of the preform have fused together to a large extent. **104**

Fig. 3.26. FE-SEM images from IG process samples containing various amounts of Ba-Ce-O nanoparticles.(a) In the sample with the smallest Ba-Ce-O content, viz. 0.1 wt. % Ba-Ce-O, formation of the the usual long parallel platelets of Y-123 characteristic of melt processed and IG processed samples have been disturbed by the grain growth of Y-211. In (b), (c) and (d), with 0.5 wt. %, 3.0 wt. % and 10.0 wt. % of Ba-Ce-O respectively, we see that the Y-211 particle size decreases continuously with increasing Ba-Ce-O content. The parallel, long Y-123 grains have been restored in the samples with higher Ba-Ce-O content. **105**

Fig. 3.27. An enlarged image from the YBCO sample with 10 wt. % of Ba-Ce-O. Y-rich cores can be observed in the Y-211 grains. Particles in different stages of division can be seen. Small white BaCeO$_3$ particles can be seen. **106**

Chapter IV

infiltration of liquid phase from Y-123 into the Y-211 perform, can be observed. (d) and (e), which show the side and top view respectively of the Ce-5 sample demonstrates the fact that the Y-123 pellet had not shrunk after the experiment suggesting that the entry of liquid phases into the Y-211 perform was blocked in this case.

to Y-211.

Chapter-V

Chapter-VI

Table Captions

Properties and Applications of Superconductors

1. **Properties of Superconductor:**

a) **Zero resistance** [1]**:** No resistance is detectable below a critical temperature (T_c) even for high scattering rates of conduction electrons. Persistent currents magnetically induced in a coil of $Nb_{0.75}Zr_{0.25}$ and watched with NMR yielded an estimate of the decay time greater than 10^5 years! (From theoretical estimates the decay time may be as large as 10^{10} years)
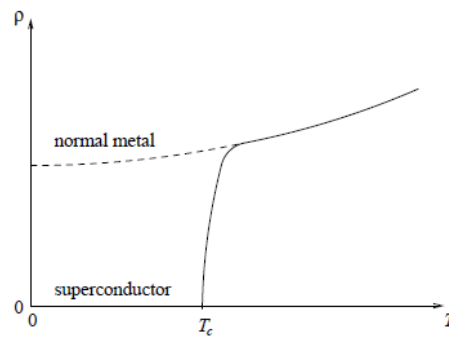
Fig. 1. A temperature dependent resistivity curve showing the disappearance of electrical resistivity below T_c for superconductor.

b) **Absence of thermoelectric effects** [2]**:** No Seebeck voltage, no Peltier heat, no Thomson heat is detectable.

c) **Ideal diamagnetism:** $\chi_m = -1$. Weak magnetic fields are completely screened from the bulk of a superconductor.

d) **Meissner effect** [3]**:** It is found that when a superconductor is cooled in presence of a weak magnetic field below T_c, the field is completely expelled from the bulk of the superconductor.

$$T > T_c \qquad\qquad T < T_c$$
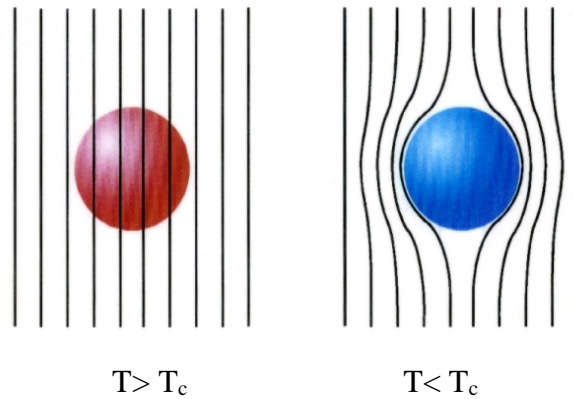
Fig. 2. In superconducting state magnetic flux cannot enter into the superconductors. It exhibits perfect diamagnetism

e) **Flux quantization** [4]**:** The magnetic flux through a superconducting ring is quantized and constant in time. This phenomenon was theoretically predicted by F. London in 1950 and experimentally verified in 1961.
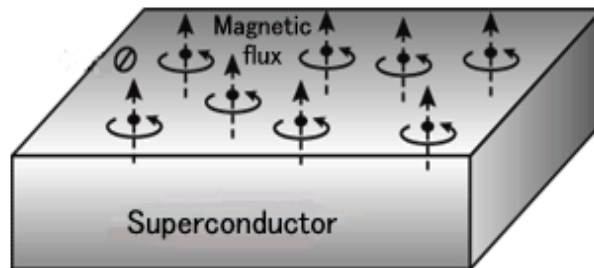
Fig. 3. Magnetic flux (a batch of magnetism) that flows through the ring of superconductor is an integral multiple of the minimum unit (flux quantum). This phenomenon is called the quantization of magnetic flux

f) **Josephson Effect** [5]**:** In 1962**,** Josephson predicted that Cooper pairs can tunnel through a thin non-superconducting barrier without any applied voltage. Anderson and Rowel provided experimental support such phenomenon. Such Junctions are known as Josephson junctions that exhibit macroscopic quantum effects. Josephson junctions have important applications in quantum-mechanical circuits, such as SQUID,

superconducting qubits, and RSFQ (rapid single flux quantum) digital electronics.
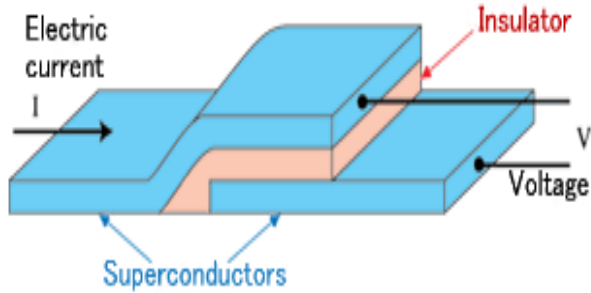
Fig. 4. When a thin layer of insulator is sandwiched between two superconductors, until the current becomes certain volume, electrons pass through the insulator as if it does not exists.

2. Types of Superconductors

Superconductors, based on their magnetic properties, can be broadly classified into two kinds namely Type-I and Type-II superconductors. A typical sketch representing the variation of magnetization of a Type-I superconductor with applied field H_e is shown in Fig. 5(a). When the external magnetic field H_e is lower than the critical field H_c, the magnetization is given by $M = -H_e$ and the superconductor shows a perfect diamagnetism (B = 0). This state is known as the Meissner state.

In the case of a Type-II superconductor, the perfect diamagnetism is maintained only up to the lower critical field, H_{c1}, and then the magnetization varies continuously with the penetration of magnetic flux as shown in Fig. 5(b) until the diamagnetism disappears at the upper critical field, H_{c2}, where the normal state starts.
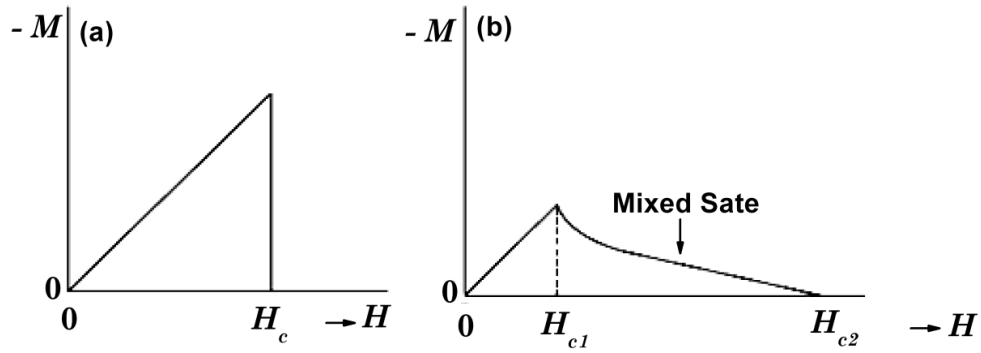
Fig. 5. Field dependence of magnetization (M) for (**a**) Type-I superconductor and (**b**) Type-II superconductor

It is known that the critical field of Type-I superconductors varies with temperature according to

$$H_c(T) = H_c(0)\left[1 - \left(\frac{T}{T_c}\right)^2\right] \dots\dots (A.3)$$

where $H_c(0)$ is the absolute critical field (value of H_c at zero temperature)

Both the lower and upper critical fields (H_{c1} and H_{c2}) of Type-II superconductors show similar temperature dependences. Schematic representations of the H-T phase diagrams of Type-I and Type-II superconductors, indicating the variation of H_c with temperature T, are shown in Figs. 6(a) and (b) respectively.
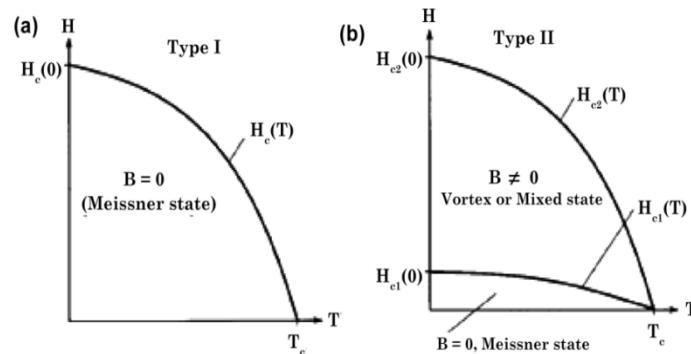
Fig. 6. Schematic representation of H-T phase diagram of (**a**) Type-I and (**b**) Type- II superconductors.

3. Basic theories in superconductivity:

London's Theory:

In 1935, F. and H. London proposed a phenomenological theory for the electrodynamic properties of superconductors. It is based on a two-fluid picture: If the electrons from a normal fluid of concentration n_n and a superfluid of concentration n_s, where $n_n + n_s = n$
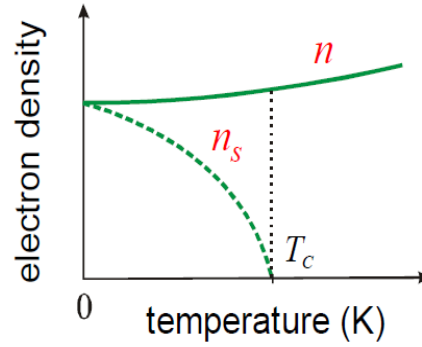
Fig. 7. The variation of concentration of normal and superconducting electrons with temperature.

From Drude model for normal metal

$$m\frac{d\vec{v}}{dt} = e\vec{E} - m\frac{\vec{v}}{\tau}$$

where $\vec{v}$ is drift velocity and τ is the relaxation time

In superconducting state $\tau \to \infty$

$$m\frac{d\vec{v}}{dt} = e\vec{E}$$

$$\frac{d\vec{v_s}}{dt} = \frac{e\vec{E}}{m}, \implies \frac{d\vec{J_s}}{dt} = ne\frac{d\vec{v_s}}{dt} = \frac{n_s e^2}{m}\vec{E} = \frac{1}{\Lambda}\vec{E} \quad \text{-- London's equation}$$

$$\text{Where,} \quad \Lambda = \frac{m}{n_s e^2} = \frac{4\pi\lambda_L^2}{c^2}$$

$$\lambda_L = \left(\frac{mc^2}{4\pi n_s e^2}\right) \text{ is known as London penetration depth}$$

Further from Maxwell's equation

$$\vec{\nabla} \times \vec{H} = \frac{4\pi}{c}\vec{j}$$

$$\Rightarrow \frac{4\pi}{c}\vec{\nabla} \times \vec{j} = -\frac{1}{c\Lambda}\frac{4\pi}{c}\vec{H} = -\frac{1}{\lambda_L^2}\vec{H}$$

$$\Rightarrow \vec{\nabla} \times \vec{\nabla} \times \vec{H} = -\nabla^2\vec{H} = -\frac{1}{\lambda_L^2}\vec{H}$$

Similarly equation also holds for $\vec{E}$ also

$$\nabla^2\vec{E} = \frac{1}{\lambda_L^2}\vec{E}$$

Hence, both electric ($\vec{E}$) and magnetic ($\vec{H}$) field penetrate inside a superconductor to the distance λ_L which is called magnetic filed London penetration depth.
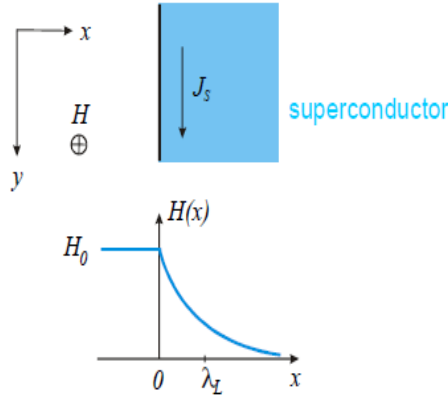
Fig. 8. Magnetic field penetrates into the superconducting sample up to a distance of λ_L gradually disappears as it penetrates further. ($\vec{H} \to 0$ as $x \to \infty$) [].

$$\nabla^2\vec{H} = \frac{1}{\lambda_L^2}\vec{H}$$

With $\vec{H} = (0,0,H_o)$ gives $\qquad \frac{d^2}{dx^2}H - \frac{1}{\lambda_L^2}H = 0$

Using boundary conditions, $H(0) = H_o$ and $H(\infty) = 0$, we get

$$H(x) = H_0 \exp^{\left(-\frac{x}{\lambda_L}\right)} \qquad \text{for the magntic field}$$

Relation to screening current

$$\vec{J_s} = \frac{c}{4\pi} \vec{\nabla} \times \vec{H}$$

$$\text{With} \quad \vec{J_s} = (0, J_s, 0), \Longrightarrow J_s = \frac{c}{4\pi} \frac{dH}{dx}$$

$$J_s(x) = \frac{c}{4\pi\lambda_L} H_0 \exp^{\left(-\frac{x}{\lambda_L}\right)}$$

$$\lambda_L \sim \sqrt{\frac{1}{n_s}}, \text{ so it decreases with temperature}$$

$$\lambda_L(T) = \lambda_L(0) \left[1 - (\frac{T}{T_c})^4\right]^{-1/2}$$

Ginzburg–Landau theory:

Based on the Landau theory on second order phase transition Vitaly Lazarevich Ginzburg and Lev Landau proposed [7] that the free energy of the superconductor near superconducting transition can be described by a complex order parameter ψ

Ψ is associated with superconducting electron density n_s

$$n_s = |\psi|^2$$

Now expanding Ψ in term of free energy F_s

$$F_s = F_n + \alpha|\psi|^2 + \frac{\beta}{2}|\psi|^4 + \frac{1}{2m}|(-i\hbar\nabla - 2eA)\psi|^2 + \frac{|B|^2}{2\mu_0}|$$

Where α and β considered as superconducting parameter. F_n is normal state free energy, m is effective mass and e is the charge of electron and A is magnetic vector potential B is magnetic field.

By minimizing the free energy with respect to fluctuations in the order parameter and the vector potential, one arrives at the Ginzburg–Landau equation

$$\alpha\psi + \frac{\beta}{2}|\psi|^2\psi + \frac{1}{2m}(-i\hbar\nabla - 2eA)^2\psi = 0$$

$$J = \frac{2e}{m}Re\{\psi^*(-i\hbar\nabla - 2eA)\psi\}$$

For a homogeneous superconductor where there is no superconducting current

$$\alpha\psi + \frac{\beta}{2}|\psi|^2\psi = 0$$

$$|\psi|^2 = -\frac{\alpha}{\beta}$$

ψ is a complex order parameter, hence its magnitude should be ≥ 0 when $T > T_c$

$$|\psi|^2 = 0$$

but when $T < T_c$ magnitude of the order parameter is positive

$$|\psi|^2 = -\frac{\alpha_0(T - T_c)}{\beta}$$

As T approaches T_c, ψ vanishes, which is typical behavior of second order transition

Ginzburg–Landau theory introduced new characteristic lengths in superconductors they are

1. **Coherence length (ξ)** defined as the length scale on which the superconducting order parameter changes considerably

$$\xi = \sqrt{\frac{\hbar^2}{2m|\alpha|}}$$

2. **Penetration depth (λ_L)** which was previously introduced by London brothers. Penetration depth in terms of order parameter

$$\lambda = \sqrt{\frac{m}{4\mu_o e^2 \psi_0^2}}$$

3. **Ginzburg-Landau parameter(κ)** is the ratio of penetration depth(λ_L) and coherence length(ξ)

$$\kappa = \frac{\lambda}{\xi}$$

for Type-I superconductors $0 < \kappa < 1/\sqrt{2}$ and for Type-II superconductors $\kappa > 1/\sqrt{2}$

BCS theory:

John Bardeen, Leon Cooper and Robert Schrieffer, in 1957, proposed the basis of a quantum theory of Superconductivity [6] which is now popularly known as "BSC Theory". Specific accomplishments of BSC theory are:

1. An attractive interaction between electrons can lead to a ground state separated from the excited states by an energy gap. The critical field, the thermal properties and most of the electromagnetic properties are consequences of the energy gap.

2. The electron-lattice-electron interaction leads to an energy gap of the observed magnitude. The indirect interaction proceeds when one electron interacts with the lattice and deforms it; a second electron sees the deformed lattice and adjusts itself to take advantage of the deformation to lower its energy. Thus the second electron interacts with the first electron via the lattice deformation.

3. The penetration depth and the coherence length emerge as consequences of the BCS theory. The London equation is obtained for magnetic fields that vary slowly in space.

4. The criterion for the transition temperature of an element or alloy involves the electron density of orbitals $D(\epsilon_F)$ of one spin at the Fermi level and the electron-lattice interaction parameter U, which can be estimated from temperature dependence of electrical resistivity. For $[UD(\epsilon_F)] \ll 1$, the BCS theory predicts T_c as:

$$T_c = 1.14\,\theta\exp\left[-\frac{1}{U\,D(\epsilon_F)}\right]$$

where θ is the Debye temperature. This result for T_c is in agreement at least qualitatively with the experimental data.

Magnetic flux through a superconducting ring is quantized and the effective unit of charge is 2e rather than e. The BCS ground state involves pairs of electrons; thus flux quantization in terms of the pair charge 2e is a consequence of the theory.

4. Vortex matter

In Type-I superconductors, no magnetic flux can enter the material as long as it is in the superconducting state. Once the applied field is more than the critical field H_c, the magnetic flux enters the material since it becomes normal.

In Type-II superconductors, the coherence length is smaller than the London penetration depth [9,10]. The partial diamagnetic state occurring between the lower critical field (H_{c1}) and the upper critical field (H_{c2}) in the M-H phase diagram is called the mixed state and is shown in Fig. 6 (b).

In the mixed state, the magnetic flux lines enter the material in narrow regions which become non-superconducting and are comparable to the size of coherence length [9, 10]. The entry of flux lines occurs in the form of vortices / fluxoids. The entry of a fluxoid locally loses the condensation energy. The loss of

energy due to the penetration of fluxoid is called the penalty energy and is $\frac{H_c^2}{2\mu_o}$ per unit volume.

The vortices are surrounded by rings of super-currents which shield the rest of the superconductor from getting exposed to the applied magnetic fields. The vortices arrange themselves in a regular structure known as the vortex lattice as described by Abrikosov [11]. This is a quantized effect with the flux quantum associated with each of the vortices being $\Phi_0 = h/2e$, where h is the Planck's constant and 2e is the total charge of the Cooper pair. A schematic representation of the fluxoids in the sample volume is shown in Fig. 10.
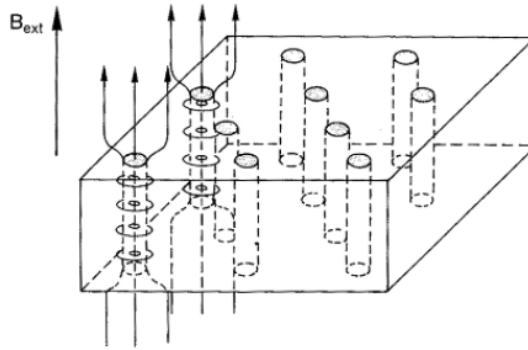
Fig. 10. A Schematic representation of the mixed state of a Type-II superconductor. The flux tubes (fluxoids) arranged in a two-dimensional lattice, allow the magnetic field to penetrate. Each fluxoid is surrounded by superconducting ring currents and enclose one magnetic flux quantum.

The magnetic field, when applied parallel to c-axis of the samples generates supercurrents in the a-b planes of the sample. Since the applied magnetic field and the generated supercurrents are perpendicular to each other, Lorentz force gets generated which tends to move the vortices causing energy dissipation. This is schematically shown in Fig. 11.
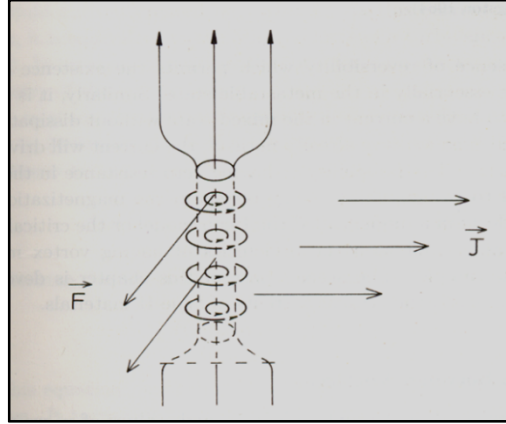
Fig. 11. A schematic sketch showing the direction of the Lorentz force resulting on the vortices due to the application of magnetic field.

In order to minimize the motion of vortices, pinning centers need be introduced which pin the magnetic flux lines. This is achieved through vortex pinning or flux pinning, by creating normal sites out of which the vortex cannot leave without large energy increase [12]. The vortex will be pinned to such inclusions as it does not have to spend energy to destroy superconductivity in that inclusion. An inclusion is most efficient when its diameter matches with the coherence length ξ of the material [13].

The bulk pinning force dented as F_p is the sum over all contributions from various pinning centers, and if the number of interactions per unit volume is N, then F_p becomes equal to Nf_p, where f_p is the elementary pinning force [14]. Critical current density is related to the flux pinning force F_p as

$$F_p = Nf_p = J_c \times B \ldots\ldots\ldots (A.11)$$

5. Relation of J_c to the magnetization in orthorhombic samples

The critical current density 'J_c' in type-II superconductors can be estimated by analyzing the magnetization using critical state model proposed by Bean [8] which was discussed in section 2.7 of Chapter II.

The formulation for the samples in orthorhombic geometry is discussed below:
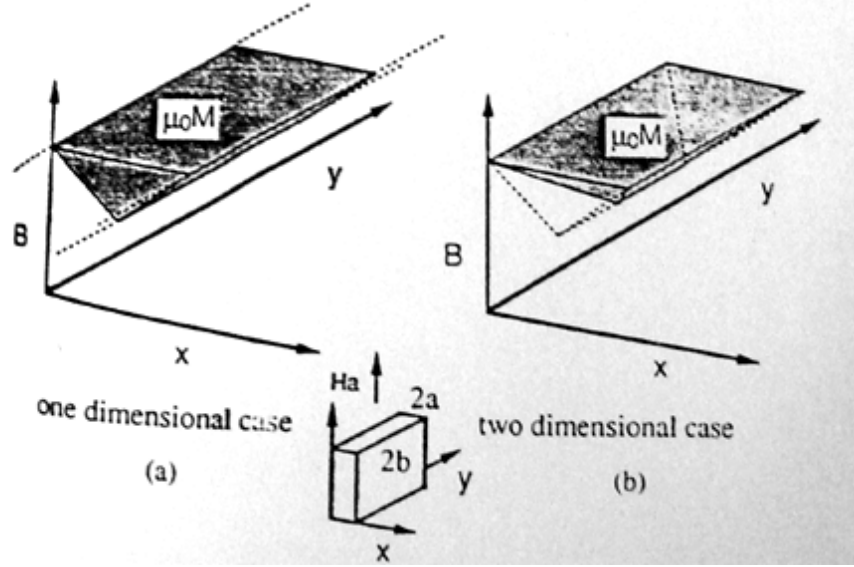
Fig. 9. Schematic illustration of the field penetration for **(a)** one dimensional case and **(b)** orthorhombic geometry.

Fig. 9 shows a schematic illustration of the field penetration for one-dimensional orthorhombic case. When J_c along each side of the cross-section of the sample is same as the initial M (H) curve is given by

$$M(H) = -H + \frac{H^2}{2J_c}\left(\frac{1}{a} + \frac{1}{b}\right) - H^3(3J_c ab), \text{ for } 0 < H < H^*$$

$$M(H) = -J_c\left(\frac{1}{2} - \frac{a}{6b}\right), \text{ for } H^* < H$$

and the reverse curve is given by

$$M(H) = -J_c a\left(\frac{1}{2} - \frac{a}{6b}\right) + H_m - H - \left[\frac{(H_m - H)^2}{4J_c}\right]\left(\frac{1}{a} + \frac{1}{b}\right) + \frac{(H_m - H)^2}{12J_c 2ab}$$

$$, \text{ for } H_m - 2H^* < H < H_m$$

$$M(H) = J_c a\left(\frac{1}{2} - \frac{a}{6b}\right), \text{ for } -H_m < H < H_m - 2H^*$$

Where *a* and *b* are dimensions of the cross section of a sample with $a \geq b$

Therefore for the orthorhombic geometry, when H_m is larger than *2H*,

$$M(H)^+ - M(H)^- = J_c b \left(1 - \frac{b}{3a}\right) \dots\dots (2.24)$$

6. Applications of Superconductors

Considerable amount of efforts have been invested in developing applications for HTSCs in the fields of power generation, power transmission, power storage, particle accelerators, MRI etc. [15-18]. These applications make use of the ability of the materials to carry high currents without loss of power, to sustain large currents without change in their magnitudes over long periods of time, to levitate large weights, to exhibit tunneling effects etc. Table 1 lists some of the applications being explored, based on the properties exhibited by the superconductor.

Superconductors can carry electric currents several orders of magnitude more than the ordinarily used conductors such as copper, without dissipation [19-21]. Magnets with the potential of generating very high fields with high homogeneity and stability of the field and better reliability compared to resistive / permanent magnets are possible. First operational superconductor magnet (developed in 1957) was made with Nb wire, which could produce 0.7 T [22]. In 1962, a superconductor magnet was fabricated using Nb-Sn, which could produce 7.0 T field. At present, superconductor magnets are able to produce 17T of magnetic field [15]. Their use in magnetic resonance imaging ensures a superior image quality. In high energy physics, particles can be accelerated, deflected and focused by the fields generated by superconducting magnets [23].

Table 1. Applications of superconductivity

Basis for Property	Applications
$R = 0$ and high J_c	1. Magnets for variety of applications 2. Passive microwave devices 3. Interconnects in microelectronics 4. Electrical energy transport by cables
Josephson tunneling	1. Microwave detectors and mixers 2. In physical measurements (SQUIDs etc) 3. Computers (fast logic and memory circuits) 4. Plasma and space 5. In medicine (magnetic encephalography)
High J_c at high H_{c2}	1. Electrical power industry 2. Plasma confinement (in high energy physics) 3. In transport (levitation trains, MHD-propelled ships) 4. Medicine (nuclear magnetic resonance tomography)

The Superconducting fault current limiter [17] (SC-FCL) is a unique device, without any conventional equivalent, which limits the current as soon as it oversteps a predetermined threshold value. It prevents the current from exceeding a given value. While it presents negligible impedance in no fault regime (no voltage drop), it naturally and automatically inserts high impedance when the current exceeds a certain value.

Superconducting flywheel energy storage [24] (S-FES) system is an energy storage device with low kinetic energy losses, which utilizes the diamagnetic levitation property of superconductor. The system, therefore, is one of the most promising candidates for application in the renewable energy field, in photovoltaic or wind energy development where power generation is intermittent. The use of HTSCs for generation, storage, transmission and transformation of electrical power in electrical industry has been assessed by major industries all over the world. Fig. 12 [25] shows

the projected need for superconductors at various sectors in the coming decade.
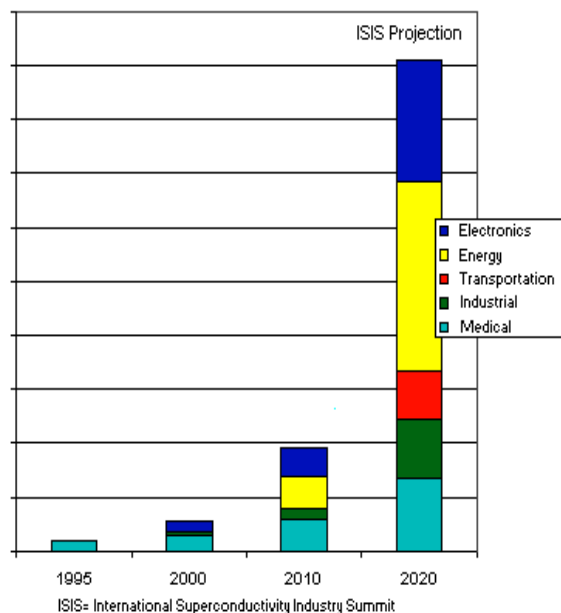
Fig. 12. The need of superconductors in various areas is increasing and will grow multifold in the coming decade as predicted by ISIS (International Superconductivity Industry Summit) [25**]**

The SQUIDs, using conventional superconductors and operating at liquid helium temperature, i.e. 4.2K, are the most sensitive magnetometers [18]. SQUIDs, made from oxide superconductors and operating at liquid nitrogen temperature (77K), are of interest when it comes to extending their use to other applications like portable high field magnets for medical and military applications. In VLSI (very large scale integration) technology, the use of HTSC interconnections working at 77K offer several advantages and it is expected that in high-speed computers and telecommunications, this will be used extensively in near-future.

The possibilities of applications of HTSCs in magnetically levitated trains [16] and in magnetic mineral separation is also being pursued [26], though making cost-effective devices for uses in these fields appear to be

somewhat remote. The three properties of superconductors relevant to applications, viz. the critical temperature T_c, critical current density J_c and critical magnetic field H_c are continually sought to be improved. The current density and magnetic field requirements for different applications are listed in Table. 2.

Table 2. J_c and H_c requirements for various applications in electrical power industry

Application	J_c (A /cm^2)	$\mu_o H_c$ (T)
Power transmission	2×10^4	1
Power generation	2×10^4	5–7
Transformers	10^4	1
Power storage	10^3–10^4	5–10
MRI Scanners	10^4	2
Mineral separation	10^4	2-5

Application of superconductors as trapped field magnets, magnetic shields and porous superconductors as fault current limiters have been discussed in Chapter I.

Reference

1. J. File and R. G. Mills, Phys. Rev. Lett. 10, 93 (1963).

2. W. Meissner, Z. Ges. K¨alteindustrie 34, 197 (1927).

3. W. Meissner and R. Ochsenfeld, Naturwiss. 21, 787 (1933).

4. J. G. Bednorz and K. A. M¨uller, Z. Phys. B64, 189 (1986).

5. Josephson, B. D., "Possible new effects in superconductive tunnelling," Physics Letters 1, 251 (1962) doi:10.1016/0031-9163(62)91369-0

6. Bardeen J, Cooper L N and Schrieffer J R 1957 *Phys. Rev.* **106** 162

7. V.L. Ginzburg and L.D. Landau, Zh. Eksp. Teor. Fiz. 20, 1064 (1950). English translation in: L. D. Landau, Collected papers (Oxford: Pergamon Press, 1965) p. 546

8. C. P. Bean, *Phys. Rev. Lett.* **8** (1962) 250

9. Krabbes G, Fuchs G and Canders W-F 2005 *High Temperature Superconductor Bulk Materials: Fundamentals - Processing - Properties Control - Application Aspects* (Wiley, GmbH, KGaA, Weinheim)

10. Pippard A B 1953 *Physica C* **19** 765

11. Abrikosov A A 1957 *Zh. Eksp. Teor. Fiz.* **32** 1442

12. Campbell A M and Evetts J E 1972 *Adv. Phys.* **21** 199

13. Murakami M 1992 *Melt Processed High temperature Superconductors* (World Scientific, Singapore)

14. Matsushita T 2007 *Flux Pinning in Superconductors* (Springer-Verlag Berlin Heidelberg)

15. Masaru Tomita and Masato Murakami, *Nature* **421** (2003) 517-519

16. M. Tomita, K. Nagashima, T. Herai and M. Murakami, *Physica C* **372–376** (2002) 1216–1220

17. J. Sim, K. B. Park, H. R. Kim, J. S. Kang, B. W. Lee, H. M. Kim, I. S. Oh, O. B. Hyun, *Cryogenics* **47** (2007) 183–188

18. T. Bauch, J. Johansson, K. Cedergren, T. Lindstrom and F. Lombardi, *Physica C* **463–465** (2007) 979–984

19. H. I. Dua, D. H. Lee, B. S. Han, S. S. Song, J. S. Lee, S. W. Yim and T. H. Sung, *Physica C* **471** (2011) 1559–1564

20. Jian X. Jin, *Physica C* **460–462** (2007) 1443–1444

21. O. Tsukamoto, *Supercond. Supercond. Sci. Technol.* **17** (2004) S185–S190

22. J. E. Kunzler, E. Buehler, L. Hsu, and J. Wernick, *Phys. Rev. Lett.* **6** (1961) 89-91

23. P. Schmiiser, *Rep. Prog. Phys.* **54** (1991) 683-730

24. Kazuyuki Demachi, Issei Masaie, Takumi Ichihara and Makoto Kita, *Physica C* **426–431** (2005) 826–833

25. http://www.superconductors.org/Uses.htm

26. J. H. P. Watson, *Minerals Engineering* **7** (1994) 737–746

Publications:

List of Patents:

Patents with filing authorities at DRDO IPR:

1. Improved method of fabrication of porous refractory matrices
2. Method of coating emission enhancement films on dispenser cathodes by chemical route
3. Method of fabricating superconductor products

Patents under preparation:

1. Introduction of nanoparticles into non-interaction preforms
2. Fabrication nano-porous Nickel fibers

Publications in Journals and Conferences

1. "Complex-shaped Alumina Products through Rapid Prototyping" T. Rajasekharan, **P. M. Swaroop Raju**, Rakesh Kumar Pandey, V. Seshu Bai, R. Pradyumna and M. A. H. Baig, Metals Materials and Processes, 2007, Vol. 19, No. 1-2, pp. 41-46

2. "Effect of Infiltration temperature on the properties of Infiltration Growth Processed YBCO superconductor" S. Pavan Kumar Naik1, **P. Missak Swarup Raju**, N. Devendra Kumar, T. Rajasekharan and V. Seshubai submitted to *Physica C* (under revision PHYSC-D-12-00241R1)

3. "A novel method of shaping YBCO superconducting bulk products through gelcasting" **P. Missak Swarup Raju**, T. Rajasekharan and V. Seshubai (under preparation)

4. "Innovative method of introducing ceria nano particles as pinning centers in YBCO matrix" **P. Missak Swarup Raju**, T. Rajasekharan and V. Seshubai (under preparation)

5. "Flux profile studies on ceria doped IG processed YBCO nanocomposites" **P. Missak Swarup Raju**, T. Rajasekharan and V. Seshubai (under preparation)

6. "Mechanism of refinement in Y-211 particles in ceria doped IG processed YBCO composites" **P. Missak Swarup Raju**, T. Rajasekharan and V. Seshubai (under preparation)

7. "On introduction of nano-ceria into Y-211 preforms for flux pinning in YBCO superconductors" **P. Missak Swarup Raju1**, N. Devendra Kumar, S. Pavan Kumar Naik1, T. Rajasekharan2 and V. Seshubai1, ICMST 2012, 10-14 June 2012, Kottayam, Kerala

8. "Fabrication of GdBa$_2$Cu$_3$O$_{7-\delta}$ (GdBCO) superconductor in air through Preform Optimized Infiltration Growth Process (POIGP)" S. Pavan Kumar Naik1, **P. Missak Swarup Raju**, N. Devendra Kumar, V. Seshubai and T. Rajasekharan, ICMST 2012, 10-14 June 2012, Kottayam, Kerala.

9. "Complex shapes of Alumina through gelcasting" **P. Missak Swarup Raju**, V. Seshu Bai, T. Rajasekharan PM 2006, National conference on "Powder

metallurgy and its Best" 32nd Annual Technical meeting, Jan 23-24, 2006, Hyderabad

10. "A Study of Iron Nanoparticles in Sub-Critically Dried Silica Aerogel", **P. Missak Swarup Raju**, T. Rajasekharan, A. Satish Kumar, V .Seshu Bai, IUMRS-ICAM 2007, 10th national conference on Advance materials, October 8-13, 2007, IISc., Bangalore.

11. "Thermo-elastic properties of tungsten-copper composite processed through Pressure- less consolidation Technique", **P. Missak Swarup Raju**, V. Seshu Bai, Ashutosh Panchal, M.T. John, T. Rajasekharan, Bijoy Sharma, PM-09 international conference and trade exhibition, Feb 16-18, 2009, Panjim, Goa

12. "Pressure- less consolidation of porous Tungsten metal powder", **P. Missak Swarup Raju**, V. Seshu Bai, T. Rajasekharan, Ashutosh Panchal, Bijoy Sarma, PM-09 international conference and trade exhibition, Feb 16-18, 2009, Panjim, Goa

13. Processing of Porous Structures of Nickel through Gelcasting", **P. Missak Swarup Raju**, T. Rajasekharan, Ashutosh Panchal, N. Arvind kumar, Bijoy Sharma, PM-09 international conference and trade exhibition, Feb 16-18, 2009, Panjim, Goa

14. "Fish Tail effect in high Jc bulk YBCO superconductor fabricated by Seeded Infiltration Growth process", N. Devendra Kumar1, **P. Missak Swarup Raju**, Sabyasachi Saha,V. Seshu Bai1, Alok Banerjee, M. Muralidharan and T. Rajasekharan, 54th DAE Solid State Physics Symposium 2009

15. Effect of nano sized CeO_2 doping on magnetic and microstructural properties of IG processed YBCO. **P Missak Swarup Raju**, N. Devendra Kumar, V. Seshubai and T. Rajasekharan. Proceedings of India-Singapore Joint Physics Symposium 2010 (ISJPS-2010), Page 72, February 19-21, 2010 University of Hyderabad, Hyderabad.

16. High J_c bulk YBCO superconductors fabricated by Preform Optimized Infiltration Growth Process (PO-IGP)V. Seshubai and N. Devendra Kumar India-Singapore Joint Physics Symposium 2010 (ISJPS-2010), proceedings page 38, February 19-21, 2010 University of Hyderabad, Hyderabad.

17. "Nano-twinning: cause for high Jc to high fields in bulk YBCO superconductor fabricated by Preform Optimized Infiltration Growth Process" N. Devendra Kumar, **P. Missak Swarup Raju**, Sabyasachi Saha, V. Seshu Bai, K. Muraleedharan and T. Rajasekharan, International conference Electron Nanoscopy & XXXII Annual Meeting of EMSI (EM-50) organized jointly by Defence Metallurgical Research Laboratory and Electron Microscope Society of India during July 6-8, 2011

P Missak Swarup Raju

Phone: +91-986-670-2909
E-mail: swarupraj@gmail.com/swarup_pmr@yahoo.com

Work Address:
Research Scholar
School of Physics
University of Hyderabad
Hyderabad – 500046
Andhra Pradesh, India
Phone: 91-40-23134365, 23010241

Home Address:
P. M. Swarup Raju
S/o P .S. Raju
Balimela college of Science and
Technology, Balimela
Malkangiri, ORISSA
Phone: 09866702909

Academics

- Pursuing Doctor of Philosophy (**Ph.D**.) at University of Hyderabad, in Physics Stream
  * Specialization : Superconductivity
  * Thesis to be submitted shortly
  * Tentative Title of the thesis: "**Infiltration growth processing of YBCO nano-composites: shape forming, microstructural and magnetic studies"**

- Master of Science (**M.Sc**.) from University of Hyderabad in Physics Stream, 2003 with **68.88 %**
  * Specialization : Quantum optics
  * Undergone research training in the form of a project as a part of M.Sc. program
  * Title of the project: "**Guided mode mediation in EIT wave guide"**

- Bachelor of Science (**B.Sc**.) from Behrampur university, 2001 with **65.37 %**
  * Specialization: **Physics Honors**

Additional Qualifications:

- Secured **83** percentile in Graduate Aptitude Test in Engineering (GATE), 2003 National Level Examination.

- Worked as JRF for 2 years and as SRF for 2 years in a research project funded by Defence Research Development Organization (DRDO).

Skills

- Having hands on experience with various material processing techniques (both solid state and chemical routes) such as
  - **Gelcasting**
  - **Injection molding**
  - **electrochemical deposition**
  - **Powder Metallurgy processing**
  - **Chemical vapor deposition**
  - **Thermal vapor deposition**
- Preparation of nano particles through chemical route
- Preparation of carbon nano-tubes through Chemical Vapor Deposition (CVD) route.
- Versed with various characterize techniques in order to measure various properties like:
  - s**urface area**, **particle size**, **viscosity**, **zeta potential**, **d_{33}, dielectric properties,**
  - **four probe resistivity,**
  - **ac susceptibility, magnetization, magnetic levitation etc.**
  - **Mechanical properties compression strength, indentation, density measurement, CTE measurement, Thermal conductivity.**
  - **Crystal structure determination using X-ray diffraction studies**
  - **Microstructural analysis (on micrographs obtained both from optical and electron microscopes)**

Achievements

Three patents have been submitted for getting filed which emerged out of the work that was carried out by me during my Ph.D./project tenure. All the three have been reviewed internally and have been recommended for patenting. The filing process is underway.

Following are the titles of the patents filled in collaboration with Defence Metallurgical Research Laboratory (DMRL), Hyderabad and Microwave Tube Research and Development Centre (MTRDC), Bangalore

- *METHOD OF FABRICATING SUPERCONDUCTOR PRODUCTS*

- *IMPROVED METHOD OF FABRICATION OF POROUS REFRACTORY MATRICES*

- *METHOD OF COATING EMISSION ENHANCEMENT FILMS ON DISPENSER CATHODES BY CHEMICAL ROUTE*

Interests

- Applied superconductivity
- Functional Ceramics and Composite Materials
- Coated Conductors, Superconducting Wires and Tapes
- Energy application materials

Hands on experience with

* Physical Property Measurement System 'PPMS' (Quantum Design-make) with various attachments like Vibrating Sample Magnetometer (with Oven), ac susceptibility measurement, Resistivity, thermal transport measurement etc.

* Microscopes like
  * Metallurgical Optical Microscope with Polarizer attachment (Zeiss make, Axiovert)
  * Scanning Electron Microscope (FEI-make, XL30 ESEM)
  * Field Emission Scanning Electron Microscope FE-SEM (Zeiss make, Ultra 55)
  * Atomic Force Microscope

* Low Speed Diamond Saw, ISOMET 1000 and an Auto-polisher of Buehler make. Developed expertise in preparing samples for observation under SEM / TEM.

* Furnaces operating to $1200^{\circ}C/1700^{\circ}C$ furnaces controlled by programmable temperature controller and thyristor (Eurotherm-make/WEST-make)

* Heat treatment of samples in Hydrogen / Methane atmospheres.

* Versed with sample preparation techniques for fabricating high temperature bulk (RE)BCO superconductors.

* Shaping machines like lathe, miller, hydraulic press, dicer etc.

Materials worked with

These are some of the material that I have worked with so far

- **Alumina**
- **PZT**
- **YBCO**
- **Fused Silica**
- **Si_3N_4**

- **Silicon Carbide**
- **Tungsten**
- **Carbonyl Iron**
- **Nickel**
- **Bronze**

Computational skills

∗ Origin, MS office (Word, excel, power-point etc.) and FORTRAN.

∗ Microstructural analysis using Axio-vision / Image analysis software.

∗ Having familiarity with scientific software like JCPDS data cards, binary phase diagrams.

Work Experience in the projects

∗ Research Fellow in the project entitled "Gelcasting and Rapid prototyping of Ceramics" funded by Defense Research and Development Organization (DRDO), Ministry of Defence, Govt. of India

Publications:

1. A novel method of shaping YBCO superconducting bulk products through gelcasting
   P.Missak Swarup Raju, N. Devendra Kumar, T. Rajasekharan and V. Seshubai
   Submitted to *Supercond. Sci. Technol.* – Under Review

2. Effect of nano-CeO_2 on the microstructural and magnetic properties of IG processed YBCO superconductors fabricated by Gelcasting technique
   P. Missak Swarup Raju, N. Devendra Kumar, T. Rajasekharan and V. Seshubai
   Submitted to *Supercond. Sci. Technol.* – Under Review

3. Slurry based technique to process complex-shaped Alumina Products through Rapid Prototyping
   P. Missak Swarup Raju, T. Rajasekharan,
   PM 2006, National conference on "Powder metallurgy and its Best" and 32nd Annual Technical meeting, Jan 23-24, 2006, Hyderabad

4. A Study of Iron Nanoparticles in Sub-Critically Dried Silica Aerogel
   P. Missak Swarup Raju, T. Rajasekharan, A. Satish Kumar, V .Seshu Bai,
   IUMRS-ICAM 2007, 10th national conference on Advance materials, October 8-13, 2007, IISc., Bangalore.

5. Complex-shaped Alumina Products through Rapid Prototyping
   T. Rajasekharan1, **P. M. Swaroop Raju**, Rakesh Kumar Pandey, V. Seshu Bai, R. Pradyumna and M. A. H. Baig,
   Metals Materials and Processes, 2007, Vol. 19, No. 1-2, pp. 41-46

6. Thermo-elastic properties of tungsten-copper composite processed through Pressure-less consolidation Technique
P. Missak Swarup Raju, V. Seshu Bai, Ashutosh Panchal, M.T. John, T. Rajasekharan, Bijoy Sharma,
PM-09 international conference and trade exhibition, Feb 16-18, 2009, Panjim, Goa

7. Pressure- less consolidation of porous Tungsten metal powder
P. Missak Swarup Raju, V. Seshu Bai, T. Rajasekharan, Ashutosh Panchal and Bijoy Sarma,
PM-09 international conference and trade exhibition, Feb 16-18, 2009, Panjim, Goa

8. Processing of Porous Structures of Nickel through Gelcasting
P. Missak Swarup Raju, T. Rajasekharan, Ashutosh Panchal, N. Arvind kumar and Bijoy Sharma,
PM-09 international conference and trade exhibition, Feb 16-18, 2009, Panjim, Goa

9. Fish Tail effect in high Jc bulk YBCO superconductor fabricated by Seeded Infiltration Growth process
N. Devendra Kumar, **P. Missak Swarup Raju**, Sabyasachi Saha,V. Seshu Bai, A. Banerjee, K. Muraleedharan and T. Rajasekharan
54th DAE Solid State Physics Symposium 2009

10. High J_c bulk YBCO superconductors fabricated by Preform Optimized Infiltration Growth Process (PO-IGP)
V. Seshubai, **P. Missak Swarup Raju** and N. Devendra Kumar
India-Singapore Joint Physics Symposium 2010 (ISJPS-2010), proceedings page 38, February 19-21, 2010 University of Hyderabad, Hyderabad.

11. Effect of nano sized CeO_2 doping on magnetic and microstructural properties of IG processed YBCO
P Missak Swarup Raju, N. Devendra Kumar, V. Seshubai and T. Rajasekharan
Proceedings of India-Singapore Joint Physics Symposium 2010 (ISJPS-2010), Page 72, February 19-21, 2010 University of Hyderabad, Hyderabad.

12. Nano-twinning: cause for high Jc to high fields in bulk YBCO superconductor fabricated by Preform Optimized Infiltration Growth Process
N. Devendra Kumar, **P. Missak Swarup Raju**, Sabyasachi Saha, V. Seshu Bai, K. Muraleedharan and T. Rajasekharan
International conference Electron Nanoscopy & XXXII Annual Meeting of EMSI (EM-50) organized jointly by Defence Metallurgical Research Laboratory and Electron Microscope Society of India during July 6-8, 2011

Personal

- ❖ Father's Name   :   P. S. Raju
- ❖ Mother's Name   :   P. Sarojini
- ❖ Date of Birth   :   June 6, 1981
- ❖ Nationality   :   Indian
- ❖ Gender   :   Male

Reference

- ❖ Professor. V. Seshubai, University of Hyderabad, Hyderabad, India.
  E-mail: seshubai@gmail.com

- ❖ Dr. T. Rajasekharan, Scientist-G, DMRL, Hyderabad, India.
  E-mail: trajasekharan@gmail.com

- ❖ Dr. A. R. James, Defence Metallurgical Research Laboratory, Hyderabad, India
  E-mail: james@dmrl.drdo.in

- ❖ Dr.K. C. James Raju, University of Hyderabad, Hyderabad, India.
  E-mail: kcjr@uohyd.ernet.in

- ❖ Dr. S. Srinath, University of Hyderabad, Hyderabad, India.
  E-mail: sssp@uohyd.ernet.in

Declaration

I declare that the information provided is true to the best of my knowledge.

P Missak Swarup Raju